

**CONTROLLING OPTO-ELECTRIC PROPERTIES OF CADMIUM
STANNATE THIN FILMS DEPOSITED BY RF SPUTTERING**

by

Evan L. Kimberly

A thesis submitted to the Faculty of the University of Delaware in partial fulfillment of
the requirements for the degree of Master of Science in Physics

Summer 2011

Copyright 2011 Evan L. Kimberly
All Rights Reserved

**CONTROLLING OPTO-ELECTRIC PROPERTIES OF CADMIUM
STANNATE THIN FILMS DEPOSITED BY RF SPUTTERING**

by

Evan L. Kimberly

Approved:

Robert W. Birkmire, Ph.D.
Professor in charge of thesis on behalf of the Advisory Committee

Approved:

George Hadjipanayis, Ph.D.
Chair of the Department of Physics and Astronomy

Approved:

George H. Watson, Ph.D.
Dean of the College of Arts and Sciences

Approved:

Charles G. Riordan, Ph.D.
Vice Provost for Graduate and Professional Education

ACKNOWLEDGMENTS

First, I would like to thank Brian McCandless for all of his help and patience with me during the course of this work, especially regarding his help with the variable angle spectroscopic ellipsometer. Further, I would like to thank Tiejun Meng for all his collaboration and help with measurements, Robert Birkmire for his support and guidance and Vicky DiNetta for teaching me to use the atomic force microscope. I owe every person at the IEC a special thanks as well, for making me feel welcome and always being willing to help out or discuss something. I would also like to thank Corning for the funding provided for this work.

A special thanks is deserved for all of my friends in physics, here at the University of Delaware as well as around the country, for making my time in physics a wonderful experience thus far.

A very special thanks to Anna, for all of her patience, love and support throughout my time at the University of Delaware, as well as her very gratefully accepted help editing this thesis.

This work is dedicated to my parents, who always encouraged me to be curious.

TABLE OF CONTENTS

LIST OF FIGURES	viii
LIST OF TABLES	xii
LIST OF ABBREVIATIONS	xiii
ABSTRACT	xv

Chapter

1 INTRODUCTION	1
1.1 State of the World.....	1
1.2 Options.....	3
1.3 Thesis Statement.....	4
2 BACKGROUND	6
2.1 Cadmium Telluride Solar Cells.....	6
2.2 Cadmium Tin Oxide.....	8
2.3 New Cadmium Telluride Device Structure.....	9
3 ELLIPSOMETRY	11
3.1 Overview.....	11
3.2 Obtaining Data.....	15
3.2.1 Equipment.....	15
3.2.2 The Brewster Angle.....	16
3.2.3 Calibration Procedure.....	17
3.2.4 Brewster Angle Determination.....	18
3.2.5 Ψ and Δ Obtained.....	20
3.3 Building a Model.....	20
3.3.1 Minimization.....	20
3.3.2 The Layers.....	26

3.3.2.1	Substrate.....	27
3.3.2.2	Material Layer.....	28
3.3.2.3	Surface Layer.....	29
3.3.3	Oscillator Models.....	30
3.4	Fitting the Model to the Data.....	36
3.4.1	Initial Model.....	38
3.4.2	Final Model.....	44
3.4.3	Gradings.....	50
4	EXPERIMENTAL.....	56
4.1	Deposition.....	56
4.2	Heat Treatment.....	59
4.3	Characterization and Analysis.....	62
4.3.1	Ellipsometry.....	62
4.3.2	Spectrophotometer.....	66
4.3.3	Glancing Incident Angle X-Ray Diffraction.....	67
4.3.4	Energy-Dispersive X-Ray Spectroscopy.....	69
4.3.5	Atomic Force Microscopy.....	70
4.3.6	Hall Effect and Van der Pauw.....	71
5	RESULTS.....	75
5.1	Deposition Conditions.....	77
5.1.1	Temperature.....	77
5.1.2	Atmospheric Oxygen Content.....	80
5.1.3	Sputtering Ambient Pressure.....	86
5.1.4	Summary.....	93
5.2	Heat Treatment Conditions.....	94
5.2.1	Effect of Atmospheric Oxygen Content After Heat Treatment..	94
5.2.2	Thickness Dependence.....	102
5.2.3	Heat Treatment Environment.....	106
5.2.4	Summary.....	113
6	CONCLUSION AND FUTURE WORK.....	114
6.1	Conclusion.....	114

6.1.1	Summary of Results.....	114
6.1.2	Ellipsometry.....	115
6.1.3	Further Details.....	116
6.2	Future Work.....	117
6.2.1	Cadmium Tin Oxide.....	117
6.2.2	Cadmium Telluride Solar Cells.....	117
	REFERENCES.....	119

LIST OF FIGURES

2.1	A diagram showing a cross- section of a traditional CdTe solar cell. Layers are not drawn to scale.....	7
2.2	A diagram showing a cross- section of the CdTe solar cell as proposed by Wu. Note the $Zn_xCd_{1-x}S/CdS$ layer. This is a by-product of interdiffusion between the ZTO and CdS layer and is actually beneficial in the working of this device structure [11]. Layers are not drawn to scale.....	10
3.1	The Institute of Energy Conversion's variable angle spectroscopic ellipsometer. A calibration sample is currently affixed to the sample stage. Not pictured is the device's input polarizer, to the right of the AutoRetarder. The Institute's UV/VIS spectrophotometer is visible in the background.....	15
3.2	An example of Brewster angle determination for sample SP3147.7. Here, due to the near identical minimum values of the Ψ curves, the Brewster angle can be assumed to be evenly spaced between the two minima, at approximately 62°	19
3.3	The general oscillator layer window from the WVASE32 software after fitting a TL oscillator to sample SP3128.7. The blue curve is the actual oscillator being fit to ϵ_2 . The black curve is the Kramers-Kronig calculated fit for ϵ_1 . The red and green curves are ϵ_2 and ϵ_1 for the reference oscillator, respectively.....	39
3.4	Graph of MSE (mse0) vs. CTO thickness (Thick.2) for sample SP3118.7ht. This MSE is unique at 750 nm.....	44
3.5	An example of simple index grading for sample SP3118.7ht using data at 500 nm wavelength. This grading has a variation range of 3.2%. It also has a symmetric exponent of 1.6. The extinction coefficient is not present. Due to the nature of the grading, the grading for each constant is identical over their respective ranges.....	51

3.6	An example of a grading for SP3151.2a using data at 500 nm wavelength. Here, the left axis is associated with n and the right axis is associated with k . Note the node at approximately 770 nm.	52
4.1	A diagram of the SP3 sputtering system. Image provided by Tiejun Meng.	57
4.2	A comparison of direct (right line) and indirect (left line) band gap calculation for SP3151.7. The band gap of about 2 eV for the indirect is similar to known data regarding amorphous CTO [28] [33].	65
4.3	A comparison of transmission calculated via extinction coefficients obtained from VASE (brown) with normalized transmission obtained with spectrophotometry (green) for sample SP3118.7 with no heat treatment.....	67
4.4	GIXRD spectra of SP3113, heat treated at different temperatures. This data shows that CTO crystallizes at about 550 °C. Below this temperature, the samples are considered amorphous.....	68
4.5	Example of EDS data for SP3151.2b, after being heat treated at 650 °C with CdS in Ar. This sample shows the desired (Cd/Sn) ratio.....	69
4.6	An example of AFM imaging for SP3118.7. Note the boxes beneath image indicating both RMS roughness and Z range of the whole image and of the selected box within the left image. Each image is one square micron.....	71
4.7	Diagram showing the location of the contacts used to determine sheet resistance and Hall mobility.....	72
5.1	A diagram depicting how various cuts of the initial sample were labeled. The numbering corresponds to the initial cuts made of the sample, while the lettering corresponds to the sub-cuts of each numbered sample. All initial numbered samples are 1 inch wide by 2 inches tall. All lettered samples are 1 inch square.....	76
5.2	GIXRD data for CTO films deposited under 5 mT of pressure in a 1% oxygen environment at 25 °C and 300 °C. The rounded structures suggest small scale crystallization or amorphous structure.....	78
5.3	Direct band gap assessment for CTO films deposited under 5 mT of pressure in a 1% oxygen environment at 25 °C and 300 °C.....	79
5.4	Transmittance for CTO films deposited under 5 mT of pressure in a 1% oxygen environment at 25 °C and 300 °C.....	80

5.5	Optical constants for CTO films deposited at 10 mT and 25 °C, with varying oxygen.....	81
5.6	Indirect (left group) and direct (right group) band gap assessment for CTO films deposited at 10 mT and 25 °C, with varying oxygen.....	83
5.7	Transmittance for CTO films deposited at 10 mT and 25 °C, with varying oxygen.....	84
5.8	Growth rate versus oxygen content for CTO films deposited at 10 mT and 25 °C. The remaining percent of the atmosphere is argon gas.....	85
5.9	Optical constants for CTO films deposited in 1% ambient oxygen and 300 °C, with varying pressure.....	87
5.10	Optical constants for SLG and CSG glass. Note that all figures show a very small degree of variation.....	88
5.11	Transmittance for CTO films deposited in 1% ambient oxygen and 300 °C, with varying pressure.....	89
5.12	Indirect (left group) and direct (right group) band gap assessment for CTO films deposited in 1% ambient oxygen and 300 °C, with varying pressure..	90
5.13	Growth rate for CTO films deposited in 1% ambient oxygen and 300 °C, with varying pressure.....	92
5.14	Comparison of growth rate for the pressure dependent series and the oxygen dependent series. Argon pressure was determined for each series by calculating the partial pressure for an ideal gas.....	93
5.15	Optical constants for CTO films deposited at 10 mT and 25 °C, with varying oxygen. All samples heat treated at 600 °C.....	97
5.16	Transmittance for CTO films deposited at 10 mT and 25 °C, with varying oxygen. All samples heat treated at 600 °C.....	98
5.17	Indirect (left group) and direct (right group) band gap assessment for CTO films deposited at 10 mT and 25 °C, with varying oxygen. All samples heat treated at 600 °C.....	100
5.18	Optical constants for CTO films deposited at 10 mT, 10 % oxygen and 25 °C, with varying thickness. All samples heat treated at 600 °C.....	103

5.19	Direct band gap assessment for CTO films deposited at 10 mT, 10 % oxygen and 25 °C, with varying thickness. All samples heat treated at 600 °C.....	104
5.20	Transmittance for CTO films deposited at 10 mT, 10 % oxygen and 25 °C, with varying thickness. All samples heat treated at 600 °C.....	105
5.21	Optical constants for CTO films deposited at 5 mT, 5% oxygen and 25 °C, with varying heat treatment temperatures (solid) and environments (dashed).....	108
5.22	Direct band gap assessment for CTO films deposited at 5 mT, 5% oxygen and 25 °C, with varying heat treatment temperatures (solid) and environments (dashed).....	109
5.23	Transmittance for CTO films deposited at 5 mT, 5% oxygen and 25 °C, with varying heat treatment temperatures (solid) and environments (dashed).....	110

LIST OF TABLES

2.1	Comparison of electrical properties obtained by Wu for CTO to those of SnO ₂ formed using SnCl ₄ and SnO ₂ formed using Sn(CH ₃) ₄ chemistry. Both of these SnO ₂ samples were doped with fluorine and deposited by chemical vapor deposition. Electrical properties of indium tin oxide (ITO) [15] also shown for comparison. Table adapted from Wu [11].	8
4.1	Deposition conditions for CTO samples 112-151.	58
4.2	Heat treatment conditions for CTO samples 112-151.	61
5.1	Band gap values for samples deposited in atmospheres with varying oxygen percentage. Values are approximate.	83
5.2	Table of band gap values for samples deposited under varying pressure. Values are approximate.	89
5.3	A table depicting all deposition and heat treatment variables for the heat treated samples relevant to this work. Data regarding non-optical properties of the samples is also included. It should be noted that all samples were fitted using the VASE software to an MSE value of 10 or below.	96
5.4	Table of pre-heat treatment properties for all samples from Table (5.3).	97
5.5	Table of band gap values for samples deposited in atmospheres with varying oxygen percentage, after heat treatment. Values are approximate.	100
5.6	Electric properties of CTO produced by Wu, compared to SP3151 samples.	112

LIST OF ABBREVIATIONS

CAGR	- Compound Average Growth Rate
PV	- Photovoltaic
FIT	- Feed-in Tariff
CdTe	- Cadmium Telluride
CIGS	- Copper Indium Gallium Selenide
CTO	- Cadmium Stannate (Cadmium Tin Oxide)
TCO	- Transparent Conducting Oxide
FTO	- Fluorine Tin Oxide, (SnO ₂ :F)
VASE	- Variable Angle Spectroscopic Ellipsometry (Ellipsometer)
AFM	- Atomic Force Microscopy (Microscope)
GIXRD	- Grazing Incident X-Ray Diffraction
CdS	- Cadmium Sulfide
ITO	- Indium Tin Oxide
ZTO	- Zinc Tin Oxide
MSE	- Mean Square Error
SLG	- Soda Lime Glass
CSG	- Corning Specialty Glass
RMS	- Root Mean Square

TL	- Tauc-Lorentz
GLAD	- Gauss-Lorentz Asymmetric Doublet
SP3	- Sputtering System Number Three
PVD	- Physical Vapor Deposition
CBD	- Chemical Bath Deposition
CdO	- Cadmium Oxide
EDS	- Energy-Dispersive X-Ray Spectroscopy
Cd/Sn	- Cadmium to Tin Ratio
SEM	-Scanning Electron Microscope
VDP	- Van Der Pauw

ABSTRACT

In this research, the optical and electrical properties of cadmium stannate thin films were studied in order to determine how these properties depend on the deposition and heat treatment conditions used during film formation. Trends in band gap energy, transmittance, mobility, resistivity and carrier density were studied, as well as the growth rate and the indices of refraction and extinction. Optical data was primarily measured using variable angle spectroscopic ellipsometry. In the process of acquiring this data, a procedure for accurately determining the optical properties using variable angle spectroscopic ellipsometry was developed. Ultimately, samples achieved the highest quality when deposited in 5% atmospheric oxygen at room temperature and heat treated at 600 °C in contact with a cadmium sulfide layer in an argon atmosphere. It was found that oxygen content and film thickness may affect the heat treatment process, while temperature treatments below 600 °C will not sufficiently induce crystallization. Further study should be given to controlling the cadmium sulfide diffusion rate in order to optimize carrier density and mobility.

Chapter 1

INTRODUCTION

1.1 State of the World

With rising concerns about energy consumption and the exhaustion of fossil fuel supplies, interest in solar energy has substantially increased. Since 1979 solar energy has undergone a 33% compound average growth rate (CAGR) [1]. Currently, there are 32 GW of installed power from solar cells and in 2010 alone, 7.2 GW of power were installed [1]. All trends point towards a continuing rapid increase of worldwide installation of solar cells that are inexpensive and more efficient. In the United States alone, installed photovoltaic (PV) power increased 71 percent CAGR per year from 4 MW of power up to 290 MW between 2000 to 2008 [2]. These numbers are but a small fraction of the 3.9 TWh of electrical power [3] generated each year in the United States, but the rapid growth in recent years is a step in the right direction, away from non-renewable sources, such as oil and natural gas. Projections indicate that solar energy, which includes PV as well as solar thermal energy, will comprise 4.3% of the nation's power capacity by 2020, with PV expected to reach 30 GW of installed power [4].

As of 2007, rough estimates based on the average solar energy system put the cost per KWH of solar energy at around \$0.38 [5]. This includes rough estimates of power

output over a 25-30 year life expectancy, as well as the initial cost of the unit. This is still significantly higher than the present costs of coal, oil, and natural gas, which stand at \$0.006, \$0.05, and \$0.03, respectively. However, with increases in efficiency and reduction in cost, this cost per KWH is capable of falling dramatically. In early 2007, for example, Nanosolar announced its copper indium gallium selenide (CIGS) -based printable solar cell method, which will produce solar cells that will sell for around \$1.00 per watt [6]. By 2008 First Solar became the first company to produce solar cells at a capital cost of \$1.00 per watt, and by 2009, the cost was down to \$0.85 per watt [7]. This cost of \$1.00 per watt is often mentioned in the PV industry as the tipping point where solar power becomes cheaper than fossil fuels, after accounting for retail price and post-use costs associated with pollution and other environmental factors. This is just one example of substantial steps forward in cost reduction.

In addition to new methods of processing, governments are becoming more actively involved in green energy fields, with Feed-in Tariffs (FITs) becoming more frequent. FITs are the general grouping of laws designed to encourage utility companies to buy back renewable energy generated by all eligible participants at a reasonable rate. Germany, one of the first countries to implement FITs, also has one of the highest demands for solar power as well as one of the largest growths in installed solar power, for the year of 2009 [8].

Even without the help of government subsidies, grid parity, the point where generating alternative solar energy is equal in cost to grid power, is rapidly approaching. In very sunny regions, such as parts of California and Hawaii, grid parity is already a reality [9]. The rest of the nation is not far behind, and there is speculation that grid parity will be achieved in even cloudy areas by 2020.

While solar power isn't perfect, it may be the most promising of the newer sustainable green energy sources. Wind power, while currently cheaper than solar power, may be very limited by region whereas sunlight is fairly ubiquitous. Solar power has the most rapid growth of current energy sources, and is perhaps the cleanest as well.

1.2 Options

Knowing all of this, it is clear how important new facets of photovoltaic energy can be towards improving efficiency and simplifying production to reduce the cost per watt of installed PV. Typically, PV cells are made with crystalline silicon. Silicon has been shown to be an excellent material for solar cells, achieving module efficiencies near 20% [10]. However, these materials require fairly thick layers of silicon, around .2 mm, in order to function optimally. Materials such as cadmium telluride (CdTe) and CIGS allow for far thinner cells due to their high absorption coefficients over the wavelength range of solar maximum output.. The layer thicknesses for cells based off of these materials range from tens of nanometers to tens of microns, a considerable reduction in thickness from crystalline silicon. This reduction in thickness has the benefit of allowing

lighter, more flexible cells to be produced, as well as cost reduction benefits. Further, these thin film solar cells have lower manufacturing costs than crystalline silicon, as well as lower material costs. This large reduction in costs helps to drive down the price per watt of these solar cells despite having lower efficiencies, typically no higher than 16.5% in the case of CdTe [11].

Use of CdTe in particular has seen tremendous growth. The cells produced by First Solar, some of the cheapest produced at \$0.85 per watt, are cadmium telluride based cells. First Solar alone accounts for 13% of the global market share for PV, having installed 29% of the total installed PV for 2009 [12]. Despite this rapid growth, much can still be done to further increase efficiency of these cells while reducing costs. Replacing tin oxide with cadmium stannate, also known as cadmium tin oxide (CTO), is one aspect of device design that can impact efficiency. Using cadmium stannate as a transparent conducting oxide (TCO) in combination with CdTe produces better results than previously attempted TCOs [11] such as fluorine doped tin oxide (FTO) due to enhanced optical transmittance of the CTO/glass stack. To further increase the value of this material, methods for controlling properties and simplified processing must be discovered as well.

1.3 Thesis Statement

The goal of this thesis is to determine the relationship between the optical and electronic properties of cadmium stannate films and their deposition and post-deposition

processing parameters. Specifically, the coefficients of refraction and extinction and the resulting transmittance in structures on glass with RF sputtered films are characterized. The deposition conditions being independently varied include pressure, temperature, power and ambient atmosphere composition as well as post-deposition treatments conducted at various temperatures and in various ambient atmospheres. The optical analysis will be carried out using variable angle spectroscopic ellipsometry (VASE) to determine the optical constants n and k , the index of refraction and extinction, respectively. Electronic measurements will be carried out using the Hall effect and the van der Pauw method. Supporting measurements required for developing unique optical models include atomic force microscopy (AFM), spectrophotometry and grazing incidence X-ray diffraction (GIXRD).

Chapter 2

BACKGROUND

2.1 Cadmium Telluride Solar Cells

CdTe based solar cells have enjoyed a large degree of development in recent years [12]. CdTe's optical band gap of about 1.5 eV nearly perfectly matches the solar spectrum for PV energy conversion [11]. Further, due to its very high absorption coefficient of $5 \times 10^5 \text{ cm}^{-1}$, CdTe is able to absorb nearly all of the available photons with an energy greater than that of the band gap within a depth of 2 μm [11]. This allows for far thinner cells to be produced, which reduces production costs.

Currently, the majority of CdTe based solar cells are produced using p-type CdTe combined with an n-type cadmium sulfide (CdS) layer to form a heterojunction structure. Fluorine-doped tin oxide (FTO) is typically used as the TCO layer of the solar cell. These layers are deposited in reverse order on a glass substrate, with a metallic backing being applied to the CdTe layer. This device structure has remained the dominant CdTe solar cell structure for over 40 years [11] [13]. A cross section of this design can be seen in Figure (2.1). This device structure is capable of producing cell efficiencies of at least 15.8% [14].

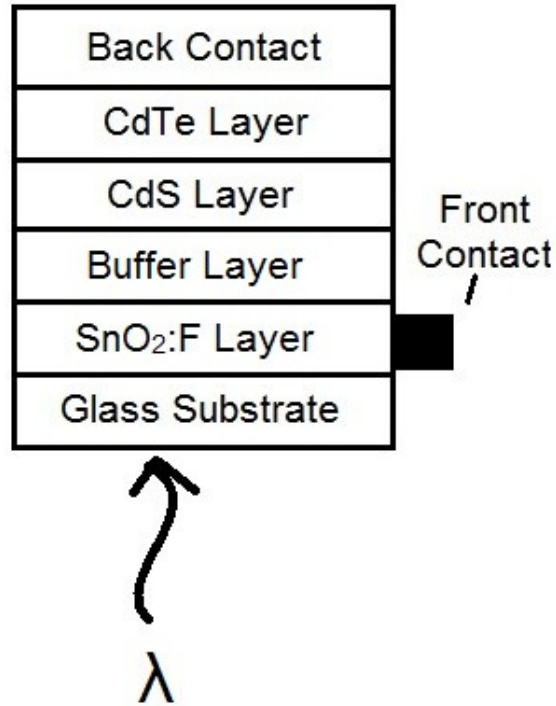


Figure 2.1: A diagram showing a cross-section of a traditional CdTe solar cell. Layers are not drawn to scale.

While this device structure is fairly robust and capable of producing cells with high efficiencies, the structure is ultimately limiting. As indicated by Wu et al., FTO films have an average transmission of only 80% with a sheet resistivity of $\sim 10 \Omega/\text{sq}$ [11]. Further, FTO has a fairly low band gap for a window layer semiconductor, at about 3.0 eV. This low band gap value causes undesirable absorption in the window layer, ultimately impacting cell efficiency.

2.2 Cadmium Tin Oxide

As a transparent conducting oxide, CTO has several distinct advantages over SnO₂. As seen in Table (2.1), CTO has electrical resistivity at least two times lower than SnO₂ films as well as far higher mobility and carrier concentration [11]. Because of the low resistivity, much thinner CTO films are able to be used in cell fabrication. The reduced thickness, combined with CTO's superior optical qualities, allows for far higher transmittance than the traditional FTO films [13], at close to 90%. These characteristics all make CTO a far more favorable material than SnO₂.

Table 2.1: Comparison of electrical properties obtained by Wu for CTO to those of SnO₂ formed using SnCl₄ and SnO₂ formed using Sn(CH₃)₄ chemistry. Both of these SnO₂ samples were doped with fluorine and deposited by chemical vapor deposition. Electrical properties of indium tin oxide (ITO) [15] also shown for comparison. Table adapted from Wu [11].

Material	Thickness (nm)	carrier density (cm ⁻³)	mobility (cm ² /Vs)	Resistivity (Ωcm)	Sheet Resistance (Ω/sq)
CTO	510	8.94 x 10 ²⁰	54.5	1.28 x 10 ⁻⁴	2.6
SnO ₂ (SnCl ₄)	~1000	4.95 x 10 ²⁰	15.4	8.18 x 10 ⁻⁴	8.6
SnO ₂ (SnCH ₃) ₄)	~1000	4.52 x 10 ²⁰	42	3.29 x 10 ⁻⁴	3.3
ITO	610	2.6 x 10 ²⁰	17.4	1.38 x 10 ⁻³	22.6

Further, CTO has a strong potential to obtain high mobility, which can allow for lower carrier concentration and consequential reduction in free carrier absorption. High carrier concentration is thought to be responsible for high free-carrier absorption in the

near infra red part of the solar spectrum [16]. The combination of these beneficial traits mean that there is more flexibility in choosing parameters of the TCO, such as the thickness. This increase in freedom allows for a greater variety of deposition and heat treatment parameters to be used, ultimately allowing the CTO layer to be adjusted to a number of different configurations.

2.3 New Cadmium Telluride Device Structure

Ultimately, Wu has proposed a rethinking of the classic CdTe device structure. The new variation of the structure uses CTO as the new TCO layer, as well as using a zinc tin oxide layer (Zn_2SnO_4 or ZTO) as a buffer layer between the TCO and the CdS layer. The CdS layer is also now oxygenated, to raise the band gap [11]. It should be noted that this CdS oxygenation may not be intact after cell processing. This model can be seen in Figure (2.2). Using this device structure, a record setting 16.5% efficiency was achieved [11]. This new model will not be discussed at length in this paper. Ultimately, further work regarding this model shall be conducted, in order to confirm and improve upon this work.

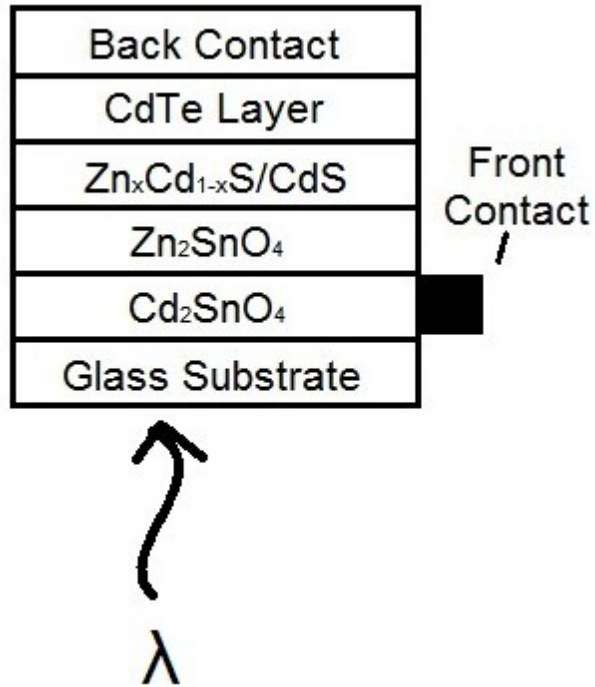


Figure 2.2: A diagram showing a cross-section of the CdTe solar cell as proposed by Wu. Note the $Zn_xCd_{1-x}S/CdS$ layer. This is a by-product of interdiffusion between the ZTO and CdS layer and is actually beneficial in the working of this device structure [11]. Layers are not drawn to scale.

Chapter 3

ELLIPSOMETRY

3.1 Overview

Ellipsometry is a powerful established tool for measuring surfaces and thin films, due to the way it makes use of polarized light [17] [18] [19]. When linearly polarized light is reflected from a flat dielectric or metal, the resulting light is elliptically polarized. Ellipsometry effectively measures this change in polarization state of the light. The basis of this technique is the measurement of the ratio of p- polarized light, light perpendicular to the sample surface in the plane of incidence, to s- polarized light, light parallel to the sample. Typically, when discussing polarized light, the important features include the amplitudes as well as the phase. If components are in phase, the light is linearly polarized. If they are ninety degrees out of phase, they are circularly polarized. In general, these two states are very specific. Most likely, the components will be neither in phase nor perfectly ninety degrees out of phase, or the amplitudes of the components will not be equal. For this more general case, an ellipse is carved out as the light propagates through space. Ellipsometry then, is the measurement of this ellipse.

The power of ellipsometry comes from its comparative measuring. Due to the ratio nature of the data, ellipsometry is very sensitive to minute changes, allowing for a

very high resolution. Material layers as thin as a few angstroms are resolvable using this technique. As mentioned earlier, ellipsometry measures the ratio of p-polarized light to s-polarized light. This is accomplished by measuring the ratios of the magnitudes of the total reflection coefficients, described by Fresnel, of these polarization states as well as the phase shift between these polarization states induced by the reflection. The ratio of the total reflection coefficients is defined such that

$$\tan \Psi \equiv \frac{|R^p|}{|R^s|} \quad (3.1)$$

where R^p and R^s are the total reflection coefficients for the p- and s-polarized states, respectively, and Ψ is an angle whose tangent is equal to this ratio. Further, the phase shift is defined such that

$$\Delta \equiv \delta_1 - \delta_2 \quad (3.2)$$

where δ_1 is defined as the phase difference between the components of the light before reflection from a surface, and δ_2 is the phase difference after reflection. Ψ and Δ are the parameters actively measured by the ellipsometer. Data for Ψ ranges from 0° to 90° and data for Δ ranges from -180° to 180° . These two equations can be easily combined into a single equation, containing both phase and amplitude information before and after reflection.

$$\rho = \tan(\Psi) e^{i\Delta} \quad (3.3)$$

Where ρ is now defined as the complex reflectance ratio. This is the fundamental equation of ellipsometry [20].

Knowledge of ρ allows for the calculation of dielectric constants for the materials comprising the sample being studied. In the simplest 'two-phase' model, this is done using equation (3.4).

$$\frac{\tilde{\epsilon}}{\epsilon_a} = \sin^2 \phi \left[1 + \left[\frac{(1-\rho)}{(1+\rho)} \right]^2 \tan^2 \phi \right] \quad (3.4)$$

where $\tilde{\epsilon}$ is the complex dielectric for the material and $\tilde{\epsilon}_a$ is the complex dielectric for the ambient environment, usually air [17] [19] [21]. $\tilde{\epsilon}$ is defined as

$$\tilde{\epsilon} = \epsilon_1 + i \epsilon_2 \quad (3.5)$$

where ϵ_1 and ϵ_2 describe the behavior of the material upon being probed with light.

Generally, the optical constants for refraction and extinction are considered more useful, since they relate directly to the interaction between the light doing the probing and the pure materials being probed. These values easily relate to the complex dielectric by

$$\tilde{\epsilon} = \tilde{N}^2 = (n - ik)^2 \quad (3.6)$$

where \tilde{N} is defined as the complex index of refraction [20]. In this fashion, an accurate description of the optics of the materials being studied can be obtained.

However precise it may be, ellipsometry is not a direct measurement system. Values for Ψ and Δ are obtained at various angles of incidence and over a spectrum of wavelengths. This polarization data then needs to be fitted to a model which approximates the general form of the sample. The user sets up an initial model using approximations for the unknown parameters. Through an iterative process, a computer program generates values of Ψ and Δ , attempting to match these values to the recorded

data from the ellipsometer. In doing so, the parameters which describe the material layers are varied slightly until the Ψ and Δ data generated matches the experimentally obtained data and an accurate understanding of the various variables is established. It is for this reason that accuracy of the initial model is incredibly important. All factors of the model are taken into consideration, and many assumptions are made with regards to the actual properties and behaviors of various aspects of the model. There are several different methods for dealing with these assumptions when they do not fit the physical reality of the sample.

Due to the noninvasive nature of ellipsometry, it has proven incredibly useful in determining various characteristics of a sample, without altering the sample itself. The models generated by the data are able to determine the thickness of a sample, as well as the inherent optical properties of a sample, such as n and k . As long as the model used to describe the sample is accurate, the accuracy of these measurements is extremely high. Ellipsometry also allows for a reasonable estimate of the surface roughness of a sample to be made. These properties, in particular the optical constants, will be the primary focus of the work done with the ellipsometer.

3.2 Obtaining Data

3.2.1 Equipment

The setup being used here is a variable angle spectroscopic ellipsometer from J. A. Woollam Co, as pictured in Figure (3.1). Not shown are the 75W HS-190 monochromator and the fiber optic cable with a spectral range from 240-1700 nm.

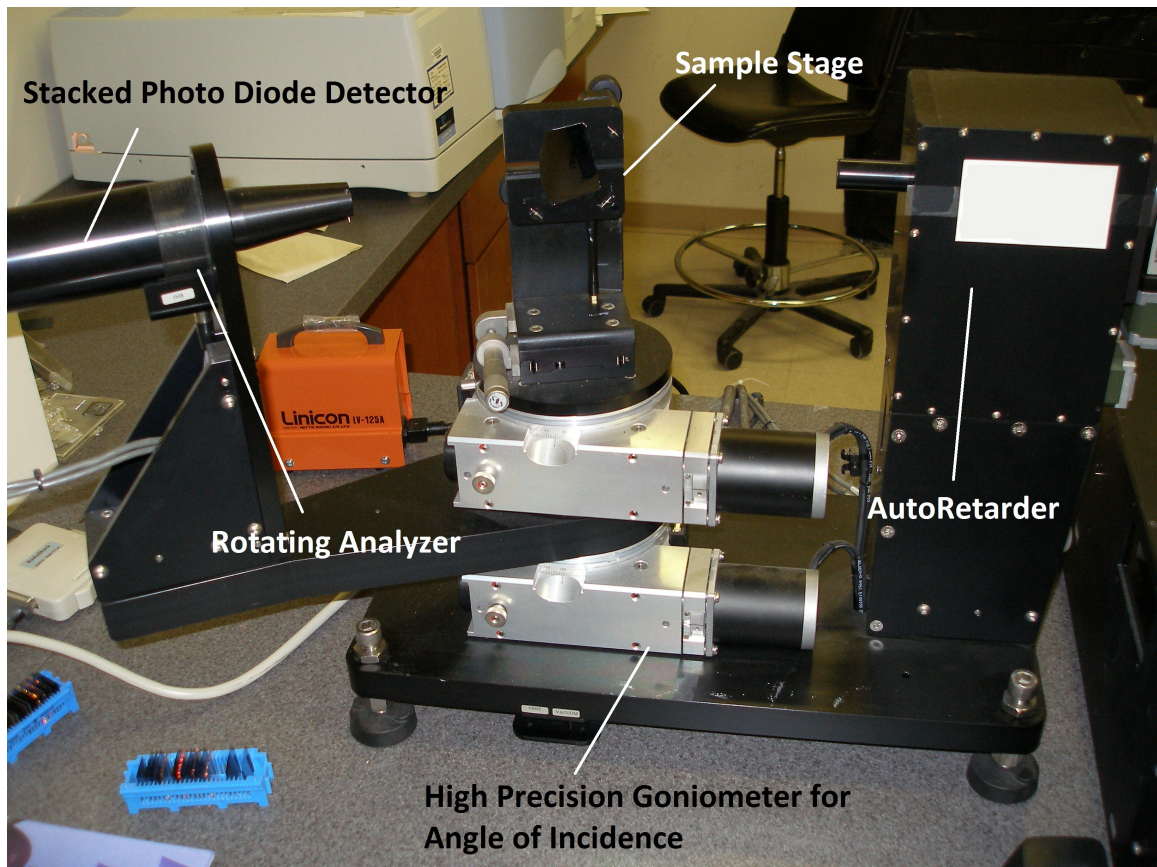


Figure 3.1: The Institute of Energy Conversion's variable angle spectroscopic ellipsometer. A calibration sample is currently affixed to the sample stage. Not pictured is the device's input polarizer, to the right of the AutoRetarder. The Institute's UV/VIS spectrophotometer is visible in the background.

Also shown in this image are the Linicon LV-125A pump, designed to hold a sample to the vertical sample stage, as well as the UV/VIS spectrophotometer in the background. This setup allows for the most flexibility with parameters, providing the ability to independently select various wavelengths, angles of incidence and even incoming polarizations, as desired.

This setup makes use of a rotating analyzer, which is able to determine the component amplitudes and phase difference of the reflected light. An AutoRetarder is also used to reduce inaccuracies in the Δ measurement. Since the ellipsometer is directly measuring $\cos(\Delta)$, a large degree of uncertainty is present when Δ is close to 0° or 180° . The AutoRetarder induces a 90° shift in Δ . Comparing $\cos(\Delta)$ to $\cos(\Delta-90^\circ)$ allows for accurate determination of the correct value of Δ .

3.2.2 The Brewster Angle

The initial step before Ψ and Δ data can be taken is to determine the Brewster angle. The Fresnel equations indicate that the Brewster angle is when the reflection from the p- polarized light has a magnitude of zero, allowing only s- polarized light to be reflected from the surface [20]. This is achieved when the indices of refraction for the two sides of the interface can be described as in equation (3.7).

$$\theta_B = \arctan\left(\frac{n_2}{n_1}\right) \quad (3.7)$$

Due to ellipsometry's comparative nature of measurement, achieving the greatest contrast between the reflected p- and s- polarized light tends to yield the greatest sensitivity to change in the data, allowing for more accurate results. Because of this, the Brewster angle is a natural choice of angle at which to collect data, since the p- polarized light is maximally absorbed, allowing for the greatest contrast between the two components, and thus, the greatest sensitivity. However, the Brewster angle itself is a function of the indices of refraction of the materials comprising the interface. In addition, for most materials the index of refraction varies with wavelength. Thus, the Brewster angle is a function of wavelength [20].

$$\theta(\lambda)_B = \arctan\left(\frac{n(\lambda)_2}{n(\lambda)_1}\right) \quad (3.8)$$

In order to circumvent using a fixed wavelength, the Brewster angle is determined for large values of wavelength as well as for small values. Ultimately, an average value of the Brewster angle can be determined, as well as an effective range. This 'Brewster angle range' allows for several Ψ and Δ series to be taken at angle values that will maximize the accuracy of the data.

3.2.3 Calibration Procedure

Once a sample is ready to be measured the first step is to calibrate the system. The sample is secured to the measurement stage via the vacuum pump, and the sample is aligned in the X, Y and Z coordinates to achieve maximum intensity of the incident light

beam. This must be done each time a sample is affixed to the sample stage, to ensure the maximum amount of light reaches the detector.

Due to the ratio nature of ellipsometry, there is little more in the way of actual calibration. However, a standard sample, in this case a silicon wafer, still needs to be measured to ensure consistency of data between each run. The calibration process is automatic and fairly straightforward. Once the numbers are checked and in rough agreement with previous data runs, it is safe to proceed.

3.2.4 Brewster Angle Determination

Once the ellipsometer is calibrated and the sample to be measured has been affixed, the Brewster angle can be determined. Data for the Brewster angle is taken with a varying angle of incidence at two separate wavelengths. The angle of incidence varies from 45° to 80° at 1° intervals. One series is taken with a wavelength of 500 nm and one is taken with a wavelength of 1500 nm. This gives a fairly large spread and with it a fairly good understanding of where the Brewster angle range is. A few additional options should be toggled as well, before starting this data run. The option to skip any range of wavelengths should be unchecked. In addition, great accuracy is not required in determining the Brewster angle range, so grating changes should be split across the angles, to allow for faster scanning.

Once the data has finished being taken, a representative graph will display on the screen showing Ψ as a function of angle for each wavelength value. Looking at the two Ψ curves, it should be fairly obvious where each of their minima are. An example of this is shown in Figure (3.2). Once the minima are determined, the range of the Brewster angle can be estimated. Typically, Ψ and Δ data are taken at the mean of the Brewster angles, as well as $\pm 5^\circ$. These three angle values will usually fall within the Brewster angle range, allowing for a high degree of accuracy in the measured Ψ and Δ data.

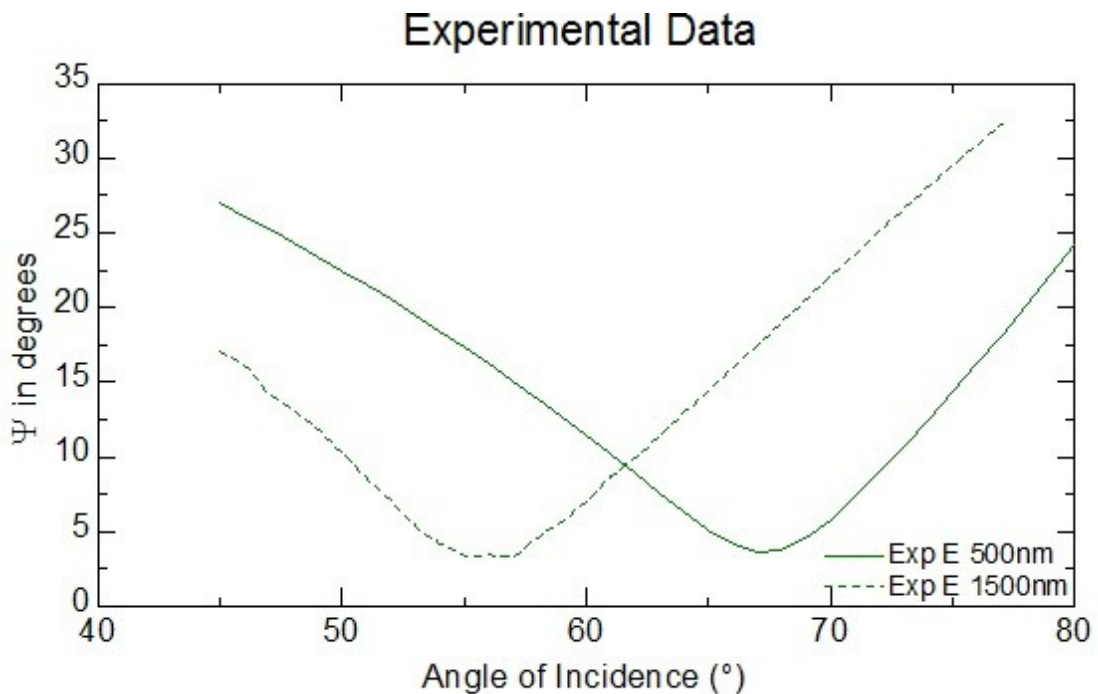


Figure 3.2: An example of Brewster angle determination for sample SP3147.7. Here, due to the near identical minimum values of the Ψ curves, the Brewster angle can be assumed to be evenly spaced between the two minima, at approximately 62° .

3.2.5 Ψ and Δ Data Obtained

After taking this initial Brewster angle determination run, Ψ and Δ data are ready to be taken. It is important to adjust the measurement parameters to agree with the actual sample. Doing so allows for the data to be modeled more accurately later on. Since the samples of interest are deposited on glass, and glass has a depolarizing effect on light, selecting “Isotropic + depolarization” during the options section of this data run is very important to accurately capture the physical properties of the sample. Dynamic averaging should also be enabled, to reduce noise in the data. Unlike the first 'Brewster' run, there is no need for grating changes to be split across the angles, so this option should be unchecked. Once again, no wavelengths should be skipped as nothing currently being dealt with involves cables being in the way. Finally, the data range should be selected. Data should be taken from 1.1 to 4 eV every .025 eV. In terms of wavelength, this is about 310nm to 1127 nm. This level of resolution is enough to accurately model the data in the next steps.

3.3 Building a Model

3.3.1 Minimization

Once clean, smoothly varying data for Ψ is obtained, a model can be constructed and attempts can be made to begin fitting the data to the model. Ultimately, this process should yield accurate values for thickness, roughness, and the optical constants n and k . Once a model is constructed, the VASE software package, provided by J.A. Woollam, iteratively minimizes the mean square error (MSE) of the fit of the generated data to the

experimental data. The MSE is given in equation (3.9).

$$MSE = \frac{1}{2N - M} \sum_{i=1}^N \left[\left(\frac{\Psi_i^{mod} - \Psi_i^{exp}}{\sigma_{\Psi,i}^{exp}} \right)^2 + \left(\frac{\Delta_i^{mod} - \Delta_i^{exp}}{\sigma_{\Delta,i}^{exp}} \right)^2 \right] = \frac{1}{2N - M} \chi^2 \quad (3.9)$$

Here, N is the number of (Ψ, Δ) pairs, M is the number of variable parameters in the model, and σ are the standard deviations on the experimental data points. χ is also defined in equation (3.9). As seen in the equation, MSE is represented by the sum of the squares of the differences between the experimental and the generated data, with each difference weighted by the standard deviation of that measured point [22]. Naturally, the smaller the MSE the more likely it is that the model agrees with the experimental data. Only one set of parameters should yield this MSE value. Uniqueness is a very important point to test for in the minimization process.

The software employs the Levenberg-Marquardt algorithm for all minimizations, including the calibration data. The Levenberg-Marquardt method is interesting, in that it combines aspects of two other prominent algorithms, known as the gradient method and the inverse Hessian method. Both of these methods are useful for reducing the MSE, however, they come with penalties. Before proceeding, it will be important to establish some definitions. Let all of the measured data points be defined as y_i , where each y_i is either a measured value of Ψ or Δ. The same value as denoted from the generated model will be defined as $y(x_i; \vec{a})$, with x_i representing all model parameters and the vector \vec{a} consisting of all variable model parameters, where each element of \vec{a} is a parameter, denoted individually as a_j , where j ranges from 1 to M [22].

The gradient method, as its name implies, uses a gradient of the slope of the MSE surface to find the minimum value. The elements of the gradient vector are given by

$$\frac{\partial \chi^2}{\partial a_k} = -2 \sum_{i=1}^N \left[\frac{[y_i - y(x_i; \vec{a})]}{\sigma_i^2} \cdot \frac{\partial y(x_i; \vec{a})}{\partial a_k} \right] \quad (3.10)$$

From this β is defined.

$$\beta_k \equiv -\frac{1}{2} \frac{\partial \chi^2}{\partial a_k} \quad (3.11)$$

In order to take a step in the direction of the gradient on the MSE surface, the current values of the parameters are adjusted by adding a multiple of the gradient, in the fashion of

$$\vec{a} = \vec{a} + \text{const} \cdot \vec{\beta} \quad (3.12)$$

which can be further reduced to its simplest form.

$$\delta a_l = \text{const} \cdot \beta_l \quad (3.13)$$

Equation (3.13) sums up the fundamental idea behind the gradient method.

This process relies on the constant to determine how large the step size should be for each attempt at a minimization. However, the problem with this method is there is no accurate way to determine the step size. If too small of a value is selected the MSE will be improved only slightly, causing many iterations to be required. If too large of a value is selected the algorithm will overshoot the minimum, perhaps many, many times [22].

The inverse Hessian method is a second form used for minimizing the MSE of a given model. Near the minimum value, it can be expected that the MSE will look very similar to a quadratic function, since the MSE is a sum of squares as previously seen in equation (3.9). Since this is the case, it is possible to write χ^2 as an approximation.

$$\chi^2(\vec{a}) \approx y - \vec{d} \cdot \vec{a} + \frac{1}{2} \vec{a} \cdot \vec{D} \cdot \vec{a} \quad (3.14)$$

Here, \vec{d} is an M-component vector and \vec{D} is an M x M matrix. If this is a reasonable approximation to make, equation (3.14) naturally leads to the conclusion that the MSE minimum value will occur at values of the parameters as follows.

$$\vec{a}_{min} = \vec{a}_{cur} + \vec{D}^{-1} \cdot [-\vec{\nabla} \chi^2(\vec{a}_{cur})] \quad (3.15)$$

If this approximation is close or exact, then naturally equation (3.15) will give a very good value for the location of the minimum value of the MSE. If the approximation in (3.14) is a bad approximation, then equation (3.15) will not give good values for the MSE and in fact will yield values of the parameters which may or may not improve the MSE.

In order to evaluate the matrix \vec{D} mentioned above, it is necessary to take the partial derivative of χ with respect to the parameters.

$$\frac{\partial^2 \chi^2}{\partial a_k \partial a_l} = 2 \sum_{i=1}^N \left[\frac{\partial y(x_i; \vec{a})}{\partial a_k} \frac{\partial y(x_i; \vec{a})}{\partial a_l} - [y_i - y(x_i; \vec{a})] \frac{\partial^2 y(x_i; \vec{a})}{\partial a_k \partial a_l} \right] \quad (3.16)$$

Here we define α_{kl} as in equation (3.17).

$$\alpha_{kl} \equiv \frac{1}{2} \frac{\partial^2 \chi^2}{\partial a_k \partial a_l} \quad (3.17)$$

Finally, the adjustment vector, which needs to be added to the current parameter vector to move the minimum, can be calculated by solving the below system of linear equations.

$$\sum_{l=1}^M \alpha_{kl} \delta a_l = \beta_k \quad (3.18)$$

In general, the inverse Hessian method is best applied in situations where the starting point of the calculation is close to the minimum. The farther away from the minimum, the more likely the method is to fail, as the quadratic approximation no longer holds true [22].

The Levenberg-Marquardt method, as mentioned earlier, is the method of minimization used by the software. It elegantly combines the inverse Hessian method with the gradient method, providing a means to interpolate between the two. This method centers around the constant first mentioned in equation (3.12). Previously it was mentioned that this constant had to be guessed at, with no means for estimating its size. Marquardt determined that the Hessian matrix should provide some information relevant to the value of the unknown constant from the gradient method [22].

In order to derive the Levenberg-Marquardt method, it is wise to start with a balancing of dimensions. The elements of gradient vector β_k have the inverse dimensions of the corresponding parameters. Thus, it is clear that the much discussed constant from equation (3.12) must have dimensions of a_k^2 . The only quantity in the $\vec{\alpha}$ matrix that will

satisfy this requirement is the reciprocal of the diagonal element corresponding to the k^{th} variable. Thus, it is clear that the constant in question can be represented as follows in equation (3.19).

$$\delta a_l = \frac{\beta_l}{\lambda \alpha_{ll}} \quad (3.19)$$

Here, λ stands for a numerical constant that has not been determined yet. A new $\vec{\alpha}$ matrix, different from the original $\vec{\alpha}$ and now denoted $\vec{\alpha}'$, is now defined.

$$\begin{aligned} \alpha_{jj}' &\equiv \alpha_{jj}(1 + \lambda) \\ \alpha_{jk}' &\equiv \alpha_{jk} \text{ (if } j \neq k) \end{aligned} \quad (3.20)$$

Thus, the gradient method and the inverse Hessian method can be combined by replacing equations (3.13) and (3.18) with the following expression [22].

$$\sum_{l=1}^M \alpha_{kl}' \delta a_l = \beta_k \quad (3.21)$$

This equation is the Levenberg-Marquardt algorithm. Here, the constant λ now is given the name of the Marquardt parameter. It is important to note that when the Marquardt parameter is very large, equation (3.21) reduces to equation (3.13), also known as the gradient method. And when the Marquardt parameter is zero, equation (3.21) reduces to equation (3.18), also known as the inverse Hessian method. Thus, it is clear that the Levenberg-Marquardt method allows us to shift smoothly from one method of minimization to the other, allowing for optimal minimization. A typical approach for a minimization run is as follows.

1. Choose a value of the Marquardt parameter and calculate the adjustment to the parameters.
2. Calculate the new MSE at the adjusted values of the variables.
3. If the MSE is improved, divide the Marquardt parameter by ten and repeat the process. This shifts the algorithm towards the inverse Hessian method. If the MSE is not improved, revert back to the original values and multiply the Marquardt parameter by ten. This shifts the algorithm towards the gradient method.
4. When multiple iterations are unable to improve the MSE, convergence is attained, and the process stops. Other parameters can be set to stop this as well, including having the MSE improve by a smaller amount than a limiting bound, or a predetermined number of iterations passing [22].

In general, the Levenberg-Marquardt method is extremely robust. It is able to determine the best avenue for minimization, via self-consideration of the λ constant. In this way the algorithm can choose the most efficient route to minimization, allowing for a quick process with the least amount of time wasted when the MSE is very close or far from the minimum. The main drawback with this method is the tendency for the algorithm to settle on local minima of the MSE surface instead of the extreme minima, forcing incorrect results. A good idea to help avoid this is to test various and widely separated initial guesses for the parameters to test the plausibility of the MSE value. This will be discussed later.

3.3.2 The Layers

After collecting data for a sample according to the established standard operating procedure, the process of fitting the data to an established model is attempted. Typically these models consist of three sets of layers. These are as follow.

1. The substrate, a glass layer approximately 1.5 mm thick. Depending on the samples this is either commercially obtained Glaverbel soda lime glass (SLG) or a Corning specialty glass (CSG). Establishing an accurate set of optical constants for these materials will be discussed shortly.
2. The Material layer. This layer consists of the material or stack of materials being modeled. This layer contains the actual data of interest, and must be as exactly replicated as possible in the model in order to glean this information from the generated data. This layer has a variable thickness.
3. The surface layer. This layer consists of any surface effects present. Almost always, this layer involves only surface roughness. On occasion, it may include a surface oxidation layer. This layer is usually allowed to be fitted, but data from the AFM confirms that the root mean square (RMS) surface roughness is typically no more than 1 nm.

3.3.2.1 Substrate

In order to accurately factor in the substrate layers, a separate data run needs to be taken with a bare substrate. In this way, the optical constants of the glass being used can be accurately factored into the overall model. This process is very simple and painless. After repeating the data taking steps mentioned earlier, but now for a bare piece of glass, the data is fit, using only one layer. The software contains many different bulk predetermined optical constants, including several types of glass. Luckily, they are all similar enough that one may be used as a basis for the glass in question, either SLG or CSG.

After inputting the correct thickness, the quickest way to a fit is to immediately allow both optical constants to be fit and then run a normal fit. This will minimize the values of n and k for each individual data point measured. For example, an average data

series for CTO has 117 points of data over the range from 1.1 to 4 eV, so there will be 234 simultaneous minimizations. This method typically isn't accurate enough to do for any other samples, however glass is simple enough of a sample that this accurately captures the optical properties alone. Once finished running the fit, a visual check can confirm the accuracy of the optical constants. These parameters are now ready to be saved and called up later when building the rest of the models. All of the glass substrates used, SLG and CSG both, were 1.5 mm thick.

3.3.2.2 Material Layer

The three most common models used to fit our CTO layer all involve oscillator models. One involves the Tauc-Lorentz (TL) oscillator. This oscillator models the dielectric function of many amorphous materials particularly well. The second involves the Gauss-Lorentz Asymmetric Doublet (GLAD) oscillator. This oscillator is good for modeling absorbing spectral regions that have a shoulder [22]. The third is the basic Gaussian oscillator model, which can be used for most samples of CTO fairly well and is thus an excellent gauge of accuracy of constants.

Most often, the TL model is sufficient to accurately model the sample data, if it is amorphous. Once there is crystallization involved in the sample, the GLAD and pure Gaussian models are better able to model the samples, with the GLAD model being less reliable than the simple Gaussian more often than not. This shift in oscillator model is likely due to the more complex and large scale crystal structure generated during heat

treatment. The thickness of the material layer is highly variable, and should be verified via other sources, if possible. Several samples were able to be measured with a Dektak system. However, for the majority of the samples this was not the case. Estimates based on deposition time were used to estimate the thicknesses of the sample layers.

3.3.2.3 Surface Layer

The roughness layer is actually a composite layer between two separate layers, One of which is a void layer, and other being whatever layer is directly below the roughness layer. These layers are blended together using a formula known as the effective medium approximation.

$$\sum_i f_i \frac{\epsilon_i - \epsilon_e}{\epsilon_i + (n-1)\epsilon_e} = 0 \quad (3.22)$$

Where n indicates the spatial dimensions of the model, f_i indicates the fraction of each component, ϵ_i indicates the complex dielectric function of each constituent material, and ϵ_e indicates the effective complex dielectric function [23]. It is important to keep in mind that the complex dielectric function is intimately tied to the optical constants of a material, as discussed in section 3.1.

These roughness layers work fairly well as fine tune adjustments to data and should be similar to measured values of roughness from the AFM. However, the model values are often not particularly close to these measured values which may indicate other things happening, such as correlation between other factors and the roughness layer. The

roughness layer is generally important in modeling TCOs, such as CTO, for this very reason. The addition of a roughness parameter allows for better fits of these materials, which are often graded through the material layer. In general, if the roughness layer is ever registered as a zero thickness, or significantly greater than a few nanometers thick, it is a strong possibility that the roughness data is skewed by some other variables and should not be interpreted as real.

In addition to the surface roughness, certain materials may oxidize slightly on the surface. In order to fully understand the sample in question, surface oxidation layers should be taken into consideration, if needed. Fitting such a layer usually requires a preexisting bulk sample data set in the computer system, as fitting thin films of surface oxidation may prove tricky to capture. If data already exists, it is a matter of simplicity to add a new layer to the model with the roughness layer added on top of this oxidized layer. Thickness for surface oxidation should be very small, no more than a nanometer or two, at the largest. Other effects, such as water absorption at the surface, can also be modeled in this fashion.

3.3.3 Oscillator Models

When considering model construction, it is important to begin with a basic model. The simplest picture for light propagating through a solid is the classical model of dipole oscillators. In this model, the material is composed of dipole oscillators which can be used to represent a lattice structure or atomic interactions in general. At optical

frequencies, the dominant response is from the oscillations of bound electrons, and thus can be expressed classically using the Lorentz oscillator model. The motion of an electron bound to a nucleus driven by an oscillating electric field is given by [20].

$$m \frac{d^2 \vec{r}}{dt^2} + m \Gamma \frac{d \vec{r}}{dt} + m \omega_0^2 \vec{r} = -eE \quad (3.23)$$

Here, m is the electronic mass, e is the electric charge and ω_0 is the resonant frequency. The first term in this expression represents the acceleration of the particle. The second term represents damping due to scattering. The third term represents the Hooke's law restoring force. The driving force \vec{E} is simply the incident light. The electric field \vec{E} is taken to vary in time as per $e^{-i\omega t}$, and it is assumed that \vec{r} will have the same time variation. Thus, the solution to equation (3.23) is as follows.

$$\vec{r} = \frac{eE/m}{(\omega_0^2 - \omega^2) - i\Gamma\omega} \quad (3.24)$$

It is well known that the dipole moment can be written as

$$\vec{p} = e \vec{r} \quad (3.25)$$

where e is the charge value of the dipole, and \vec{r} is the distance between the charges.

It is also well known that, due to the small displacement, a linear proportionality exists between the dipole moment and the field. This proportionality is known as the atomic polarizability and is defined as

$$\vec{p} = \tilde{\alpha}(\omega) \vec{E} \quad (3.26)$$

where the atomic polarizability is frequency dependent. Using these two equations, it is

possible to write equation (3.24) in terms of the atomic polarizability.

$$\tilde{\alpha}(\omega) = \frac{e^2}{m} \frac{1}{(\omega_0^2 - \omega^2) - i\Gamma\omega} \quad (3.27)$$

Further, since it is well known how the dielectric function relates to the atomic polarizability, equation (3.27) can be written as

$$\tilde{\epsilon} = 1 + \frac{4\pi Ne^2}{m} \frac{1}{(\omega_0^2 - \omega^2) - i\Gamma\omega} \quad (3.28)$$

where $\tilde{\epsilon}$ represents the complex dielectric function and N represents a given number of oscillators. This can easily be split up into the real and imaginary components using equation (3.5) or, more usefully, they can be written in terms of the optical constants as described by equations (3.5) and (3.6). Thus, the optical constants are obtained [20].

$$\begin{aligned} n &= \sqrt{\frac{1}{2} [(\epsilon_1^2 + \epsilon_2^2)^{1/2} + \epsilon_1]} \\ k &= \sqrt{\frac{1}{2} [(\epsilon_1^2 + \epsilon_2^2)^{1/2} - \epsilon_1]} \end{aligned} \quad (3.29)$$

In this way, it is possible to build optical constants mathematically out of an oscillator function. By using a well defined function such as this Lorentz oscillator, a minimizing fit is able to focus fit conditions on the parameters that define the oscillator, where the oscillator is mathematically linked to the optical constants. This is a much better fit technique than a point by point fit of the optical constants, where each individual data point is fit. Since the data is based on oscillators, the final functions

describing n and k are much more likely to be smoothly varying, and thus, more likely to be real. There are some downsides to this method though. Namely, if the oscillator function used to describe the optical constants doesn't reflect on the actual optical constant curves, then the fit will not yield useful data.

It should be noted that the Lorentz oscillator is an ideal situation. Although the Lorentz oscillator has been highlighted here as an example of the mathematical reasoning behind using such oscillators in the modeling, it was not actually used in any of the data fitting in this project, for this very reason. Other oscillators were chosen and applied to this same system, either due to the mathematical reasoning behind an oscillator allowing for a better fit between the oscillator and the data, or more simply, empirical evidence showed a certain oscillator was able to describe the behavior of the data.

For example, the Gaussian oscillator is much better at fitting amorphous and glassy films, as well as polycrystalline materials due to the Gaussian distribution of the absorption bands in these materials [24]. For this reason, it is well suited to the materials in this project. The Gaussian oscillator model is as follows.

$$\begin{aligned}\varepsilon_2(E) &= Amp \cdot \left(e^{-\frac{(E-E_n)^2}{\sigma}} - e^{-\frac{(E+E_n)^2}{\sigma}} \right) \\ \varepsilon_1(E) - 1 &= \frac{2}{\pi} P \int_0^{\infty} \frac{\xi \varepsilon_2(\xi)}{\xi^2 - E^2} d\xi \\ \sigma &= \frac{Br}{2\sqrt{\ln(2)}}\end{aligned}\tag{3.30}$$

The parameters that are fit by the software are the amplitude (Amp) center Energy (E_n) and the broadening of the absorption peak (Br), which is the Full-Width-Half-Maximum value of the curve. Here, P denotes the Cauchy principle value. The Gaussian model is much more useful for our data, since the Gaussian model rapidly approaches zero beyond $E_n \pm Br$, for ϵ_2 [24]. This allows the Gaussian model to model materials which are transparent over a limited portion of the measured spectral range.

On the other hand, the TL oscillator is a strong example of an empirical optical model. Many data sets were fit using this model, however there is no mathematical reasoning for this model describing data, other than it reflects the shape and structure of actual amorphous optical constants. The TL model is as follows.

$$\epsilon_2(E) = \frac{AE_0\Gamma(E-E_g)^2}{E[(E^2-E_0^2)^2+\Gamma^2E^2]}\Theta(E-E_g) \quad (3.31)$$

This expression has 4 parameters: the band gap E_g , the peak in the joint density of states E_0 , the broadening parameter Γ , and the prefactor A which includes the optical transition matrix elements [25].

It should be noted that there is no equation mentioned for ϵ_1 for the TL model. This is because it is identical to the value of ϵ_1 for the Gaussian model, which is a Kramers-Kronig integration. This is not actually a coincidence, but an important feature of optical modeling, called Kramers-Kronig consistency. In general, simple terms, Kramers-Kronig consistency is used to calculate the real component of the dielectric

function after the imaginary component is described by the oscillator [26]. If an oscillator is Kramers-Kronig consistent, it is a strong candidate to model a real physical response system, as the Kramers-Kronig relationship strongly implies the causality of the relationship between the two equations holds.

The GLAD oscillator model is the third main oscillator model used in describing the data. Primarily, it was used as a starting point, since previous projects involving CTO were fit using the GLAD model. The primary feature of the glad model is a duo of Gauss-Lorentz oscillators tied to some center energy. These oscillators are allowed to spread away from each other and to be fit with peaks of different values, allowing for a shoulder function to be modeled. This ability to represent absorbing spectral regions with a shoulder is its primary advantage, one that our CTO data has no great need for. Each of the oscillators that compose the GLAD model is Kramers-Kronig consistent. The actual equation describing the nth Gauss-Lorentz oscillator is as follows.

$$\begin{aligned} \epsilon_n(E) &= iA_n \left[\int_0^{\infty} e^{i(E-E_n+i\gamma_n(s))s} ds - \int_0^{\infty} e^{i(E+E_n+i\gamma_n(s))s} ds \right] \\ \gamma_n(s) &= \Gamma_n + 2\sigma_n^2 s \end{aligned} \tag{3.32}$$

Where A_n , Γ_n , σ_n and E_n are the basic variables being fit for each oscillator. These are recombined to form the variables which the software uses, allowing it to determine the locations of the peaks and asymmetry of the system with further variable input [22]. This model allows for a great deal of tweaking, due to the large number of variables, which is likely the reason it was initially chosen. However, the large number of adjustable

parameters causes most fits to behave very abnormally, generating a completely unrealistic series of optical constants.

3.4 Fitting the Model to the Data

In theory, fitting the model parameters to experimental data should be as straightforward as accurately describing the system via the model and allowing the process to iteratively reduce the MSE to the minimum value. However, this is not always the case. The program must be carefully guided through a series of crucial steps to avoid generating data for an unrealistic model. If steps are not taken to ensure the accuracy of the generated data, there is a strong probability that the generated data will be neither unique nor realistic. In developing a comprehensive, robust modeling process, many different approaches were used. Different fitting methods were used in different orders, as well as much trial and error involving the choice of oscillator models used.

Furthermore, the process of data fitting became rapidly more complex as the samples became more complex due in part to amorphous-crystalline state blending and grading of the materials. Initially, the low temperature, amorphous CTO samples were fairly straightforward to fit. As the deposition temperature was increased, the process of fitting this data became more difficult, as the chemistry and structure of the CTO, and thus the optical properties, changed. The material layers became less uniform as the physical properties changed. This increasing difficulty also manifested when heat treatments were introduced to the samples. Ultimately, what was required was a

reevaluation of the 'ideal material' as assumed by the software.

The 'ideal material' assumptions made by the software can lead to problems when modeling. Because the model data is being varied in order to fit it to the experimental data, if a parameter is unaccounted for or misrepresented, the best fit result may not reflect on the actual physical properties of a sample [22]. By default, the software makes many assumptions about the nature of the sample. These assumptions need to be considered and often explicitly overwritten in order to accurately model the data. Some of these assumptions are:

1. The light entering the detector is perfectly polarized.
2. All interfaces between layers are abrupt and perfectly flat.
3. All films and the substrate are uniform along the direction normal to the sample surface.
4. All films and the substrate are isotropic.
5. All optical constants that are held fixed exactly describe the corresponding material in the sample [22].

These assumptions are just a few of many that can dramatically alter the data analysis process. Most of these issues are easily corrected for, but the primary problem with most data fitting is that they are not considered. All issues reflecting on the 'non-ideal' nature of the samples -excluding the discussion of isotropy and polarization, which were discussed in section 3.2.5- are addressed in the following discussions of the optical models.

3.4.1 Initial Model

The general procedure used for initially fitting samples starts with the model. The model should be built following the previously mentioned model structure. The layer thickness should be estimated from knowledge of the deposition conditions, or measured with the Dektak, if possible. If possible, AFM data can be used to establish a rough estimate for surface roughness of the samples. The initial model for the CTO layer should always start with the TL oscillator fitted to a preexisting model for CTO. This reference model allows the fitting process to start from a data set that should be approximately the same as the data in question. The data type of both experimental and generated data should be changed from 'ellipsometry' to 'ellipsometry with backside reflections', since the samples are all on smooth glass. In addition, the number of backside reflections should be allowed to fit. Selecting parameters 'to fit' changes the values from 'fixed' to a variable parameter that will be iteratively minimized during the next fit run. This terminology will be used from now on.

For this model, pole position 1 should be allowed to fit as well as the magnitudes of pole position 1 and 2. The poles mentioned are two zero-width oscillators, one at high energy, one at low energy. These oscillators, in addition to the 'e1 offset' are used to account for absorption outside the range of available ϵ_2 values [22]. The reasoning for these pole fit options being selected is purely empirical. All of these parameters are shown in an example oscillator layer window in Figure (3.3). All of the oscillator parameters should be allowed to fit as well. At the main screen all thicknesses should be

allowed to fit as well. The initial fit benefits from a 'wide open' approach of fitting all of the variables simultaneously. This method allows for a better understanding of the trends of the various parameters, allowing for a more educated approach to fine tuning the model.

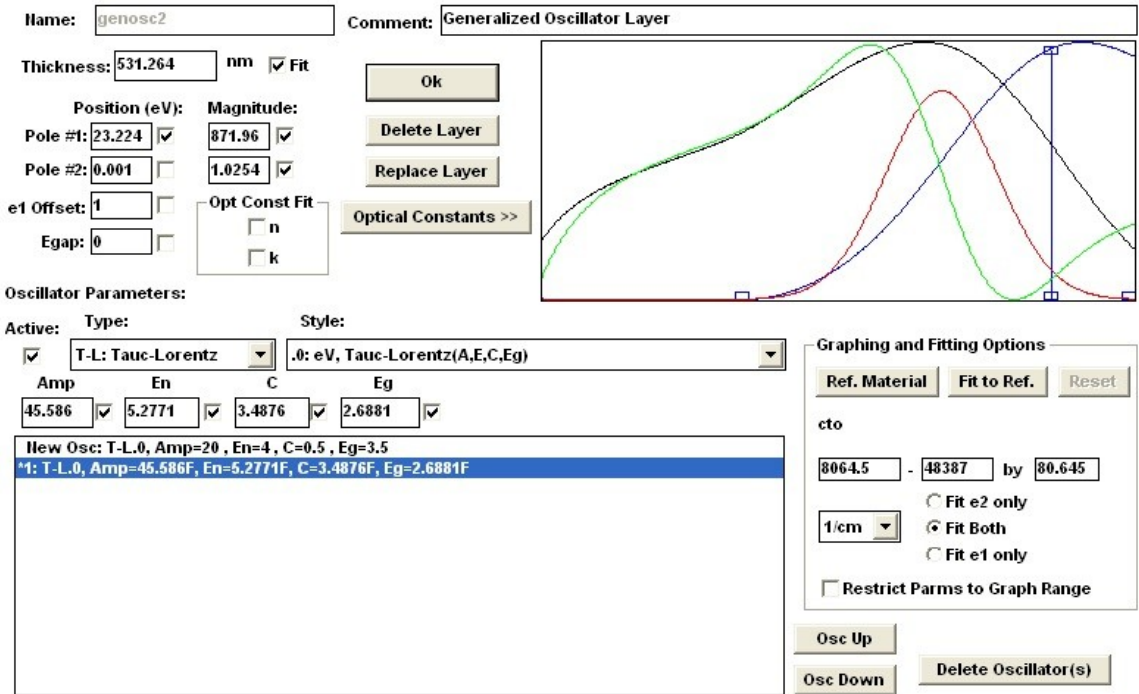


Figure 3.3: The general oscillator layer window from the WVASE32 software after fitting a TL oscillator to sample SP3128.7. The blue curve is the actual oscillator being fit to ϵ_2 . The black curve is the Kramers-Kronig calculated fit for ϵ_1 . The red and green curves are ϵ_2 and ϵ_1 for the reference oscillator, respectively.

Next, a test fit should be run. The 'normal fit' option should be selected to engage the Levenberg-Marquardt algorithm. The default parameters of the fit iterations are sufficient, however the number of iterations before automatic shutoff is fairly small by

default, at 29. Typically, fits were allowed to run for many iterations beyond this limit, in order to more accurately fine tune the MSE values. If time is not a question, having a fit turn off due to reaching its minimum bound for MSE improvement is vastly preferred over having a fit turn off due to reaching an arbitrarily set limit of iterations. However, if a fit does not settle and stop after very many iterations, it is very likely not unique.

Once the fit has run, changes to the model thickness, the graph displaying Ψ , and the MSE should be observed. Viewing the graph for depolarization might also add some insight. Ideally, an MSE lower than 10 is in an acceptable range. Obviously, lower is better. Thicknesses should behave reasonably, and neither blow up, or reduce to zero. Viewing the graphs is very helpful when forming judgments about the model. They allow for a quick view of just how accurate a specific model may or may not be. Generated data should be checked to see how closely it matches the experimental data. Perhaps there is an energy range that more accurately matches the data than the rest of the model. Such quick observations allow a better appraisal of how to proceed. After many fits, an 'intuition' is developed, allowing the user to better understand the quality of the fit. For example, whether the material layer needs to be thicker or thinner can usually be judged with a reasonable degree of accuracy by looking at the frequency of the oscillations of Ψ over a certain range of the graph. Typically, the higher the frequency of oscillations over a given energy range, the thicker the material layer is. Comparing the generated and experimental oscillations allows for a quick judgment call on the accuracy of the given thickness.

Unless the fit is very good (~ 1 MSE) after this first attempt, the variables for the oscillator and thicknesses should be reset back to matching the original model. The starting thickness should be varied and refit. It is usually most helpful to vary the CTO thickness in 50 nm increments. When a rough idea of the behavior over a range of thicknesses is determined, start fitting with smaller differences, down to about 10 nm between each attempt. This process will help to isolate the extreme minimum in the MSE curve. More likely than not, once the thickness of the material layer is close to the actual thickness, the fit will tend to migrate to that value. It should be noted that this behavior happens for local minima as well, so it is important to compare several different regions and to step the thickness across a wide range of values in order to determine which gives the best results. Once the approximate thickness is fit, thicknesses can be locked, by disabling the thickness as a fit parameter. Very rarely is the initial thickness guess close enough to the actual thickness for it to migrate to the extreme minimum.

Once the thickness of the material layer is well determined, another fit can be run. This time, All thicknesses should be fixed, but all parameters from the oscillator should be left to be fit. Backside reflections should also still be set to fit. Once the fit is run, if the MSE is good (< 10) Further steps at refinement can be taken, such as exploring grading options. The last independent fit should be the thickness of the surface roughness layer.

If the MSE is not good, or the generated data on the Ψ graph does not accurately match the experimental data, all fit parameters should be fixed, and the optical constants of the material layer should be allowed to fit. The fit type should be a point by point fit, as this will judge each energy value independently. The goal of this fit is to see what optical constants are required to accurately match the data. Once these optical constants are generated, they need to be considered. If they are smoothly varying, outside of statistical noise, and behave realistically -they should be zero or close to it for much of the energy range, for values of k - Then they should be saved, and the entire process of fitting should be repeated, using these values for the optical constants as the reference model.

If the generated optical constants are not good, such as behaving unrealistically or not smoothly varying, then they should be discarded. A recurring problem at this stage is sawtooth-like waveform appearing in the optical constants. This is obviously unrealistic and should be discarded.

If the above method is unable to bring the MSE down below 10, the non-ideal model option 'non-uniform thickness' should be attempted in the fit. Care must be taken in using this option. Acceptable values for this parameter are typically no greater than 10%. On occasion this value will climb wildly out of control, up to 80% or higher. These results are inaccurate and must be ignored. In addition to this, a simple grading layer should be added to the CTO layer, and all variables of this layer should be allowed to fit.

A grading perturbs the optical constants of the layer in question by some function of thickness. They are very useful in modeling non-uniform samples. More will be said about grading layers later. If it is still impossible to bring the MSE below 10, all above steps should be repeated using the GLAD model instead of the TL model. On the rare occasion, this has yielded better results than the TL model.

Once a model is established to a high degree of accuracy, attempts to probe it for uniqueness should be made. Various variables should be forced far from the final values of the best fit and refit, with all parameters set to fit. Ideally, the values of the perturbed parameters will always return to the same value. The program has a built in feature to do just this, allowing the analyst to select the parameter to test for uniqueness and inputting a range of values for the parameter in question. This feature will run the data, locking the parameter in question at each of the specified values and running a normal fit on the model for all parameters allowed to be fit. Ultimately, this will generate a graph of MSE versus the new parameter value, allowing easy viewing of exactly how the MSE changed from the perturbation. An example is seen in Figure (3.4). This feature works especially well for single-valued parameters, such as thickness. Since this feature is only able to test one parameter at a time, using it for aspects of the oscillator model, or the optical constants themselves, seems very inefficient. These are best perturbed manually.

It should be noted that during the various fits, the backside reflection may become 'stuck' at either the max or min values, which are 0 and 5, respectively. If this happens,

the value should be forced to something in between. If after several fits this is still the case, then the model is unable to accurately describe the number of backside reflections, and it should be ignored, or set to some value. On occasion, fitting the '% of first reflection collected' option will correct this problem, but often at the cost of collecting greater than 100% of the first reflection. This issue with the backside reflections currently has no resolution.

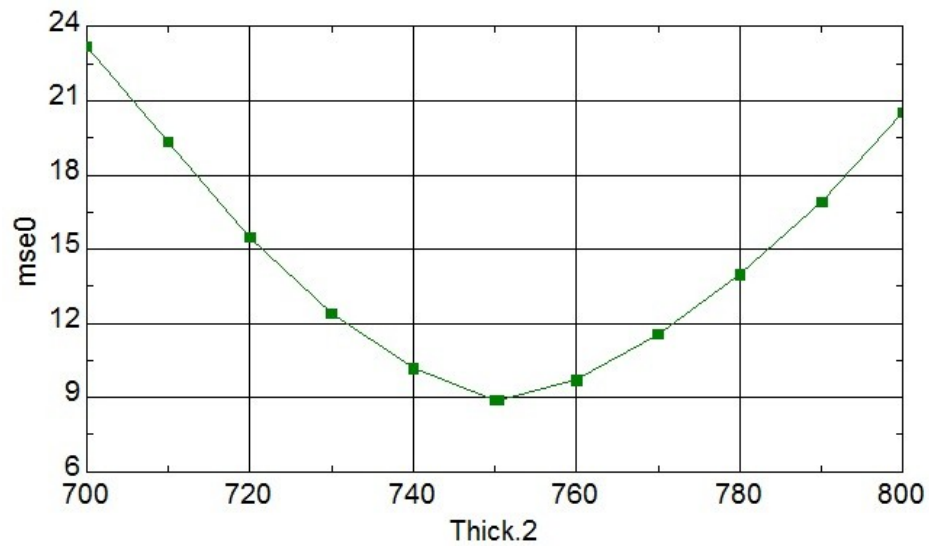


Figure 3.4: Graph of MSE (mse0) vs. CTO thickness (Thick.2) for sample SP3118.7ht. This MSE is unique at 750 nm.

3.4.2 Final Model

The above formula for data modeling works reasonably well, especially for amorphous samples deposited at lower temperatures. However, it is still fairly limited when attempting to model samples that have begun to crystallize. These partially

crystallized samples fall out of the constraints of the 'ideal model'. The process routinely fails at accurately capturing the optical constants for samples that deviate from this simple form. As samples gradually became more and more complex, this inability to adapt led to the need for a secondary modeling formula. With the assistance of James Hilfiker, an engineer at J. A. Woollam, a new data modeling formula was developed.

The first step, as before, involves accurately modeling the substrate. This step is identical to the previous method. Glass substrates are 1.5 mm thick. The appropriate glass model should be used, and the data should be set to 'backside reflections' as before. Similar to before, an initial oscillator model is built. However, instead of building the initial model based on a reference from a previous CTO data set, the new modeling procedure calls for an attempt at building the reference from the ground up. This process obviously takes more time than simply basing each model off of a predetermined reference. However, the time spent building a custom reference for each sample ensures that each sample is self consistent. If one set of optical constants varies greatly from the rest, this process will ensure that those differences are accurately captured.

In order to build this reference layer, the Cauchy dispersion relationship is used. This dispersion relationship was developed by Cauchy upon observing that, for most transparent material in the visible range of wavelengths, the index of refraction decreased with increasing wavelength. This relationship can be expressed approximately as

$$n(\lambda) = n_0 + \frac{n_1}{\lambda^2} + \frac{n_2}{\lambda^4} \quad (3.33)$$

where n_0 gives the constant value at long wavelengths, n_1 controls the curvature in the middle of the visible spectrum and n_2 influences the short wavelength range of the spectrum [20]. The Cauchy dispersion relationship is often used empirically to fit the above described transparent materials. Since the Cauchy relationship only describes the index of refraction, a different relationship is used to model the extinction coefficient.

$$k(E) = A_k e^{B_k(E-E_b)} \quad (3.34)$$

Here, A_k , B_k and E_b are all variables that define the function [20]. This relationship, the Urbach relationship, is suited for modeling the absorption tail of the extinction coefficient [22]. It is important to note that these two functions are independent of each other and must be fitted separately.

In order for the Cauchy relationship to accurately capture the relevant sections of the coefficient curves, the overall data should be narrowed down. This initial fit should be done between 1.3 and 2.9 eV. This range roughly captures the gradual increase in the index of refraction with increasing energy. At the same time, it should be noted this same region has a zero value for the extinction, since the material is transparent in this range of energies. In order to accurately capture these points, the first two coefficients of the Cauchy relationship should be fit and the Urbach relationship should not be fit, but instead be left as a zero value. Fitting the third Cauchy coefficient is not required and may actually warp the shape of the curve, in attempting to exactly match the data from

this energy range. As usual, the number of backside reflections should be set to fit for this data run. The thickness of the Cauchy layer should be estimated based on deposition conditions or Dektak data and also be allowed to fit.

Once a normal fit has been run, consistency with the actual data should be checked using the techniques from the first modeling formula. If the fit is good, the optical constants should be saved. If the data is not good, the range of energies may need to be adjusted to more accurately capture the desired Cauchy-like behavior. If no fits capture this well, the data may not lend itself to a Cauchy relationship and the old method of using reference data from past samples should be used. The previously mentioned technique of attempting fits at various thicknesses should be applied to this fit attempt as well, in order to pinpoint the approximate thickness values. The thickness should migrate to the minimum values when the initial conditions are close, as discussed.

Once a reference layer is established, a model is ready to be built. A Gaussian oscillator should be used. The Gaussian oscillator is far more versatile than the TL oscillator, which should allow for more accurate fits as the samples grow in complexity. Once the oscillator is fit to the reference, all parameters describing the oscillator should be allowed to fit. In addition, pole position 1 should be fit, as well as the magnitudes for both poles. Thickness should be estimated based on the results of the Cauchy fit and allowed to fit. It is important to note that the model does not include a surface roughness layer at this point. Backside reflection should still be allowed to fit. This initial fit attempt

should be run at the previously selected narrow range of energies. Once these options are selected, a normal fit should be run. Once again, attempting different thicknesses will yield the best results.

When a good fit is established, the restrictions on the energy range should start to be loosened. Gradually, the range should be expanded, with more weight on expansion into the lower energy region. Each time the range is increased, a new normal fit should be run. Each fit may involve readjustment to test the thicknesses. In extreme cases, resetting of the oscillator parameters back to the initial model may be required if the oscillator model migrates too far to be further fitted accurately. During this process it may also be useful to fit the e_1 offset values, in order to give a greater degree of variability. Detail should be paid to the behavior of the oscillator model parameters, and ultimately it is up to the discretion of the analyst which of the above mentioned parameters should be allowed to fit. Typically, the pole position will settle on a region and may be disabled. Similarly, the magnitude of either pole may drop to zero, clearly indicating it is not relevant in the current fit, and thus may be disabled. The value of the backside reflection should also be continuously checked to ensure it has not become fixed at one of the extreme values.

Ultimately, at the end of this process the full range of energies of the initial data should be allowed to fit. Once the best possible fit has been achieved, data values can be fixed and perturbed as described in the first model to ensure the uniqueness of the fit. At

this point, the model should be saved and all parameters should be fixed. The n and k values should be allowed to fit and a point by point fit should be run over the whole range of energy values. The results of this fit should be studied carefully and compared with the previous values of the optical constants, as well as the previous iteration of the Ψ graph. This comparison may reveal details about how the model is lacking. All steps above should be repeated using the n and k values from the point by point fit as the basis for the reference model. The final results of this new fit should yield a lower value for the MSE. If not, it is advised to revert back to the previous model.

At this stage, it may be necessary to add a grading layer. It is not uncommon for transparent conductive oxides to require a parametric grading layer to accurately describe the nuances of the physical stack. This will be discussed momentarily. At this time it is also acceptable to run a final fit with the surface roughness layer added [27].

This modeling formula has proven to be more robust than the initially developed formula, being more naturally fitted to nearly all of the later stage samples, whose complexity eluded the TL oscillator based initial model. Several of the runs accurately fitted using the TL model were refitted using the newer Gaussian model as a method of comparison. The results of this comparison showed a significant amount of agreement from the major parameters such as thickness and the optical constants. MSE values were also comparable. This consistency between different models is very reassuring, as well as testament to the accuracy of these described formulas.

3.4.3 Gradings

Several times in the modeling processes, gradings have been mentioned as a means to further reduce the MSE near the end of a fit. The idea of a grading warrants an entirely separate discussion. Gradings can be either a very powerful tool to further recreate nuances of physical data, or 'filler' material with no grounding in reality, reducing MSE values simply by bending data to 'fill in the cracks'. They must be employed judiciously and with a fair amount of supporting analysis.

There are two primary types of grading that were used to model this data. Simple index grading and parametric grading. The software is capable of many different types of grading, however these two are the only types relevant to this discussion of modeling. Simple index gradings follow a basic structure, allowing for a degree of variation off of the average index from the sample being graded to be adjusted and fitted via the “% Variation Range' box. They also allow for variations from the default linear grade with the addition of a fittable exponent, which varies the grading according to the value of the exponent. This can be further adjusted by the use of a symmetric grading profile toggle which, when toggled, will force the grading to behave symmetrically in the material. It is of value to note that the average index is effectively independent from the details of the grade profile. This will prevent the shape of the actual generated Ψ and Δ data from changing, allowing the average index values to remain unchanged by the variation of the grading [22]. An example of a simple index grading is shown in Figure (3.5).

The second type of grading used is far more complex. This grading allows for each parameter in a given model to be graded through the film's thickness independently. This fit also allows for various nodes to be set through the grading thickness. These nodes allow for several segments of linear grading to be combined through the thickness, as a piecewise function. This grading method is incredibly effective at reducing the MSE of a given sample, but should be taken with a grain of salt, due to the vast quantity of fit parameters. It is very possible that this grading can produce non-unique results. An example of a standard parametric grading is shown in Figure (3.6).

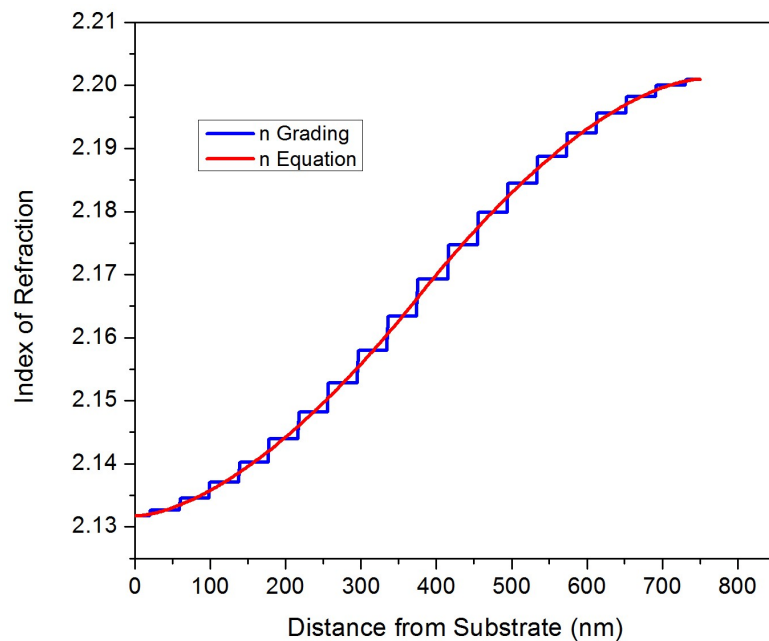


Figure 3.5: An example of simple index grading for sample SP3118.7ht using data at 500 nm wavelength. This grading has a variation range of 3.2%. It also has a symmetric exponent of 1.6. The extinction coefficient is not present. Due to the nature of the grading, the grading for each constant is identical over their respective ranges.

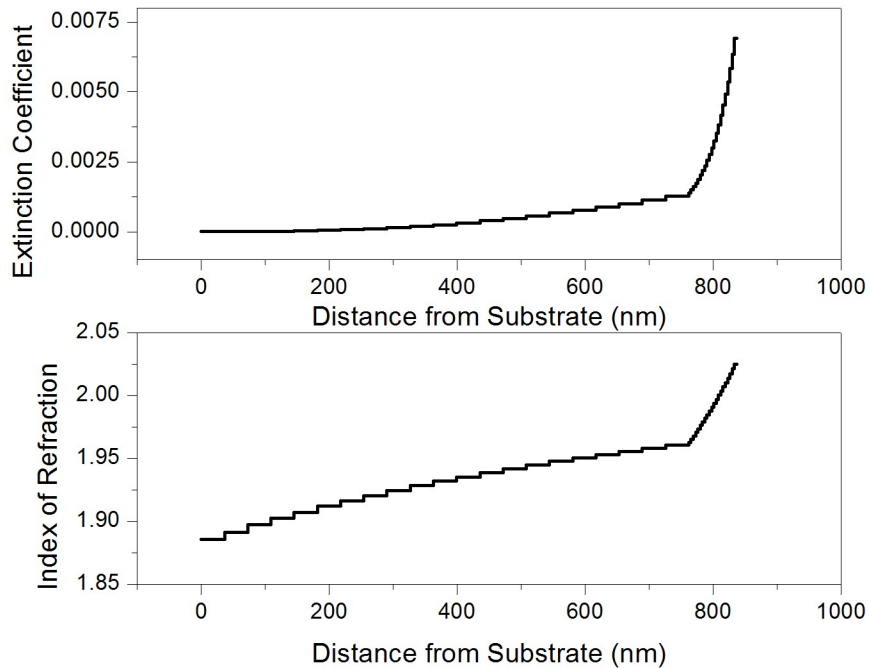


Figure 3.6: An example of a grading for SP3151.2a using data at 500 nm wavelength. Here, the left axis is associated with n and the right axis is associated with k . Note the node at approximately 770 nm.

Physically, TCOs such as CTO are very complex systems. In general, it is unlikely that a good fit will be achieved without a grading, due to the physical acts of depositing and annealing such a film and the changes these cause throughout the film. The heat treatments in particular involve extreme heat and environments. These extreme conditions can result in interdiffused interfaces between layers. Further, surface layers may lose or gain new components such as oxygen. Recrystallization at one or more surfaces is also possible under these conditions. A grading is able to reasonably simulate the changes in optical properties of a material as a function of depth, allowing for far more accurate models to be developed. It is a common problem among researchers of

TCOs to ignore the grading of a film and achieve poor fits to the experimental data, claiming these accurately represent the physical characteristics [22].

Having said this, accurately representing a grading is nearly impossible, and only an approximation of the true physical grading may actually be achieved. It should be noted that due to the approximate nature of the grading and the complex nature of TCOs in general, including surface roughness often helps reduce the MSE of a given fit. It is uncertain if this is due to actual, physical roughness, or if the additional parameter helps to compensate for the approximate nature of the model. Use of the AFM may allow further understanding of this surface roughness.

Gradings should always be made as simply as possible, working towards a more complex system. They should also only be introduced to a model after the best possible fit for the model without the grading has been achieved. It should be noted that once a grading layer is added to the model, the thickness for the grading layer replaces the thickness for the layer being graded. In this way the grading layer is used as a template to modify the material layer. In the case of the simple index grade, this is relatively straightforward. The grading parameters can be fit and once a good fit is achieved, the number of sublayers can be increased to provide a smoother variation. The process is a bit more complex for the standard parametric grading, however.

When building a parametric grading, care must be taken to avoid correlations between various parameters. These will lead to unrealistic grading results. The primary parameters to be graded during a parametric grading are the oscillator parameters and the pole magnitude parameters. Initially, it may be wise to allow all of these to be graded, before any further steps should be taken. Two endpoint nodes should be enabled at 0% and 100%. The percentage indicates the percent of the way through the material the node is, with 0% being at the substrate. The values at both of these nodes should be allowed to fit. It may or may not prove useful to run this initial test with various parameters enabled to be fitted.

Once an initial normal fit has been run for the grading, the grading should be checked for correlations between the variables. The software used has a built in feature that calculates a correlation matrix for all fitted parameters. If there is strong correlation between two variables, one or both should be disabled. At least one of them is most likely not capable of being accurately fitted. If the grading values at 0% and 100% are very different, then a third node should be added at 50% thickness, and allowed to fit both the location and the value. Using more than three nodes is unwise, as strong correlations begin to form.

Once a normal fit has been run for this data and correlations checked, the analyst should judge how realistic the grading is. If the grading is unrealistic, the model is probably too complex. A node or a parameter being graded most likely should be

removed, due to correlations. At this stage of the fitting, a good guideline is impossible to describe, due to the ever changing nature of the fitting process. Ultimately, fits should be rerun with various parameters enabled until a fit with a low MSE and minimum correlation is obtained. Once a good fit for the grading is obtained, the slices per node may benefit from an increase. This will refine the grading, perhaps increasing the MSE.

Chapter 4

EXPERIMENTAL

CTO films were deposited under a wide range of predetermined parameters using conventional RF sputtering techniques. In addition, many samples were further annealed in various atmospheres and at different temperatures. Physical details of these processes relevant to the characterization of these samples will be discussed briefly. Further, in addition to ellipsometry, several other optical and non-optical characterization methods were used. These methods will be described to the degree that they are relevant to characterizing these materials.

4.1 Deposition

Deposition for all CTO samples was carried out by Dr. Tiejun Meng, a research fellow at the Institute of Energy Conversion. The system used to deposit these samples was the Institute of Energy Conversion's sputtering system number three (SP3). This system is a RF/DC sputtering system which is able to co-sputter from up to 6 cathodes onto a single 4 inch target. For this work, only a single cathode was required. The remaining cathodes were shielded from contamination by a specially built shield. The system has four separate gas lines, allowing for the creation of unique ambient atmospheres. These lines include a pure argon line, an argon/oxygen mix, an

argon/hydrogen mix, and a water vapor line. The system is able to achieve a vacuum on the order of 10^{-7} Torr. The system also has a heater allowing for a substrate temperature in excess of 500 °C.

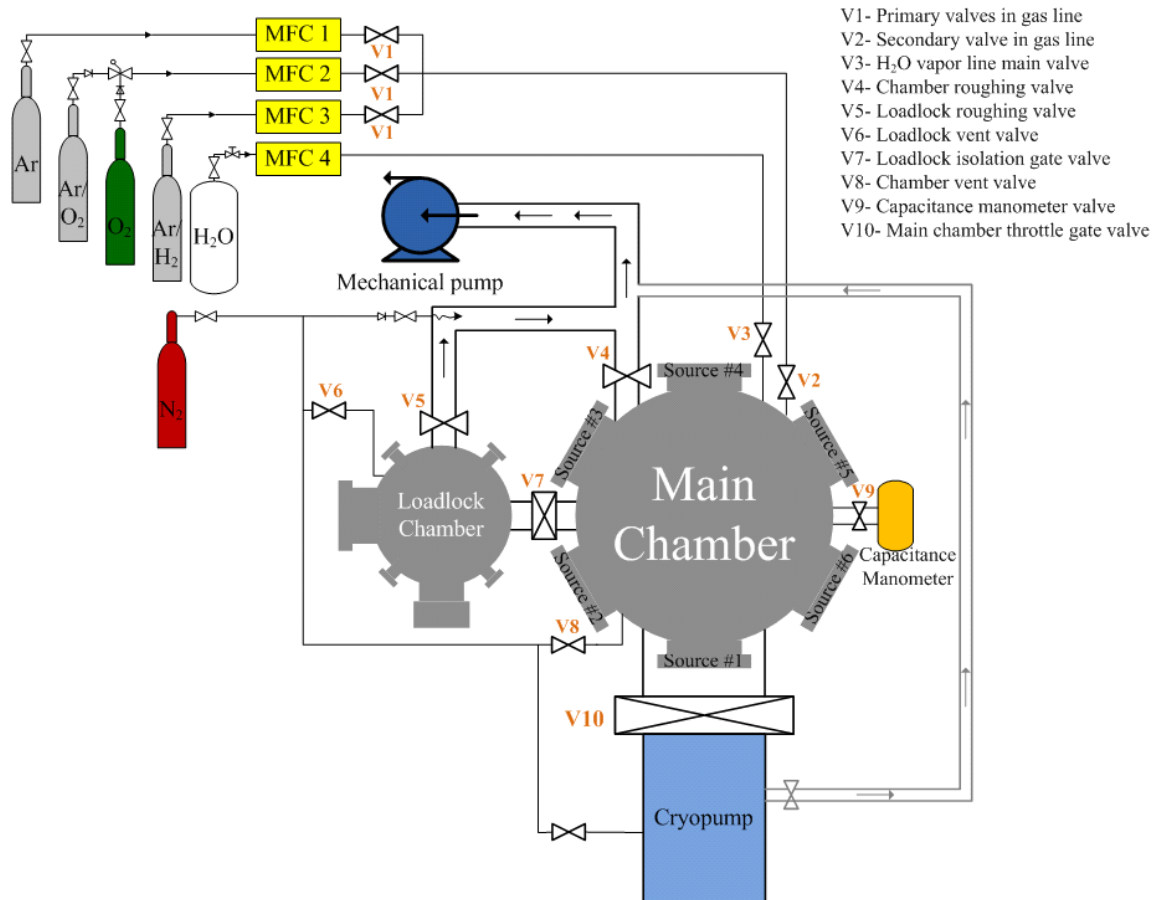


Figure 4.1: A diagram of the SP3 sputtering system. Image provided by Tiejun Meng.

The setup of SP3 allows for a great deal of control in the deposition parameters. Pressure, ambient gas composition, substrate temperature, RF power and substrate-target distance are all variable parameters of deposition. For the CTO films, a fixed RF power

of 100 W was used. The target-substrate distance was also fixed at approximately 2 inches. The CTO samples were deposited through different combinations of: ambient pressure, which was varied from 5-15 mTorr, 2) substrate temperature, which was varied from 25-500 °C and 3) oxygen content, which was varied from 0 to 5% in an argon atmosphere.

Table 4.1: Deposition conditions for CTO samples 112-151.

Sample ID	Run Date	Substrate	Pressure (mT)	RF Power (W)	Oxygen (%)	Substrate Temp (C)	Pre-sputter Time (min)	Deposition Time (min)	Center Thickness (micron)
SP3112	8/10/2010	SLG	5	100	1	25	60	30	0.78
SP3113	8/11/2010	SLG	5	100	5	25	30	30	0.80
SP3114	8/12/2010	SLG	5	100	0	25	30	30	0.73
SP3115	8/13/2010	SLG	5	100	2	25	30	30	0.76
SP3116	8/16/2010	SLG	5	100	1	300	30	30	0.63
SP3117	8/17/2010	SLG	10	100	1	300	30	30	0.73
SP3118	8/18/2010	065-4033	15	100	1	300	30	30	0.8
SP3119	8/19/2010	065-4032	10	100	1	400	30	30	0.57
SP3120	8/24/2010	065-4031	10	100	1	500	30	5	0.12
SP3121	8/26/2010	065-4030	15	100	1	400	30	30	0.67
SP3122	8/27/2010	065-4029	5	100	1	400	30	30	0.25
SP3123	8/31/2010	065-4028	15	100	0	300	60	30	0.64
SP3124	9/1/2010	065-4027	10	100	0	300	30	30	0.68
SP3125	9/2/2010	065-4026	10	100	0.3	300	30	30	0.71
SP3126	9/9/2010	065-4025	10	100	0.6	300	30	30	0.74
SP3127	9/10/2010	065-4024	10	100	2	300	30	30	1.02
SP3128	9/16/2010	065-4023	10	100	0	400	30	30	0.65
SP3129	9/17/2010	065-4022	10	100	5	300	30	30	0.9
SP3140	10/14/2010	065-4021	20	100	50	25	30	30	0.4
SP3144	10/18/2010	065-4020	10	100	50	25	30	30	0.34
SP3145	10/19/2010	065-4019	10	100	20	25	30	30	0.51
SP3146	10/20/2010	065-4018	10	100	10	25	30	30	0.66
SP3147	10/21/2010	065-4017	10	100	5	25	30	30	0.76
SP3148	10/22/2010	065-4016	10	100	10	25	30	20	0.43
SP3149	10/25/2010	065-4015	10	100	10	25	30	10	0.24
SP3150	10/26/2010	065-12900	10	100	10	25	30	5	0.1
SP3151	10/27/2010	065-12901	5	100	5	25	30	30	0.82

Deposition time was another variable involved in the creation of these samples. Typically, samples remained in the chamber for 30 minutes before deposition and then were deposited for 30 minutes. However, other time spans were used for a few samples. Table (4.1) has the full range of deposition conditions and the resulting approximate film thicknesses.

4.2 Heat Treatment

After initial characterization, many samples were further annealed under various conditions in order to crystallize samples and adjust film properties. It has been shown that such heat treatments can dramatically improve the optical and electrical properties of CTO [28] [29]. These samples were annealed in a quartz tube placed in an oven. Typically, these samples were placed in the tube and flushed with argon for about 15 minutes before being placed in the oven where they were annealed from 500-700 °C for 30 minutes. The environments of these heat treatments varied greatly, most commonly involving argon, hydrogen and air.

As per the method outlined first by Haacke et al. and later by Wu et al. [28] [29], samples were annealed in direct contact with a thin film of CdS deposited on a separate glass substrate. According to Wu, during the heat treatment CdS vapor is sublimated from the CdS layer and diffuses into the CTO crystal lattice. This diffusion of CdS creates interstitial cadmium and oxygen vacancies and reduces the quantity of secondary phases, such as CdO, SnO₂ and CdSnO₃, in the CTO [29]. The presence of these secondary

phases are known to adversely impact the electrical properties of the CTO layer [30] [28].

Samples SP3112-SP3140 were annealed using CdS created by physical vapor deposition (PVD), more specifically, thermal evaporation deposition. Samples SP3146-SP3151 were annealed using CdS created by chemical bath deposition (CBD). All CdS samples were on the order of 100-150 nm thick and were deposited on ~1 mm thick Corning 7050 glass. Many CTO samples were also annealed without the CdS sample, as a method of comparison. Table (4.2) lists the full array of heat treatments used.

Table 4.2: Heat treatment conditions for CTO samples 112-151.

Sample ID	Sample Cut	Temp. (C)	Environment	CdS ID
SP3112	3112-7	550	Ar	-
SP3113	3113-2A	550	Ar	-
	3113-3A	450	Ar/CdS	12420-13
	3113-2B	500	Ar/CdS	12420-21
	3113-3B	550	Ar/CdS	12420-12
	3113-7A	600	Ar/CdS with Mica	12423-13
	3113-8A	550	Ar/4% H2	-
	3113-7B	600	Ar/4% H2	-
	3113-4B	550	Ar+10 mg Sulfur	-
	3113-5A	550	Ar	-
	3113-4A	550	Ar+2 mg Sulfur	-
	3113-5B	550	Ar	-
	3113-8B	550	Ar+5 mg Cd	-
	3113-1A	550	Ar+5 mg Cd	-
SP3118	3118-7	600	Ar	-
SP3119	3119-7	600	Ar	-
	3119-3A	420	Air	-
	3119-3B	420	Air/CdCl2	-
	3119-6A	600	Ar/CdS	12423-32
SP3124	3124-1A	600	Ar	-
	3124-6B	700	Ar	-
	3124-2A	550	Ar/CdS	12419-12
	3124-3B	600	Ar/CdS	12421-11
	3124-7B	650	Ar/CdS	12421-12
	3124-7A	700	Ar/CdS	12420-33
	3124-8A	550	Ar/4% H2	-
	3124-5A	600	Ar/4% H2	-
SP3129	3129-1A	600	Ar	-
	3129-4B	700	Ar	-
	3129-3A	550	Ar/CdS	12419-21
	3129-2B	600	Ar/CdS with Mica	12421-32
	3129-3B	600	Ar/CdS	12423-21
	3129-7B	650	Ar/CdS	12423-21
	3129-7A	700	Ar/CdS	12423-23
	3129-8A	550	Ar/4% H2	-
	3129-5A	600	Ar/4% H2	-

Sample ID	Sample Cut	Temp. (C)	Environment	CdS ID
SP3140	3140-1A	600	Ar	-
	3140-6B	700	Ar	-
	3140-2A	550	Ar/CdS	12419-11
	3140-2B	600	Ar/CdS	12421-23
	3140-3A	650	Ar/CdS	12421-33
	3140-3B	650	Ar/CdS	12423-12
	3140-8A	550	Ar/4% H2	-
	3140-5A	600	Ar/4% H2	-
SP3144	3144-1A	600	Ar	-
	3144-1B	700	Ar	-
SP3146	3146-1B	700	Ar	-
	3146-2B	600	Ar/CBD CdS	13
	3146-3B	700	Ar/CBD CdS	9
SP3148	3148-1A	600	Ar	-
	3148-1B	700	Ar	-
	3148-2B	600	Ar/CBD CdS	14
	3148-3B	700	Ar/CBD CdS	10
SP3149	3149-1A	600	Ar	-
	3149-1B	700	Ar	-
	3149-2B	600	Ar/CBD CdS	15
	3149-3B	700	Ar/CBD CdS	11
SP3150	3150-1A	600	Ar	-
	3150-1B	700	Ar	-
	3150-2B	600	Ar/CBD CdS	16
	3150-3B	700	Ar/CBD CdS	12
SP3151	3151-1A	600	Ar	-
	3151-5A	700	Ar	-
	3151-1B	600	Ar/4 mg SnS	-
	3151-2A	600	Ar/CBD CdS	2
	3151-3A	600	Ar/CdS	12422-32
	3151-2B	650	Ar/CBD CdS	3
	3151-3B	700	Ar/CBD CdS	8
	3151-4A	600	N2/CBD CdS	7
	3151-4B	600	Air/CBD CdS	1

4.3 Characterization and Analysis

Many methods of characterization were used in ultimately determining the various properties of the CTO material samples both before and after heat treatments. Several of these techniques were also used to confirm results provided by the ellipsometer and to give insight into the structure of the samples which allowed for a more accurate and unique model to be developed.

4.3.1 Ellipsometry

Measurements taken by the ellipsometer, as described in chapter 3, were the primary source of data regarding the optical properties of CTO films. The extinction coefficient in particular was important to the work done regarding CTO. Once an accurate extinction spectrum is obtained, this data can be used to determine the absorption spectrum, the transmittance of the material and information about the band gap. In addition, the refractive index will be used to refine the anti-reflection properties of the entire window layer stack in the complete solar cells.

The absorption spectrum is easily determined from extinction. The relationship between the two is defined as

$$\alpha = \frac{4\pi k}{\lambda} \quad (4.1)$$

where k and α are functions of λ . Further, it is known that the absorption coefficient α is related to transmittance in a uniformly absorbing medium via the Beer-Lambert law.

$$T = e^{-\alpha t} \quad (4.2)$$

where T is the transmittance and t is the thickness of the material through which light is traveling. Here, T and α are single-valued. For non-uniformly absorbing media, α and T gain wavelength dependency, allowing for easy combination with equation (4.1). Thus, equation (4.2) can be rewritten as

$$T(\lambda) = e^{\frac{-4\pi t k(\lambda)}{\lambda}} \quad (4.3)$$

which allows for easy and quick calculation of the transmittance with respect to wavelength. These values can be compared to data obtained by the spectrophotometer to check for accuracy.

In addition, the absorption spectrum determined from equation (4.1) can be used to calculate the approximate value for the band gap of each sample. Depending on the band gap structure, the energy dependence of α can be determined from one of two equations.

For indirect band gap semiconductors as well as most amorphous semiconductors [31], α is given by

$$\alpha(E)_{ind} = A \frac{(E - E_G)^2}{E} \quad (4.4)$$

where A is a constant, E_G is the optical band gap energy and E is the energy corresponding to the absorption [32] [33]. In the case of indirect band gap semiconductors, E_G is equivalent to the energy of the photon required for an electron

transition, as well as the change in energy due to phonon emission or absorption, required to change the crystal momentum [32]. As mentioned earlier, equation (4.4) is also valid for amorphous materials due to the lack of translational symmetry, which relaxes the requirement for conservation of crystal momentum [33]. A plot of $(\alpha E)^{1/2}$ versus E should be linear across the region of high absorption, where α is typically greater than 10^4 cm^{-1} . Applying a linear fit to this region and extrapolating to $(\alpha E)^{1/2} = 0$ will give the value of the band gap [33].

For direct band gap semiconductors, α is given by

$$\alpha(E)_{dir} = B \frac{\sqrt{E - E_G}}{E} \quad (4.5)$$

where B is a constant [32]. A plot of $(\alpha E)^2$ versus E should be linear across the region of high absorption, allowing a linear fit to be made in the same fashion as mentioned above in order to determine the band gap. Here, E_G is purely the energy of the photon required for an electron transition, since no change in crystal momentum is needed.

A computer spreadsheet was implemented to calculate these values, allowing values of n and k determined by the ellipsometer to be quickly inserted, immediately generating a graph of normalized transmittance as well as graphs for α versus E, $(\alpha E)^{1/2}$ versus E and $(\alpha E)^2$ versus E. By studying each of these band gap models, it should be possible to determine the band gap structure of a given sample. This is typically done by comparing the linear absorbing region of each graph. Figure (4.2) shows a good example

of both indirect and direct band gap determination. Since these are both for the same sample, the fact that both models fit fairly well may suggest that there is a mixed band gap state in this sample. In this way, the band gap was able to be determined for any sample. Further cross-referencing these results with GIXRD data relevant to crystallization allowed for complete determination of the band gap structure. These values are only approximate, yet are still very useful in quantifying the development of the CTO samples. Figure (4.2) shows an example of this process for a partially crystallized sample. It is important to note that while the indirect model has a good linear fit, the sample itself exists in a mixture of crystal structure revealed by the GIXRD data, ultimately meaning that only a best guess for the band gap can be made.

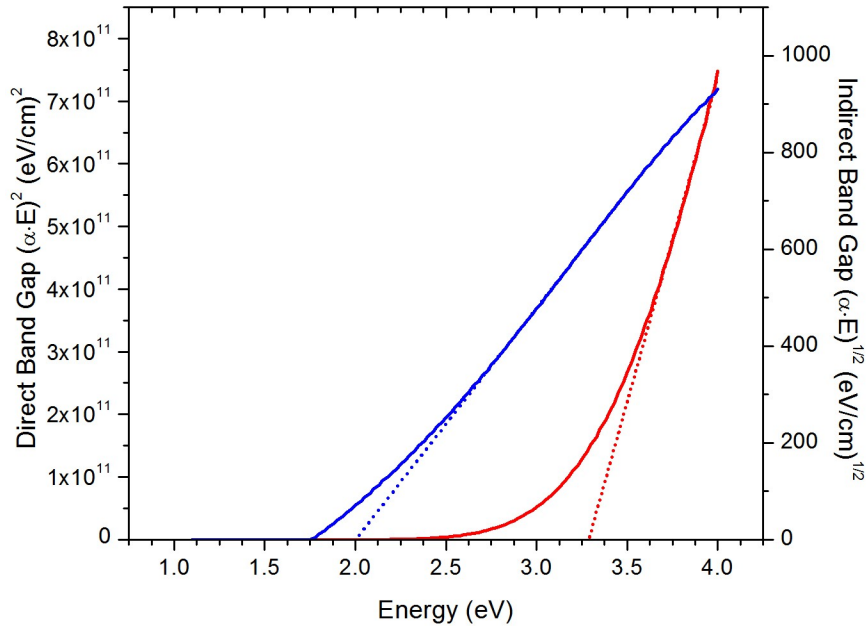


Figure 4.2: A comparison of direct (right line) and indirect (left line) band gap calculation for SP3151.7. The band gap of about 2 eV for the indirect is similar to known data regarding amorphous CTO [28] [33].

4.3.2 Spectrophotometer

A PerkinElmer Lambda 750 UV/VIS spectrophotometer was used to obtain reflection and transmission data for the CTO samples. Transmission and reflection data were taken over the wavelength range from 300 nm up to 2000 nm. This large range allowed for a better determination of the optical behavior of samples. The data obtained from these measurements allowed for the normalized transmittance

$$T_{Norm} = \frac{T}{1 - R} \quad (4.6)$$

to be calculated and plotted.

Transmittance data obtained by the spectrophotometer was primarily used to rapidly assess the transparency of the as-deposited and annealed CTO films. High transmittance is one of the key features of a good TCO layer. Quick determination of approximately how transparent each sample was allowed for judgment to be made regarding further analysis, as well as further deposition and heat treatment strategies. In addition, the normalized data for transmittance was also compared to the calculated transmittance obtained via ellipsometry for the CTO layer to check for consistency. An example of this comparison can be seen in Figure (4.3).

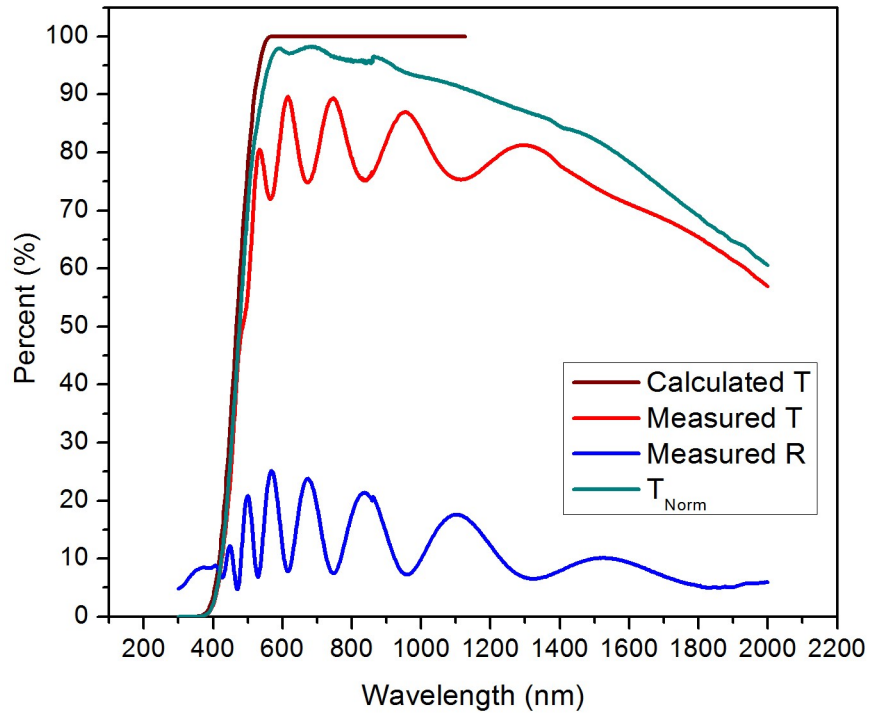


Figure 4.3: A comparison of transmission calculated via extinction coefficients obtained from VASE (brown) with normalized transmission obtained with spectrophotometry (green) for sample SP3118.7 with no heat treatment.

4.3.3 Glancing Incident Angle X-ray Diffraction

GIXRD data was taken using a Rigaku D/Max 2200 X-ray diffractometer. This data was taken using a fixed incident angle of 1° to restrict the sampling depth to the CTO film. Asymmetric detector measurements were taken over the 2θ range of 5° to 70° . This equipment allows for the structure of the sample to be studied to a depth of about 110 nm. An example of this technique is shown in Figure (4.4).

The primary use of the GIXRD measurements was to determine the crystal

structure of the CTO. This includes both the crystalline phase content and the degree of crystallization. Crystalline materials typically have a much higher mobility than amorphous materials as is the case for CTO [33]. Mobility is very important with regards to lateral conduction and high near-IR optical transmittance, requisite properties of a good TCO for thin film solar cells.

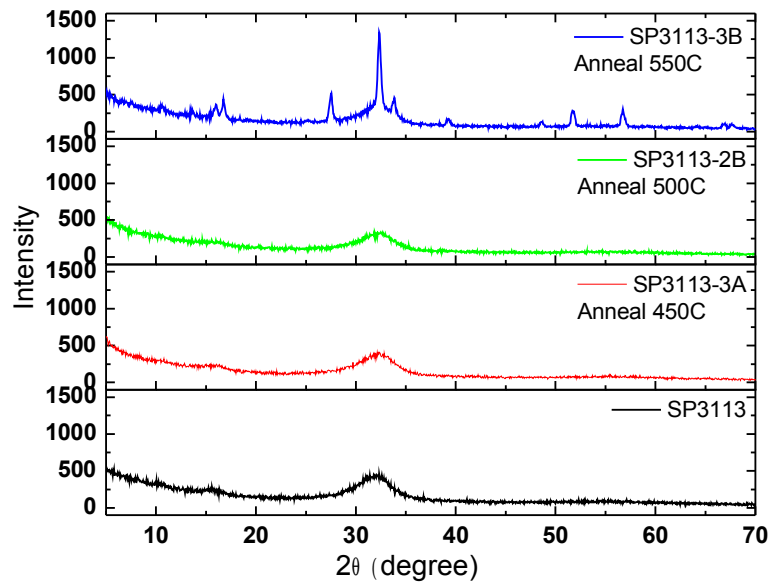


Figure 4.4: GIXRD spectra of SP3113, heat treated at different temperatures. This data shows that CTO crystallizes at about 550 °C. Below this temperature, the samples are considered amorphous.

GIXRD data is also very useful in determining if chemical phases other than the desired cadmium stannate are present in large amounts in the sample. Under certain conditions, the deposition process will yield a fair amount of by-product materials such as

cadmium oxide (CdO), as well as SnO₂ and CdSnO₃. These materials, especially CdO, negatively affect the optical and electrical properties of the TCO layer [30] [28].

Determining the presence of these by-products is an important aspect of developing a set of deposition and heat treatment conditions that yield useful results.

4.3.4 Energy-Dispersive X-Ray Spectroscopy

Energy-dispersive X-ray spectroscopy (EDS) was carried out using an Oxford Instruments EDS system in conjunction with an Amray 1810 scanning electron microscope (SEM). This EDS system is capable of a penetration depth of about 1 micron, allowing the full thickness of these samples to be studied. EDS analysis is incredibly important in determining the cadmium to tin (Cd/Sn) ratio of the samples, a key step in identifying the materials present in the CTO layer. Figure (4.5) shows example EDS data.

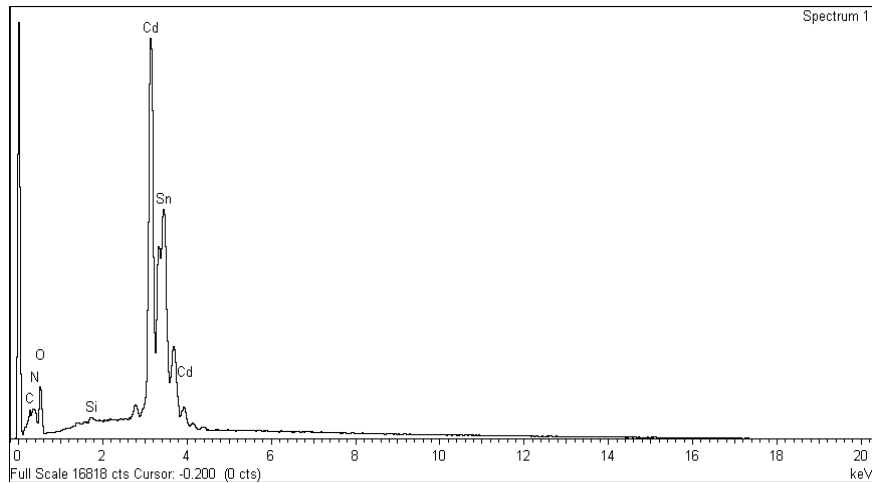


Figure 4.5: Example of EDS data for SP3151.2b, after being heat treated at 650 °C with CdS in Ar. This sample shows the desired (Cd/Sn) ratio.

4.3.5 Atomic Force Microscopy

A Digital Instruments Dimension 3100 series atomic force microscope was used to determine surface structure of the samples. The primary interest in these measurements is to determine the RMS roughness and depth of the surface roughness. Here, RMS roughness refers to the RMS depth value of a particular region, while the surface roughness depth refers to the maximum height from peak to valley of the surface roughness, over a particular region. This data is primarily useful to the ellipsometry data analysis. Surface roughness and grain size are also of relevance when considering transmission and reflection. Large RMS and depth for surface roughness and grain size will have a negative effect on transmission, due to scattering. Data was typically taken over a $2\ \mu\text{m} \times 2\ \mu\text{m}$ square. Surface roughness was determined independently for variously sized structures such as large and medium size grains as well as the surface between them. An example of this technique is shown in Figure (4.6).

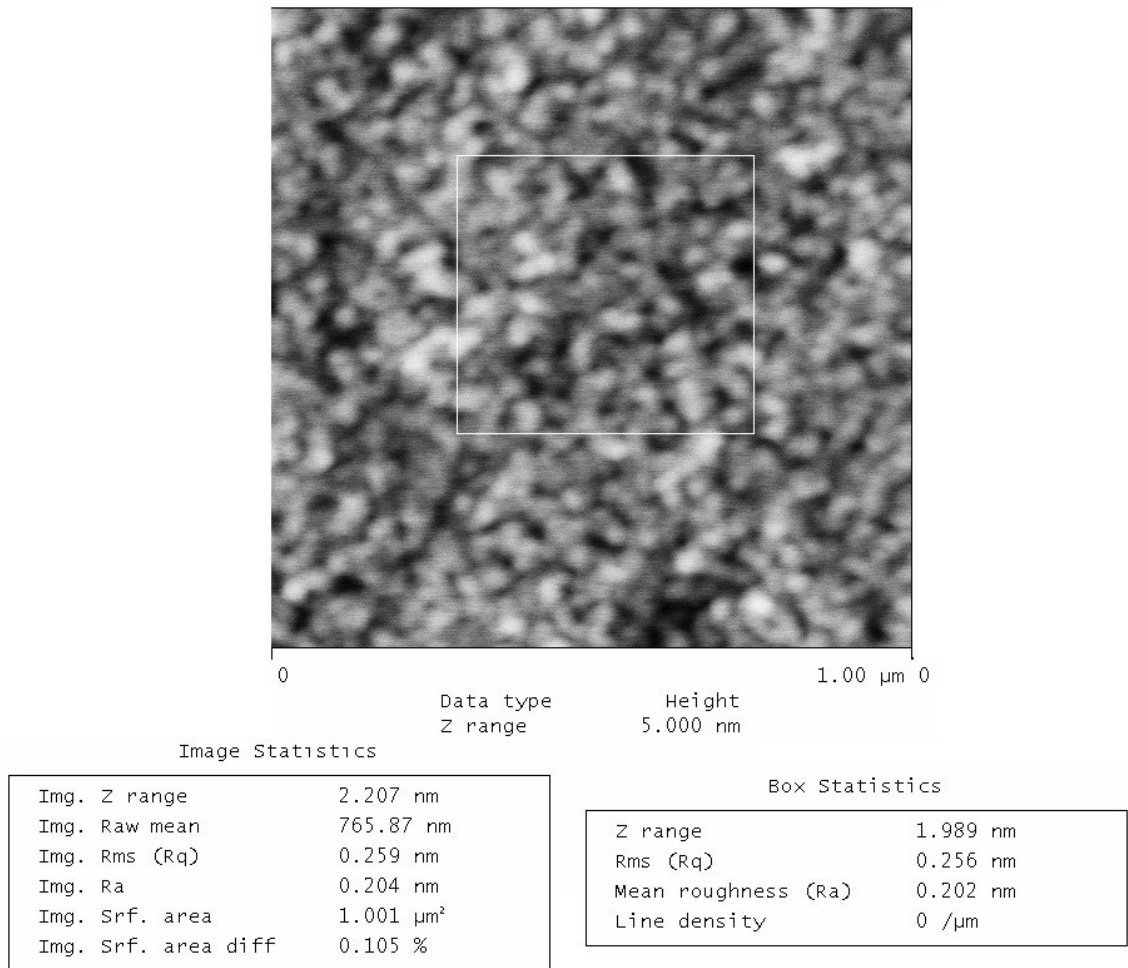


Figure 4.6: An example of AFM imaging for SP3118.7. Note the boxes beneath image indicating both RMS roughness and Z range of the whole image and of the selected box within the left image. Each image is one square micron.

4.3.6 Hall Effect and Van der Pauw

A custom built setup was used to measure both the cross-grain or lateral Van der Pauw (VDP) resistivity as well as Hall mobility and carrier concentration. The custom setup allowed for easy measurement of different cross-grain configurations of the system. This process involved several quick measurements followed by automatic calculation

once inserted into a spreadsheet.

Metallic contacts were added to the samples as shown in Figure (4.7). To determine resistivity, a current was caused to flow between contacts 1 and 2 while voltage was measured across contacts 3 and 4 (configuration 1). Three separate current values were used. This was repeated with reversed polarity for each current. Once these six measurements were taken, the sample was rotated 90 degrees and the entire process was repeated, with current now traveling between contacts 1 and 4 and voltage being measured between contacts 2 and 3 (configuration 2).

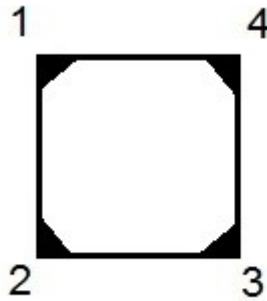


Figure 4.7: Diagram showing the location of the contacts used to determine sheet resistance and Hall mobility.

Each pair of polarity measurements were averaged together in order to eliminate offset voltages, such as thermoelectric potentials. The resistance for each of these

voltages was calculated and then the average resistance for the three currents used was determined, for each configuration. Sheet resistance could then be calculated using the Van Der Pauw formula [34]

$$e^{-\pi R_1/R_s} + e^{-\pi R_2/R_s} = 1 \quad (4.7)$$

where R_1 is the averaged resistance determined for configuration 1, R_2 is the averaged resistance determined for configuration 2 and R_s is the sheet resistance. This equation is not easily solvable. However, it is presumed that R_1 is approximately equal to R_2 .

Therefore, averaging these values where R is now the average resistance produces the value of the sheet resistance, via equation (4.8).

$$R_s = \frac{\pi R}{\ln(2)} \quad (4.8)$$

Once sheet resistance was determined, resistivity could be determined via the relationship $\rho = R_s t$, where t is the sample thickness.

Hall measurements were conducted at three different pairings of current and magnetic field to test for linearity. The Hall voltage for each set of values was recorded for both polarities of current and magnetic field. All of these voltage readings were then averaged to remove bias. From there, carrier mobility can be calculated via

$$\mu = \frac{V_H t}{IB \rho} \quad (4.9)$$

where V_H is the averaged Hall voltage, t is the thickness of the sample, ρ is the calculated resistivity and I and B are the magnitude values of the current and magnetic field,

respectively. Finally, the carrier concentration of the sample could be determined using the previously calculated values, via

$$n = \frac{1}{e \rho \mu} \quad (4.10)$$

where e is the charge of the electron.

Accurately determining the values for mobility, resistivity and carrier density is essential to the process of creating a good TCO thin film. Since resistivity is the inverse of conductivity, determining resistivity is directly important in determining how effective a conductor a given sample of CTO is. In order for these samples of CTO to be applicable in a solar cell configuration, high lateral conduction is very important. This is related not only to the resistivity/conductivity, but also to the thickness of the material. Rewriting equation (4.10), it is clear to see that conductivity is directly proportional to mobility and carrier concentration. As mentioned in Chapter 2, CTO has a great potential for very high carrier mobility. Because of this, a lower carrier concentration is required of the material. Some researchers believe that high carrier concentration, while good for improving conductivity and increasing the optical band gap, has a detrimental effect on absorption in the near infrared due to free-carrier absorption [16]. Ultimately, this high mobility should allow for a great deal of flexibility in the thickness of the CTO layer for various applications.

Chapter 5

RESULTS

Ideal conditions needed to obtain optimal CTO properties were divided into two categories: Deposition related (as deposited) and post-deposition heat treatment related (heat treated). Several trends in measured film properties were studied to identify how the material changed under different deposition and post-deposition treatment conditions. Specific focus was placed on the response of film resistivity, mobility, carrier density, band gap and transmittance to deposition and heat treatment conditions. In addition, the dependence of the optical function spectra structure on film stoichiometry (Cd/Sn ratio) and growth rate was also considered.

The samples were deposited on 4 inch by 4 inch square glass substrates, 1.5 mm thick. These initial 4 inch square samples were cut according to Figure (5.1). All data regarding pre-heat treatment deposition conditions was taken using the 1 inch by 2 inch cut number 7, unless otherwise noted. This cut was chosen due to the proximity to the center of the 4 inch by 4 inch sample.

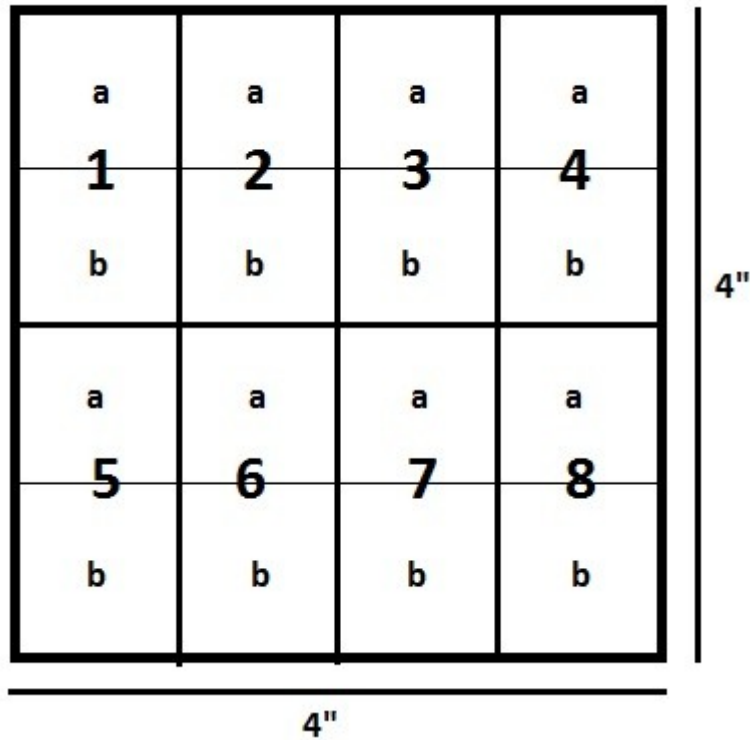


Figure 5.1: A diagram depicting how various cuts of the initial sample were labeled. The numbering corresponds to the initial cuts made of the sample, while the lettering corresponds to the sub-cuts of each numbered sample. All initial numbered samples are 1 inch wide by 2 inches tall. All lettered samples are 1 inch square.

For heat treated samples, the coated plates were cut down to 1 inch by 1 inch squares, as seen in Figure (5.1), to facilitate experimental throughput. It is important to note that due to the number and variety of heat treatments, many different sub cuts of each sample had to be used. Due to the slightly non-uniformity which can be obtained under certain conditions, particularly along the edges and at the corners of the 4 inch by 4 inch as-deposited samples, the use of sub cuts can contribute to apparent inconsistencies

in sample thickness, which shall be discussed further. It is suspected that center and edge thicknesses of the initial 4 inch by 4 inch sample may differ by as much as 20%, with more than 30% variation differences from center to corner.

5.1 Deposition Conditions

5.1.1 Temperature

Previous work [28] has shown that the properties of as-deposited CTO film preparations are not particularly deposition temperature-dependent. Optical and electrical properties of these thin films are largely dependent on their phase purity and crystal structure. However, to achieve satisfactory phase content and grain crystallization, high temperatures must be used. These temperatures, in the vicinity of 600 °C, are higher than can be achieved using the deposition heater. Samples deposited at temperatures below this will most likely exhibit signs of partial crystallization or mixed phases. Because of this, a heat treatment step is required in order to routinely form high quality films.

A comparison of samples deposited under identical conditions but at different temperatures shows the need for heat treatments. Figure (5.2) shows the GIXRD spectrum for samples deposited under identical conditions. One sample was deposited at room temperature (25 °C) while the other was deposited at high temperature (300 °C). From Figure (5.2), it is clear that there is no discernible difference in the crystal structure of these two samples. Further, it should be noted that neither of these films show signs of large scale crystallization. Figure (5.2) shows crystallization on the scale of nanometers.

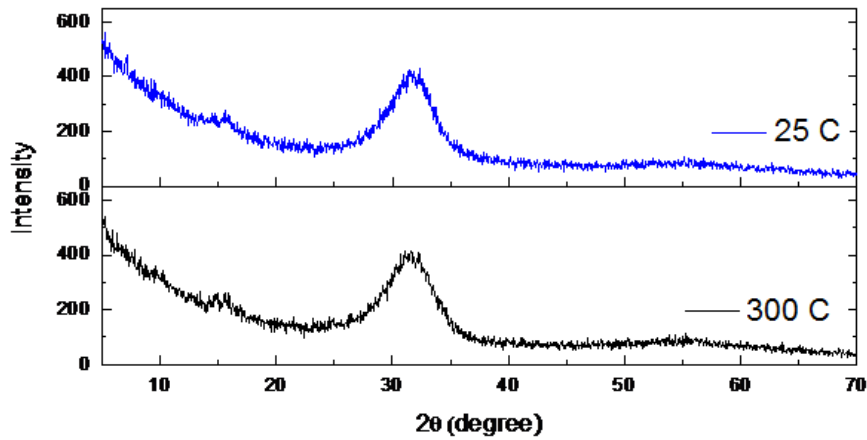


Figure 5.2: GIXRD data for CTO films deposited under 5 mT of pressure in a 1% oxygen environment at 25 °C and 300 °C. The rounded structures suggest small scale crystallization or amorphous structure.

Band gap and transmittance data for these two sets show more detail regarding temperature dependence. Figures (5.3) and (5.4) show very little difference in transmittance and extrapolated direct band gap for these films, despite the large difference in deposition temperature. Optically and structurally, these films both appear nearly identical.

In general, optical properties of films with temperature variations below 600 °C are not significantly different for different temperatures. The high thermal budget and time-intensive deposition process at high temperature is very likely not worth the slight shift in optical properties that was seen. Constant and uniform high temperature deposition is also harder to maintain and is expected to cause variations in the material

during the deposition process which reduces the quality of the final film. The process outlined by Wu [29] and based on Haacke [28] has shown that CTO with good optical and electrical properties can be easily obtained using a high temperature heat treatment. With this in mind, high temperature deposition is not necessary and should be regarded as ultimately non-ideal.

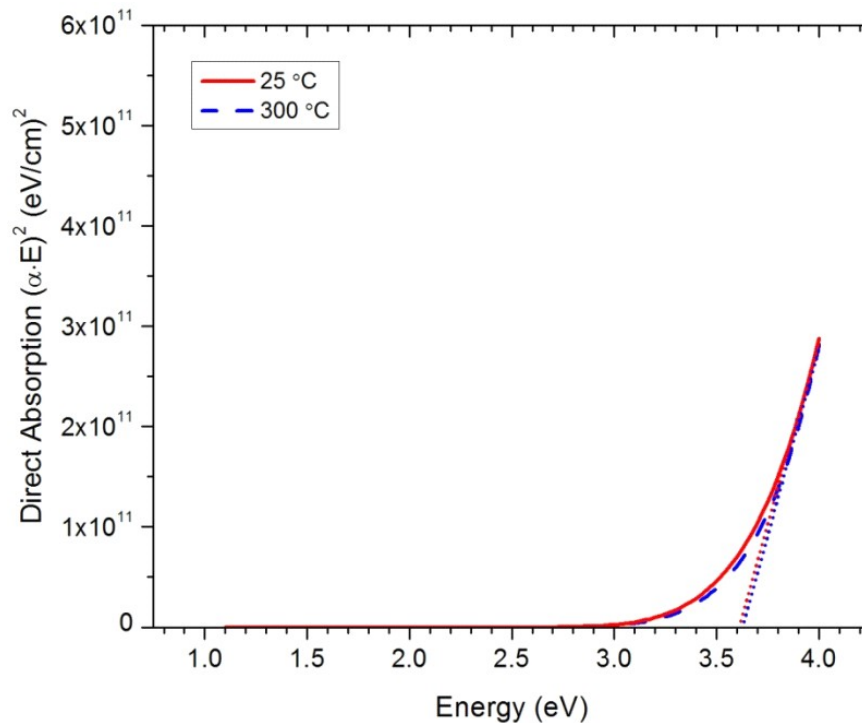


Figure 5.3: Direct band gap assessment for CTO films deposited under 5 mT of pressure in a 1% oxygen environment at 25 °C and 300 °C.

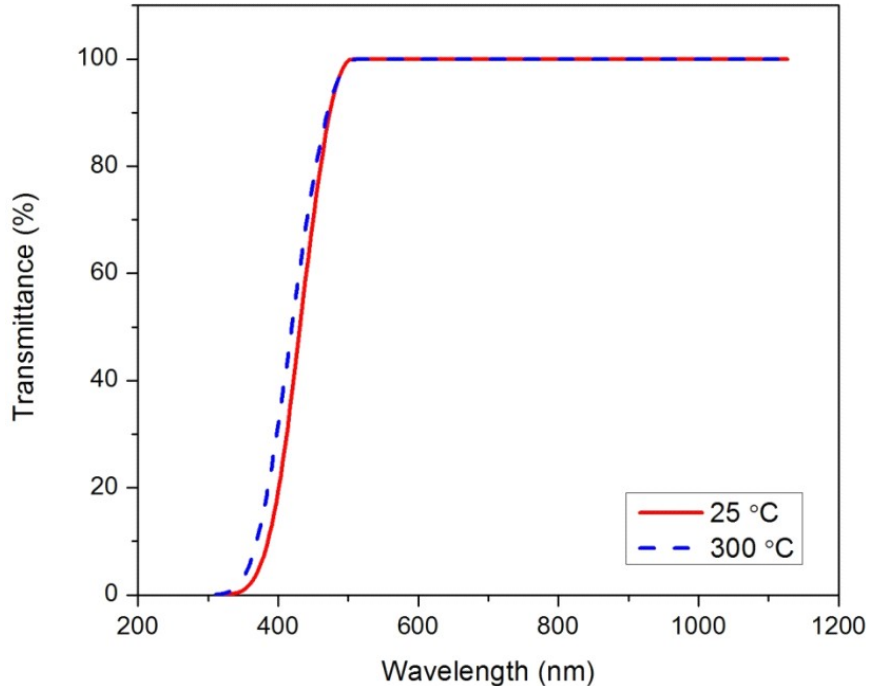


Figure 5.4: Transmittance for CTO films deposited under 5 mT of pressure in a 1% oxygen environment at 25 °C and 300 °C.

5.1.2 Atmospheric Oxygen Content

The oxygen concentration in the deposition ambient is a key component required for the deposition of high quality CTO films. Typically, samples were deposited in an atmosphere consisting of a mixture of argon and oxygen. For this work, oxygen content was varied from 0% to 50% of the atmosphere, with the balance being made up of argon, which was used as the primary sputtering gas in the ambient. As seen in Figure (5.5), the optical properties for films deposited with varying amounts of oxygen did not change dramatically. However, the transmission cut off, and hence band gap, varied systematically with respect to oxygen content, as seen in Figures (5.6) and (5.7).

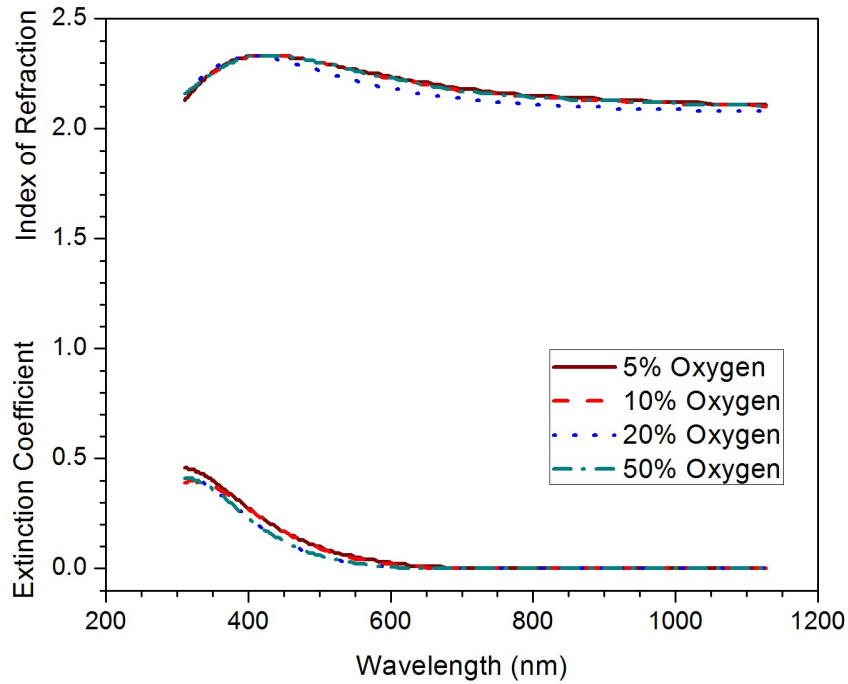


Figure 5.5: Optical constants for CTO films deposited at 10 mT and 25 °C, with varying oxygen.

Figure (5.7) reveals a nearly proportional shift of the transmittance absorption edge to shorter wavelengths with respect to increased oxygen content in the deposition atmosphere. The band gap changed less proportionally for these samples, as shown in Figure (5.6). As seen in Table (5.1), 50% oxygen gave the highest values of band gap, while 10% oxygen gave the lowest. 5% oxygen values were close to the 20% values, suggesting that there exists a local minimum value for band gap with respect to oxygen. Both band gap fits exhibited linear regimes, which may indicate a mixing of direct and indirect band gap states in these samples. However, whereas the indirect fits were only linear over a factor of 2, the direct fits were linear over an order of magnitude.

Insufficient area resolution in the optical measurements precludes determining the existence of grains with differing optical properties in the areas sampled by the ellipsometer or spectrophotometer.

With this resolution issue in mind, it may be prudent to consider more strongly the direct band gap results here. As seen in Figure (5.6), the band gap values for all samples ranges from 3 eV to 3.25 eV. Keeping this in mind, the accepted value for band gap for CTO is approximately 3.7 eV. Similarly, the band gaps for CdO and SnO₂ are 2.1 eV and 3.0 eV, respectively. The band gap for CdSnO₃ has yet to be determined. Considering these band gap values, it is unlikely that these samples contain CTO in any quantity. The spread of band gap values combined with the very low values suggest that these materials are some sort of collection of mixed material phases of CTO. This issue will be addressed further in Section 5.2.1.

Oxygen levels during deposition decreased the film growth rate exponentially with higher levels of oxygen in the ambient atmosphere, as seen in Figure (5.8). This is most likely due to changing sputtering dynamics with varying concentrations at a fixed total pressure. As the oxygen concentration increased, the argon concentration in the atmosphere was reduced, resulting in a lower impact frequency and a lower sputtering rate at the target. This interpretation is qualitatively consistent with the effect of total pressure on deposition rate described later.

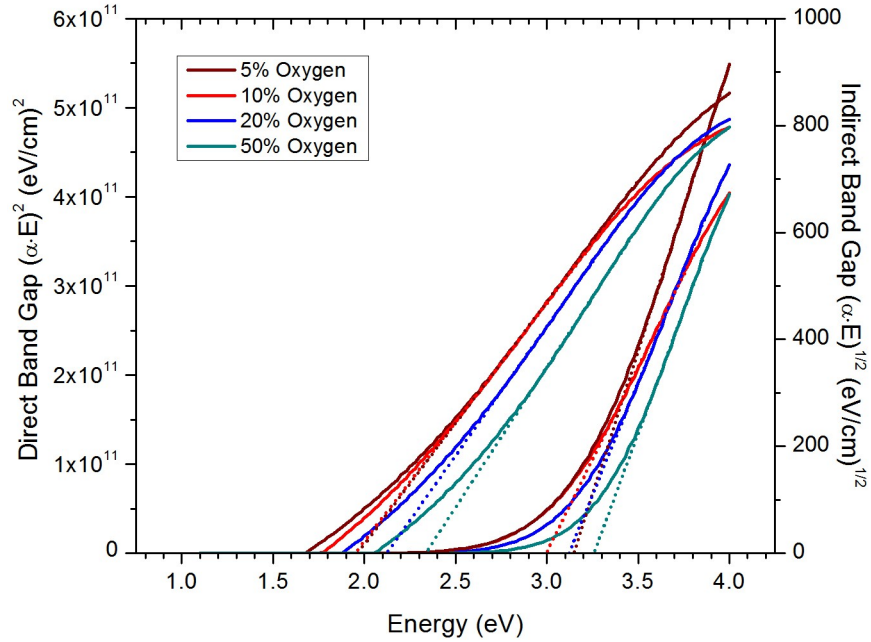


Figure 5.6: Indirect (left group) and direct (right group) band gap assessment for CTO films deposited at 10 mT and 25 °C, with varying oxygen.

Table 5.1: Band gap values for samples deposited in atmospheres with varying oxygen percentage. Values are approximate.

	5% Oxygen	10% Oxygen	20% Oxygen	50% Oxygen
Direct Band Gap (eV)	3.15	3	3.1	3.25
Indirect Band Gap (eV)	1.95	1.95	2.1	2.35

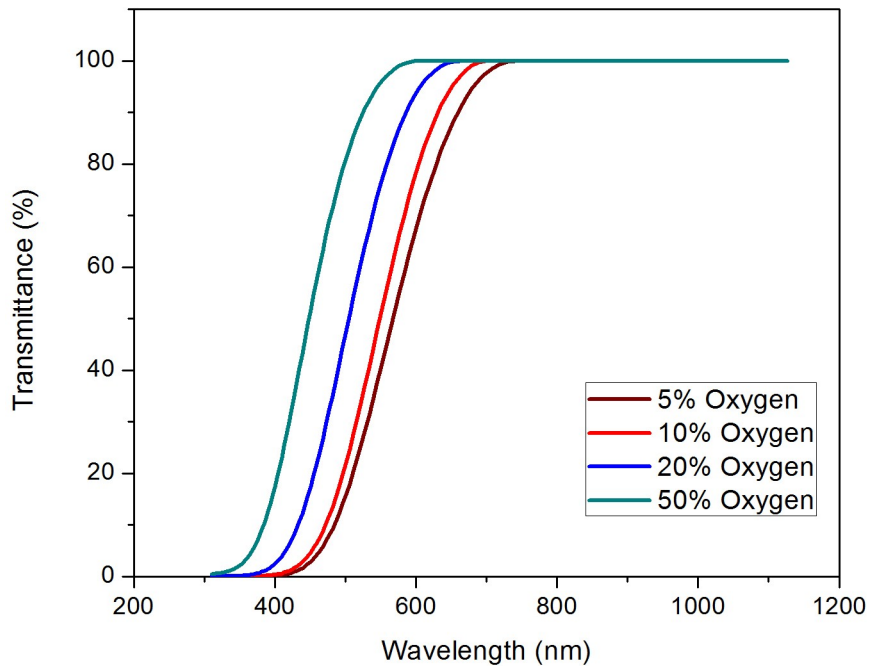


Figure 5.7: Transmittance for CTO films deposited at 10 mT and 25 °C, with varying oxygen.

Ultimately, most samples were deposited at a relatively low percentage of oxygen, typically 5% or 10%. This percentage resulted in the best post-deposition optical properties, as well as the fastest growth time. The optical properties of these materials are further improved during heat treatment.

It is also of importance to note that oxygen permits stoichiometric control of the film. At an ambient content of 5%, the proper film stoichiometry is achieved, allowing the correct phase of CTO to be obtained on recrystallization. This stoichiometry is usually expressed as the Cd/Sn ratio, which ideally equals 2. This ratio was measured in the films using EDS. For this series, the Cd/Sn ratio was nominally 1.96, with the

exception of the sample run under 10% oxygen, which produced a the ratio of 2.09. This result is unusually high and is currently unexplained. In general, however, the Cd/Sn ratio for these samples is good, and heat treatments will be shown to further increase the ratio to the desired value.

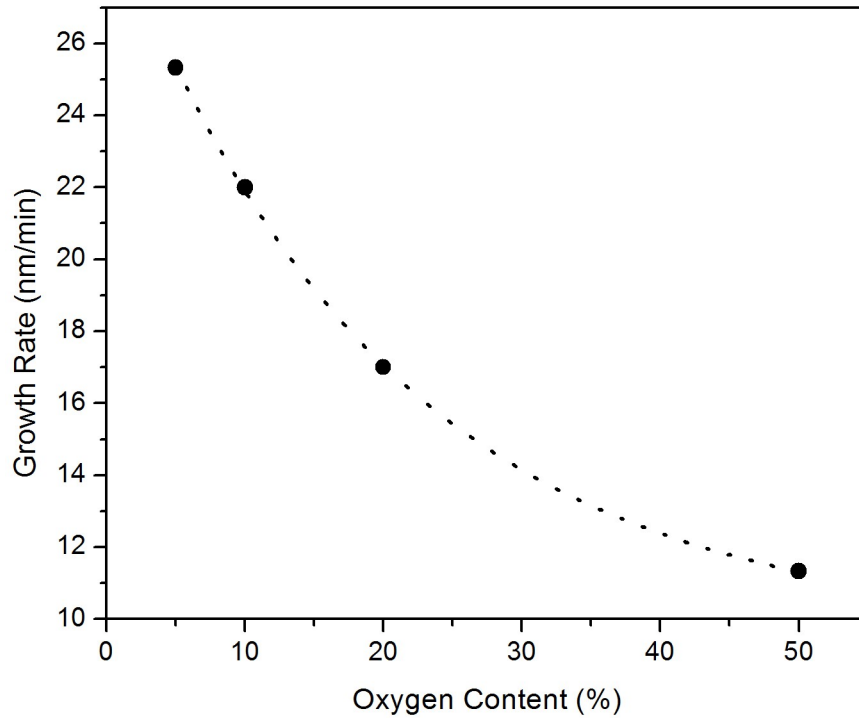


Figure 5.8: Growth rate versus oxygen content for CTO films deposited at 10 mT and 25 °C. The remaining percent of the atmosphere is argon gas.

5.1.3 Sputtering Ambient Pressure

The variation in sputtering ambient pressure used for deposition wasn't initially expected to greatly affect the optical properties of deposited samples. However, this was not the case. Several different runs were attempted, fixing oxygen content at 1% and varying total ambient pressure from 5 mT to 15 mT, all at 300 °C. This data set ultimately provides further evidence against using high temperature deposition. The highest pressure sample was deposited on CSG, while the two lower pressure samples were deposited on SLG.

Figure (5.9) shows that the optical constants for the pressure-dependent series films are more affected than the previous oxygen-dependent series. The spread of the absorption edge in the extinction coefficient is far more pronounced here than in Figure (5.5). Also of interest is the change in structure of the index of refraction for the 15 mT run. This may be due to the change in substrate material between the lower pressure runs and this higher pressure run, however the optical constants for each of these types of glass are nearly identical, as can be seen in Figure (5.10). If the change in substrate were the cause, it is suspected that the interface between the material and substrate layer is responsible.

Transmittance behaves similarly to that for the oxygen dependence series. The absorption edge moves to longer wavelengths as pressure increases, as can be seen in Figure (5.11). For both the direct and indirect band gap models, the value of the band gap

depends on the pressure during deposition. As pressure increases, the band gap shifts to lower energy values. Table (5.2) and Figure (5.12) contain data regarding the band gap behavior of these samples.

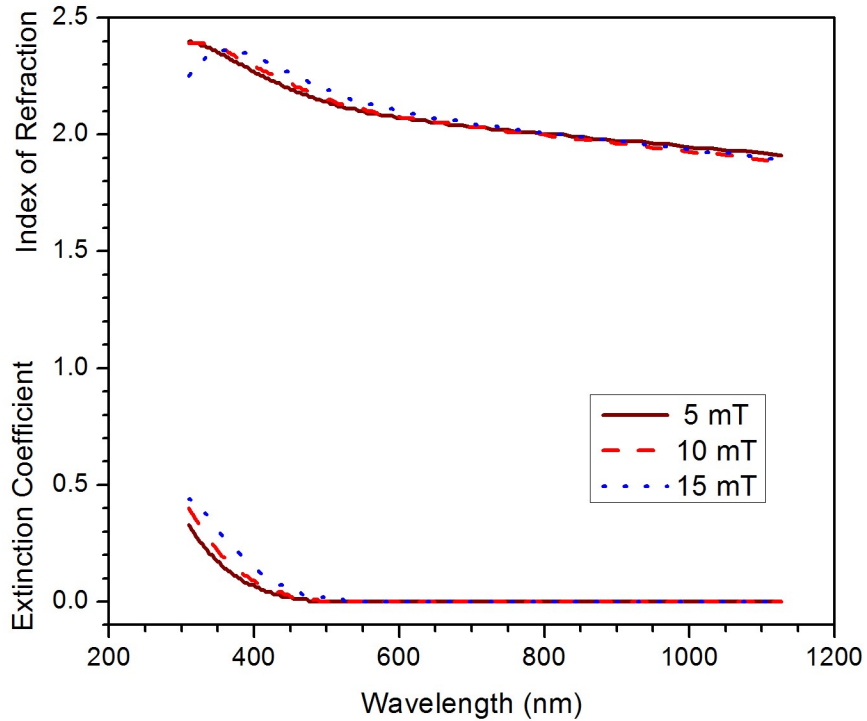


Figure 5.9: Optical constants for CTO films deposited in 1% ambient oxygen and 300 °C, with varying pressure.

Figure (5.12) contains interesting behavior regarding the band gap response of these samples. Similar to the oxygen dependence series, this series shows fairly good fits for band gap using both models, again suggesting mixed states. However, the fit for samples deposited at high pressure appears to be more linear in the direct band gap model than the indirect model. This is exactly opposite for the low pressure sample. This seems

to suggest that the pressure plays an important role in how the crystal structure develops during deposition of these materials, with the low pressure model displaying what could be interpreted as a more amorphous structure than the high pressure model.

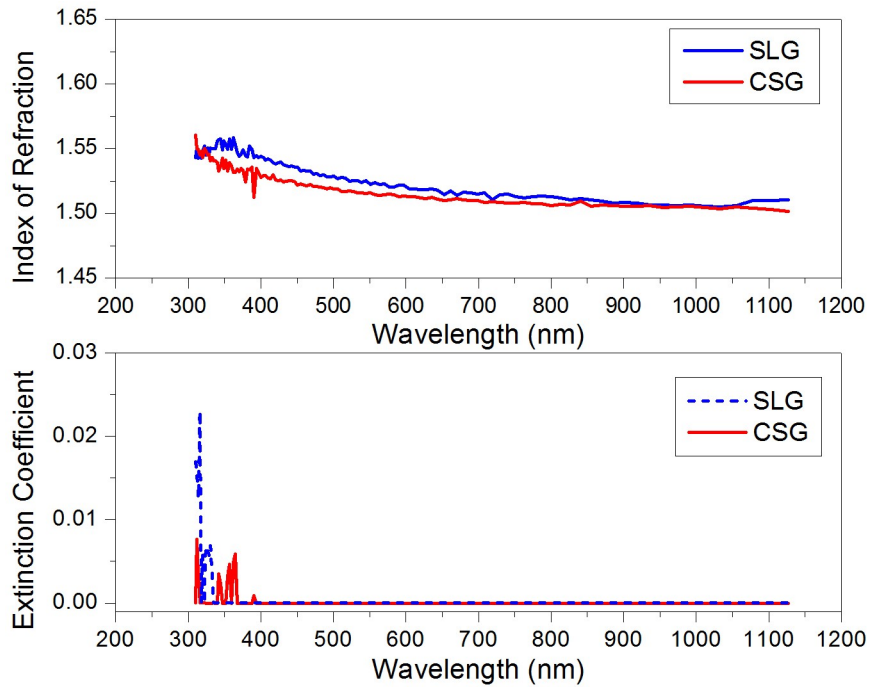


Figure 5.10: Optical constants for SLG and CSG glass. Note that all figures show a very small degree of variation.

It is important to note that over the pressure range used, film growth was linearly dependent on pressure, with the growth rate of the low pressure sample being about 18.7 nm per minute and the growth rate of the high pressure sample being about 24.5 nm per minute. As mentioned earlier, this result suggests that high pressure encourages film growth.

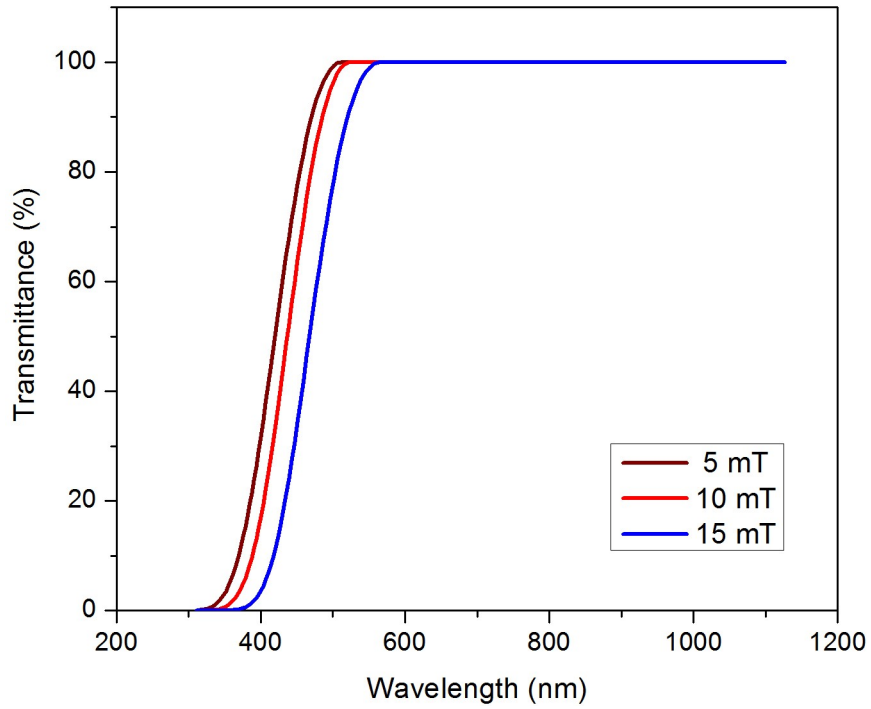


Figure 5.11: Transmittance for CTO films deposited in 1% ambient oxygen and 300 °C, with varying pressure.

Table 5.2: Table of band gap values for samples deposited under varying pressure. Values are approximate.

	5 mT	10 mT	15 mT
Direct Band Gap (eV)	3.65	3.5	3.4
Indirect Band Gap (eV)	2.6	2.55	2.45

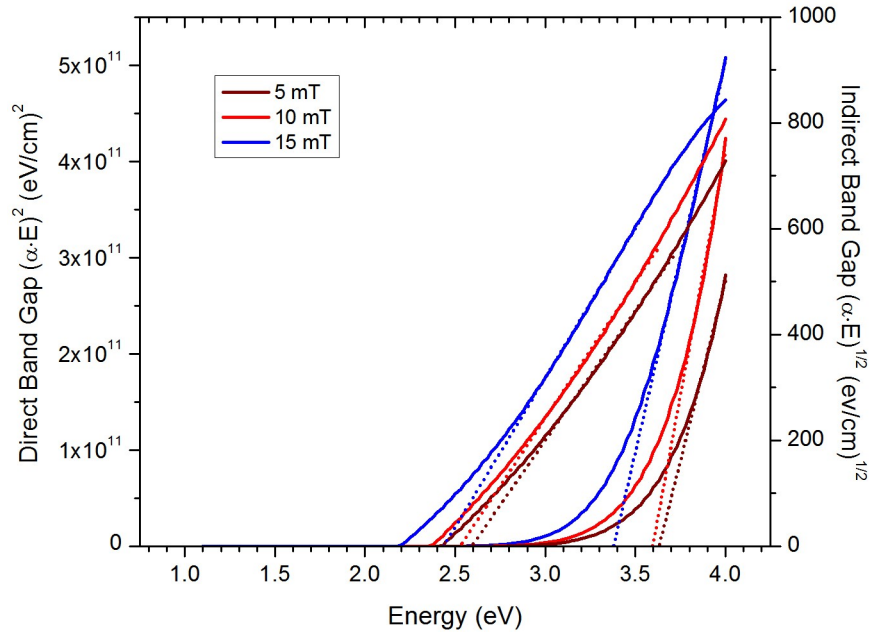


Figure 5.12: Indirect (left group) and direct (right group) band gap assessment for CTO films deposited in 1% ambient oxygen and 300 °C, with varying pressure.

Ultimately, the most useful data obtained from this series was the dependence of Cd/Sn ratio on ambient sputtering pressure. The Cd/Sn ratio varied from .84 at 5 mT to 1.14 at 10 mt to 1.64 at 15 mT. As previously mentioned, the Cd/Sn ratio for stoichiometric cadmium stannate is 2. Such low ratios in the measured films strongly suggest that these samples are not cadmium stannate or contain excess Sn-containing phases. Unfortunately, GIXRD for these samples show no discrete peaks, even after heat treatment. Most likely, different phases of CTO such as CdO, SnO₂ and CdSnO₃ co-exist in this sample. As mentioned in section 5.1.1, deposition conducted at temperatures below 600 °C are likely to contain mixed phases. Room temperature deposition produces

samples with a Cd/Sn ratio much closer to 2, suggesting that cadmium stannate, if not currently present in the material due to mixed phases, will be producible during heat treatment. These results further suggest that room temperature deposition is the most practical way to deposit CTO samples.

The previous section has shown that film growth rate strongly depends on the atmospheric argon pressure. As seen in Figure (5.13), growth rate decreases proportionally as pressure decreases. This is due to a decrease in impact frequency, causing a decrease in growth rate. These results support the previous explanation of how increased oxygen content reduces growth rate, by reducing argon concentration. A comparison of these two sample series can be seen in Figure (5.14). Here, growth rate is shown as a function of argon pressure for both series. Despite an imperfect match of the slopes of the two sets, the fact that both series have a positive slope over similar ranges supports the argon pressure dependence of growth rate. The difference in behavior of each of these series may be dependent on other parameters, such as deposition temperature.

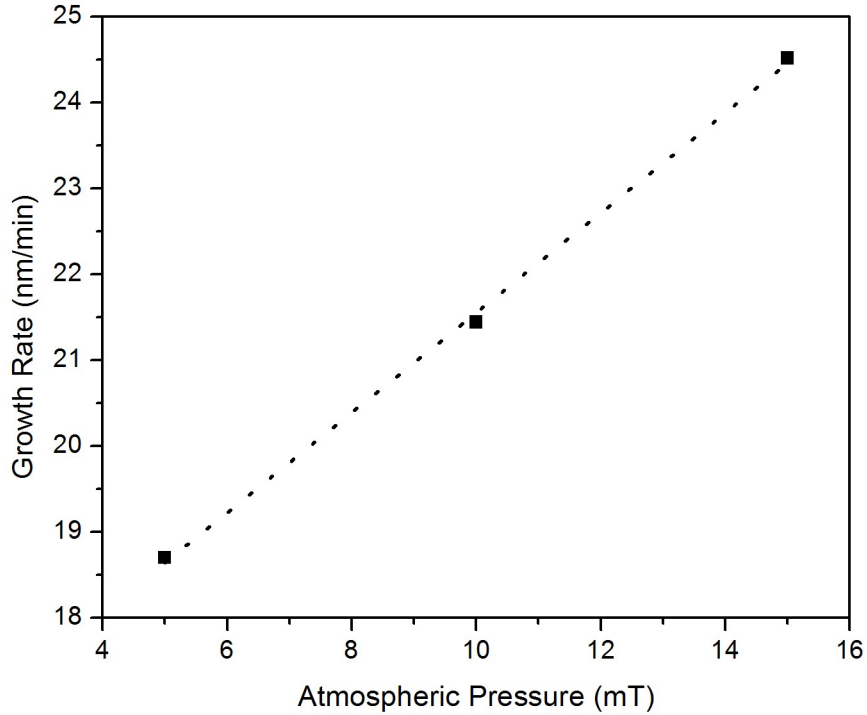


Figure 5.13: Growth rate for CTO films deposited in 1% ambient oxygen and 300 °C, with varying pressure.

An additional point to be made regarding Cd/Sn ratio concerns the impact of multiple phase inclusion on the interpretation of the optical results of films intended to be cadmium stannate. Considering the strong dependence of Cd/Sn ratio in the films on sputtering pressure, it is possible that high pressure deposition favors cadmium adherence to the substrate during deposition. The variation apparent “sticking coefficient” of cadmium at the substrate is a reasonable explanation for the measured variation in optical properties in this sample set, and may apply to CTO deposition in general.

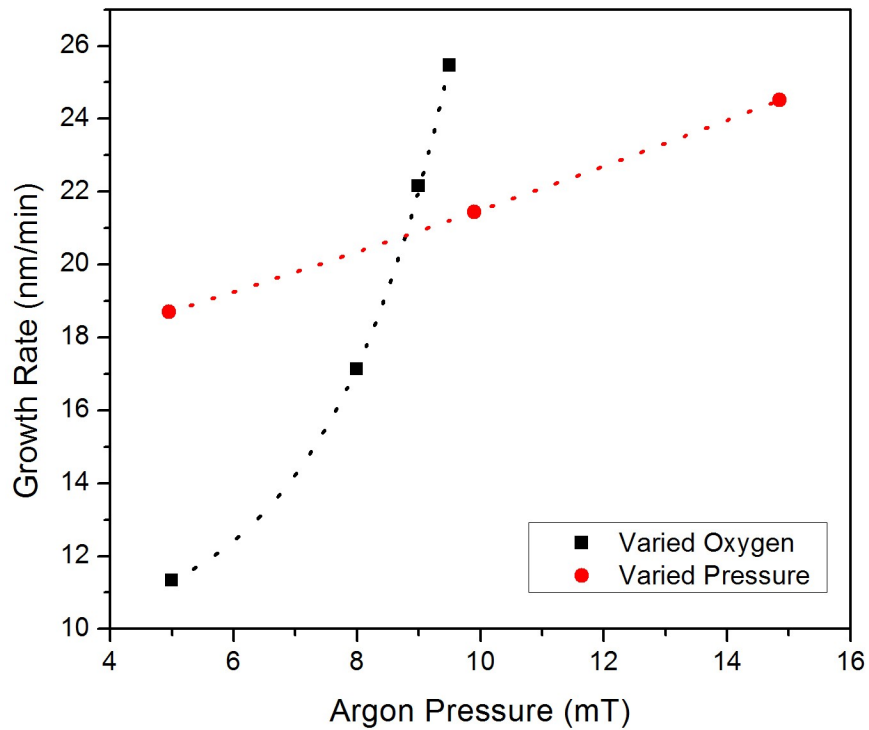


Figure 5.14: Comparison of growth rate for the pressure dependent series and the oxygen dependent series. Argon pressure was determined for each series by calculating the partial pressure for an ideal gas.

5.1.4 Summary

In general, both oxygen content and pressure of the ambient atmosphere during deposition exert a strong role in film growth rate, Cd/Sn ratio and optical properties. It should be noted that these two parameters are most likely correlated. A deposition under high pressure with high oxygen content may yield similar results, regarding growth rate, to a deposition with proportionally lower values of oxygen content and pressure, due to the effect pressure and ambients have on the sputtering gas. In general, this is due to ambient oxygen content contrasting with how the pressure enables cadmium to adhere to

the substrate. In this way, the desired stoichiometry for cadmium stannate can be fine-tuned, by adjusting these conditions.

Further, room temperature deposition is preferred to high temperature deposition. This is due to the threshold temperature needed for crystallization being too high to be achieved by the heater in the deposition chamber. Furthermore, high temperature deposition is very time and cost inefficient, while also adding a degree of possible grading to the sample due to temperature instabilities. All of these factors combine to suggest that room temperature deposition will be the method that produces the highest quality CTO until the ability to easily deposit CTO under very high temperatures is perfected.

5.2 Heat Treatment Conditions

5.2.1 Effect of Atmospheric Oxygen Content After Heat Treatment

The effects of post-deposition heat treatments were examined on a selected set of samples. It is natural to use films with Cd/Sn ratio nearly equal to 2 so that a reasonable expectation for studying phase-pure cadmium stannate films can be realized. The series first mentioned in section 5.1.2 that was deposited under varying oxygen conditions was later exposed to the same heat treatment, to study the effect deposition oxygen levels had on a final CTO material layer. All of these samples were heated for 30 minutes at 600 °C in an argon atmosphere in parallel, close proximity (less than 1 mm) contact with a CBD CdS sample, as described by Wu [29]. The electrical and material properties for each of

these samples are shown in Table (5.3) as the series from SP3144-6a to SP3147-6a. As-deposited material properties for the samples are shown in Table (5.4).

It is worth mentioning that all samples showed an increase in the Cd/Sn ratio after heat treatment, with the exception of the sample in 50% oxygen. Further, resistivity improved nearly linearly as a function of decreasing oxygen levels, with a dramatic improvement between 5% and 10% oxygen content. Carrier mobility was significantly higher for the two lower oxygen runs. However, carrier density was also higher for the lower oxygen runs, decreasing with increasing oxygen in an approximately linear fashion, which may be non-ideal. It is important to note that the electrical properties of the original samples were unable to be measured at all, indicating that the post-deposition samples were insulating.

Optical constants for the heat treated samples differ dramatically from those of the as-deposited films, as shown in Figure (5.15), especially at long wavelength. At lower wavelengths, the general structure has also changed, although less dramatically. The extinction coefficient also takes on a far steeper absorption edge than previously seen. This change in the extinction coefficient is further shown in Figures (5.16) and (5.17).

Table 5.3: A table depicting all deposition and heat treatment variables for the heat treated samples relevant to this work. Data regarding non-optical properties of the samples is also included. It should be noted that all samples were fitted using the VASE software to an MSE value of 10 or below.

Sample ID	Pressure (mT)	Oxygen (%)	Dep. Temp. (C)	Dep. Time (min)	Heat Treat Temp. (C)	Heat Treatment Environment	Heat Treat Time. (min)	Center Thickness After Dep. (nm)	VASE Model Thickness (nm)	VASE Model MSE	Cd/Sn Ratio	Resistivity ($\Omega\cdot\text{cm}$)	Sheet Resist. (Ω/sq)	Mobility (cm^2/Vs)	Carrier Density (cm^{-3})
SP 3144-6A	10	50	25	30	600	Ar/CBD CDS	30	660	350.20	6.29	1.93	3.04×10^{-4}	8.70	40.42	5.08×10^{22}
SP 3145-6A	10	20	25	30	600	Ar/CBD CDS	30	660	516.77	4.23	2.03	2.35×10^{-4}	4.69	40.07	6.65×10^{22}
SP 3146-2B	10	10	25	30	600	Ar/CBD CDS	30	660	729.36	4.11	2.1	2.15×10^{-4}	2.91	45.98	6.32×10^{22}
SP 3147-6A	10	5	25	30	600	Ar/CBD CDS	30	660	792.46	9.50	2.08	1.69×10^{-4}	2.22	46.17	8.02×10^{22}
SP 3146-2B	10	10	25	30	600	Ar/CBD CDS	30	660	729.36	4.11	2.1	2.15×10^{-4}	2.91	45.98	6.32×10^{22}
SP 3148-2B	10	10	25	20	600	Ar/CBD CDS	30	430	492.16	7.97	2.05	1.98×10^{-4}	4.03	47.34	6.68×10^{22}
SP 3149-2B	10	10	25	10	600	Ar/CBD CDS	30	240	257.81	8.26	1.92	1.83×10^{-4}	7.03	49.28	6.94×10^{22}
SP 3150-2B	10	10	25	5	600	Ar/CBD CDS	30	100	112.80	4.37	1.83	1.62×10^{-4}	14.74	51.93	7.42×10^{22}
SP 3151-6A	5	5	25	30	550	Ar/CBD CDS	30	820	879.11	8.92	2.03	4.54×10^{-4}	5.54	39.39	3.49×10^{22}
SP 3151-2A	5	5	25	30	600	Ar/CBD CDS	30	820	837.90	7.95	2.0	1.60×10^{-4}	1.95	55.63	7.20×10^{22}
SP 3151-2B	5	5	25	30	650	Ar/CBD CDS	30	820	821.48	8.79	2.07	2.14×10^{-4}	2.61	46.02	6.34×10^{22}
SP 3151-4A	5	5	25	30	600	N ₂ /CBD CDS	30	820	612.29	9.37	1.97	2.13×10^{-4}	2.59	49.17	5.98×10^{22}
SP 3151-1A	5	5	25	30	600	Ar	30	820	666.66	9.75	1.91	4.18×10^{-4}	6.23	57.61	2.60×10^{22}
SP 3151-4B	5	5	25	30	600	Ar/CBD CDS	30	820	709.55	6.44	1.82	35.3×10^{-4}	42.98	5.33	3.39×10^{22}

Table 5.4: Table of pre-heat treatment properties for all samples from Table (5.3).

Sample ID	Pressure (mT)	Oxygen (%)	Dep. Temp. (C)	Dep. Time (min)	Center Thickness After Dep. (nm)	Cd/Sn Ratio	Resistivity (Ωcm)
SP3144-7	10	50	25	30	660	1.97	Insulating
SP3145-7	10	20	25	30	660	1.95	Insulating
SP3146-7	10	10	25	30	660	2.09	Insulating
SP3147-7	10	5	25	30	660	1.98	Insulating
SP3146-7	10	10	25	30	660	2.09	Insulating
SP3148-7	10	10	25	20	430	N/A	Insulating
SP3149-7	10	10	25	10	240	N/A	Insulating
SP3150-7	10	10	25	5	100	N/A	Insulating
SP3151-7	5	5	25	30	820	N/A	Insulating

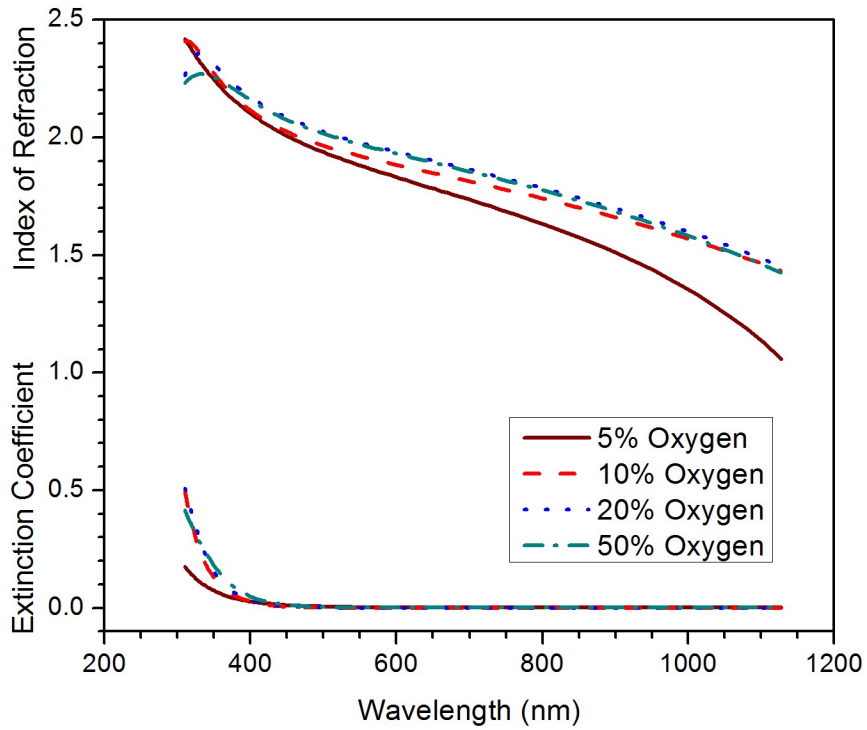


Figure 5.15: Optical constants for CTO films deposited at 10 mT and 25 °C, with varying oxygen. All samples heat treated at 600 °C.

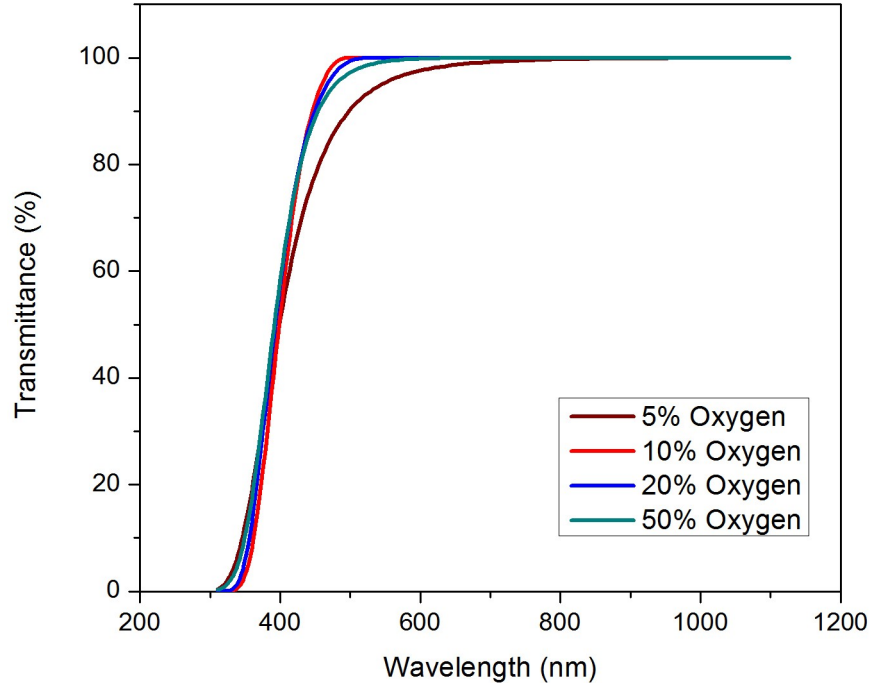


Figure 5.16: Transmittance for CTO films deposited at 10 mT and 25 °C, with varying oxygen. All samples heat treated at 600 °C.

Comparing the optical transmittance of as-deposited and heat-treated films deposited at 10 mT and 25 °C at different oxygen concentrations, and treated at 600 °C in argon, as seen in Figures (5.7) and (5.16), shows a strong effect of the thermal treatment. The transmission edge shifts in all cases towards lower wavelength, indicating a band gap shift towards higher energy by the treatment. These samples no longer display the oxygen dependence seen for transmittance after deposition only. All samples display an absorption edge at approximately 400 nm, with only the transmittance immediately leading up to the absorption edge being affected by oxygen content. This is a very

interesting development, considering the as-deposited transmittance for these same samples as seen in Figure (5.7) showed absorption edges over a wide range.

The optical band edge structure is also changed by the heat treatment, as shown in Figure (5.17) in which direct band gap transition seems to be the best fit to the absorption data. In addition, the data regarding the sample deposited in 5% oxygen suggests a higher band gap than expected during data acquisition: Ellipsometry data was only acquired up to a maximum energy of 4 eV, hence the sudden cut off of the linear portion of the 5% oxygen sample. Due to this lack of data, determining the exact value for the band gap for this sample is unreliable, but it seems reasonable from the trend and the shape of the obtained data that the actual band gap will be the highest of the four. Further attempts to acquire data higher than this range have proved difficult, due to the strong absorption of light at these higher energies.

Table (5.5) shows the band gap trend for these samples. The shift from a spread of data for band gap values to a nearly single value for direct band gap indicates that these films, after heat treatment, are no longer mixed phase due to a chemical process that takes place during heat treatment. This is further supported by the change in the shape of the optical properties as seen in Figure (5.15), as well as the transmittance spectra as seen in Figure (5.16).

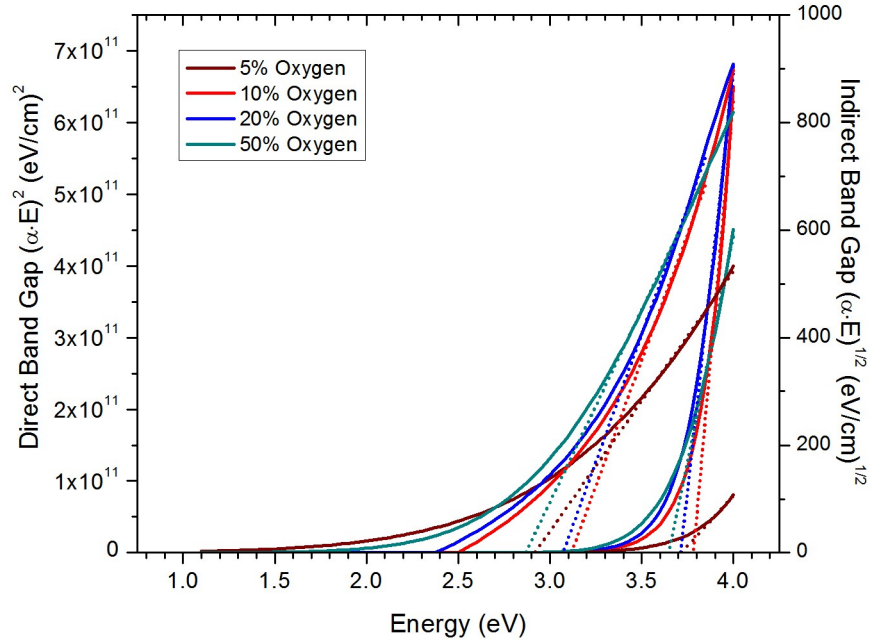


Figure 5.17: Indirect (left group) and direct (right group) band gap assessment for CTO films deposited at 10 mT and 25 °C, with varying oxygen. All samples heat treated at 600 °C.

Table 5.5: Table of band gap values for samples deposited in atmospheres with varying oxygen percentage, after heat treatment. Values are approximate.

	5% Oxygen	10% Oxygen	20% Oxygen	50% Oxygen
Direct Band Gap (eV)	3.7 (?)	3.8	3.7	3.65
Indirect Band Gap (eV)	2.9 (?)	3.1	3.1	2.9

The changes incurred during the heat treatment are possibly due to a physical process outlined by Wu and Coutts. They stated that:

It is believed that during heat treatment, CdS vapor is sublimated from the CdS layer and diffuses into the CTO crystal lattice, creating interstitial Cd and oxygen vacancies and reducing the quantity of secondary phases present. X-ray diffraction data obtained for treated samples indicate a single spinel crystal structure having a slightly larger lattice constant than CTO without interstitial cadmium [29].

Brian McCandless, an associate scientist at the Institute of Energy Conversion, has further elaborated on this suggested process.

CdS sublimation occurs primarily via decomposition into Cd and S₂ vapor, with these sub-molecular species diffusing into the film network, where a new equilibrium is established between Cd and S excess and the point defects formed during deposition. In cases where Cd/Sn < 2, the Cd vacancies are eliminated through reaction with the vapor, which likely promotes recrystallization and interphase reaction. A thermodynamic evaluation of this system would likely favor the stable single ternary phase Cd₂SnO₄ in lieu of an admixture of CdSnO₃ and SnO₂. The spinel, once formed, is a very stable configuration. The sulfur lowers the surface energy for both Cd and Sn lattice sites, overcoming the pinning effect of oxidation, and allowing reaction towards the spinel to proceed [35].

The values for direct band gap shown in Figure (5.17) indicate that this process has taken place, causing the mixed phase materials composing the film to settle into a spinel structure of CTO, with the proper band gap of about 3.7 eV. However, single phase films having high oxygen content may contain fewer interstitial oxygen vacancies. Therefore, if these vacancies control the electrical and optical quality of the film, then it is plausible that incorporation of excess oxygen may result in films with non-ideal optical and electrical properties.

Additionally, the shift in band gap structure from indirect to direct is worth some discussion. This is likely due to the crystallization of the CTO layer. Many spinel semiconductors [36] [37] are direct band gap semiconductors, as is true for CTO [38]. The indirect band gap data was included in Figure (5.17) as further evidence of this crystallization. Poorly fitting band gap data will no longer be shown.

5.2.2 Thickness Dependence

In order to quantify the thickness dependence of the optical and electrical properties in sputtered CTO films, a series of samples was deposited under the same deposition conditions for different lengths of time, producing samples with varying thickness. These samples were further heat treated at 600 °C in an argon atmosphere in direct contact with a CdS sample, for 30 minutes. Any obtained variations are thus likely to be due to depth-dependent effects of the treatment, not necessarily those of the as-deposited film. These properties and the non optical results of this series can be seen in Tables (5.3) and (5.4) for the series ranging from SP3146-2b to SP3150-2b. Thicknesses range from approximately 110 nm up to 730 nm.

Optical properties for these films, as seen in Figure (5.18), look similar to those from Figure (5.15), which were also heat treated at 600 °C. There does not appear to be a great deal of variation in extinction or refraction. Upon looking at the model for the band gap of these materials as seen in Figure (5.19), a situation similar to the 5% oxygen run shown in Figure (5.17) is clear. With the exception of the thickest sample, the data range

these samples were analyzed at is too small to accurately capture the band gap. However, a general trend can still be inferred. In general, it appears that the band gap is inversely correlated with film thickness. Further study of these very high band gaps is necessary to better verify this trend.

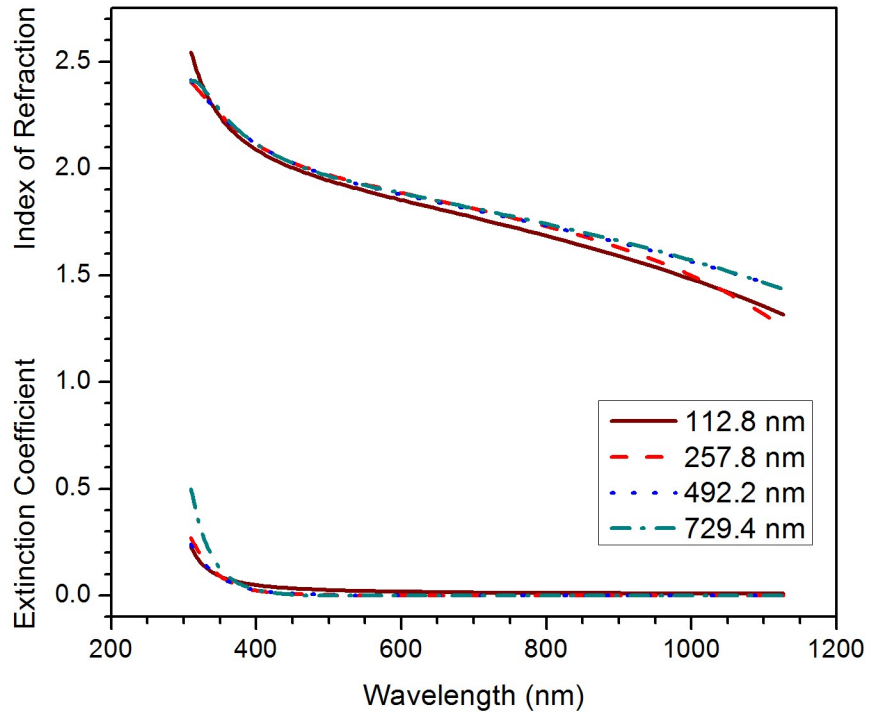


Figure 5.18: Optical constants for CTO films deposited at 10 mT, 10 % oxygen and 25 °C, with varying thickness. All samples heat treated at 600 °C.

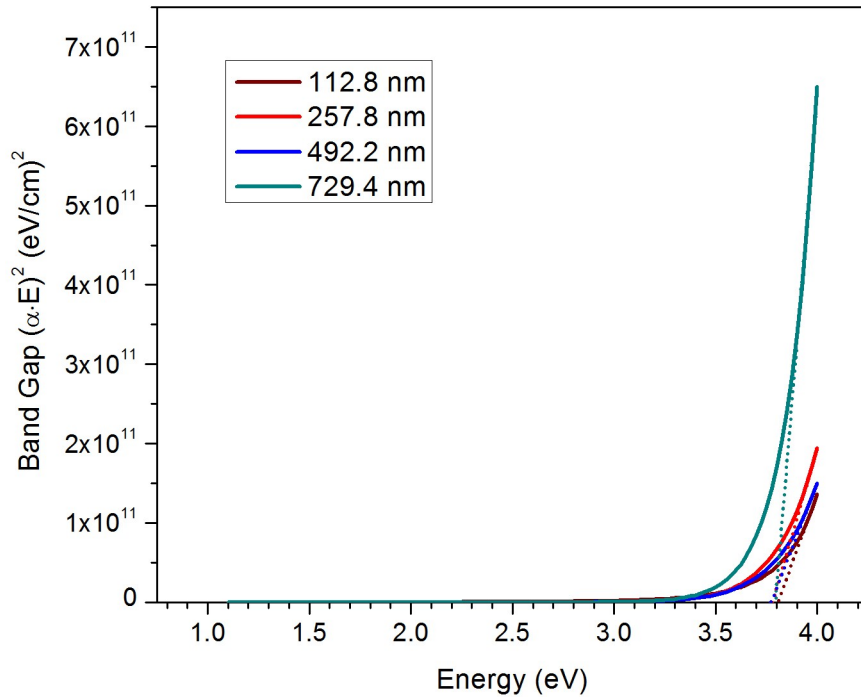


Figure 5.19: Direct band gap assessment for CTO films deposited at 10 mT, 10 % oxygen and 25 °C, with varying thickness. All samples heat treated at 600 °C.

Data regarding transmittance, as seen in Figure (5.20), is approximately what one would expect regarding transparent materials of various thicknesses, with the thinnest materials having the greatest transmittance. However, it is important to note that the thinnest material also shows the lowest average transmittance above the absorption edge. This data may also lend credibility to the trend regarding the band gap. However, due to the dependence of transmittance on thickness, this correlation may not be uniquely attributed to a fundamental change in CTO film properties.

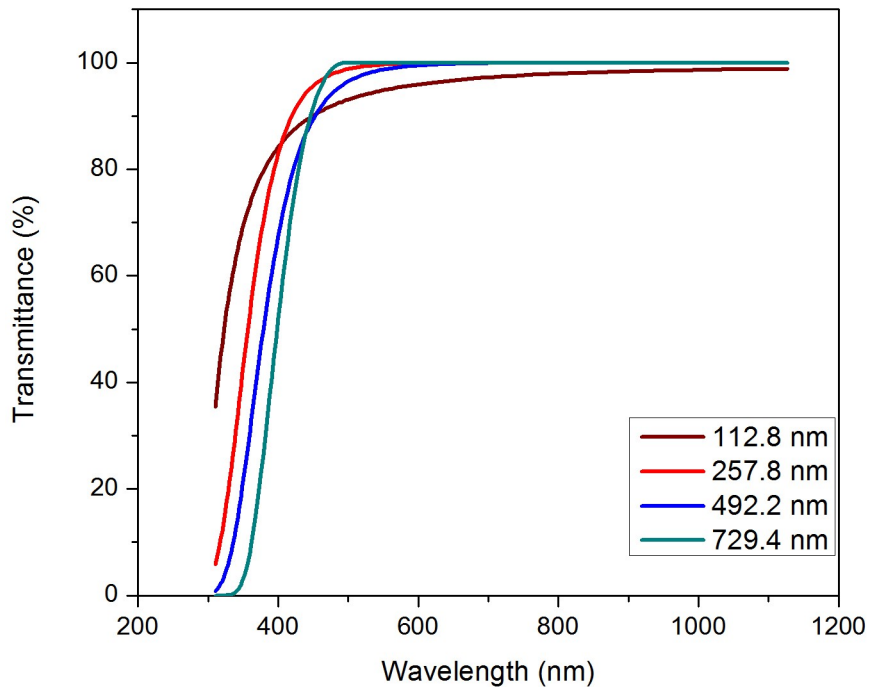


Figure 5.20: Transmittance for CTO films deposited at 10 mT, 10 % oxygen and 25 °C, with varying thickness. All samples heat treated at 600 °C.

The significant result of this data set lies with the large band gap value of the thickest sample. The thickest sample (729 nm) has a band gap significantly lower than the thinner samples (113-492 nm), all of which have very similar band gap values. During heat treatment, CdS diffused into the CTO layer, as Cd and S₂ vapor whereupon a new chemical equilibrium formed, as mentioned previously. However, the vapor penetration may have been insufficient to reach the glass-side of the thickest sample, resulting in a graded composition, crystal structure and concomitant non-uniformity in optical properties.

This is further supported by the trends of the electrical properties. As seen in Table (5.3), mobility and carrier density decreased as thickness increased. Resistivity and sheet resistance, as discussed in Chapter 4, relate back to carrier mobility and density by equation (4.10) and $\rho=R_s t$. Non-uniform diffusion of Cd and S₂ species during the heat treatment may also affect relevant morphological film properties such as grain size, allowing for larger grains to develop preferentially and possibly ultimately affecting mobility uniformity. Conversely, the thinner samples may also impede non-ideal grain structures from forming. Further work is needed to fully understand the force at work behind this thickness dependence.

Additionally, the Cd/Sn ratio for these samples shows the exact opposite behavior. As film thickness decreases, the Cd/Sn ratio decreases significantly, from ideal values of 2.1 and 2.05 for the two thickest samples, down to 1.83 for the thinnest sample. EDS measurements are capable of penetration on the order of microns, so thickness shouldn't affect the accuracy of these results. It is speculated that for the thinnest samples, the treatment time is too long, and the effect of long-term exposure to S₂ vapor acts as a transport agent for Cd species out of the film, which is ultimately destructive. This result also requires further analysis.

5.2.3 Heat Treatment Environment

Variation of heat treatment ambient content as well as heat treatment temperatures were investigated to determine the sensitivity of the film changes to chemical and thermal

conditions. Table (4.2) summarized the conditions used. Of particular interest to this work, however, are the parameters that ultimately combined to provide the best combination of optical and electrical properties, as well as the most cost and time efficient deposition. Two series in particular stood out as producing films with exceptional properties. The first deposited under 5 mT pressure with 5% oxygen content at 25 °C. The second series was deposited under a slightly higher pressure of 10 mT with 5% oxygen content and at 300 °C. However, this second higher temperature series has proven difficult to model. It is suspected that due to the various high temperature treatments, there may have been some warping of the substrate glass, rendering the ellipsometry software unsuitable for modeling. Further, this series should be considered non-ideal from a commercial perspective, due to the high temperature deposition.

The sample series used to represent materials deposited at low temperature and pressure was series SP3151. These samples were heat treated from 550 °C to 650 °C using the standard argon atmosphere and close-proximity CdS layer method as outlined by Wu [29]. Further heat treatments were done at a fixed temperature of 600 °C using various environments. Changes are detected in the film properties for those treated about 550 °C using the standard conditions. Electrical properties dramatically improve for the samples treated at 600 °C and 650 °C, when compared to the sample treated at 550 °C.

Optical properties, as depicted in Figures (5.21), (5.22) and (5.23) display a similar behavior regarding the samples receiving low temperature heat treatment. This

behavior may be indicative of the degree of crystallization of the material obtained at these higher temperatures [28] [29]. The optical constants of the low temperature sample differs significantly from those heat treated at temperatures equal to or greater than 600 °C.

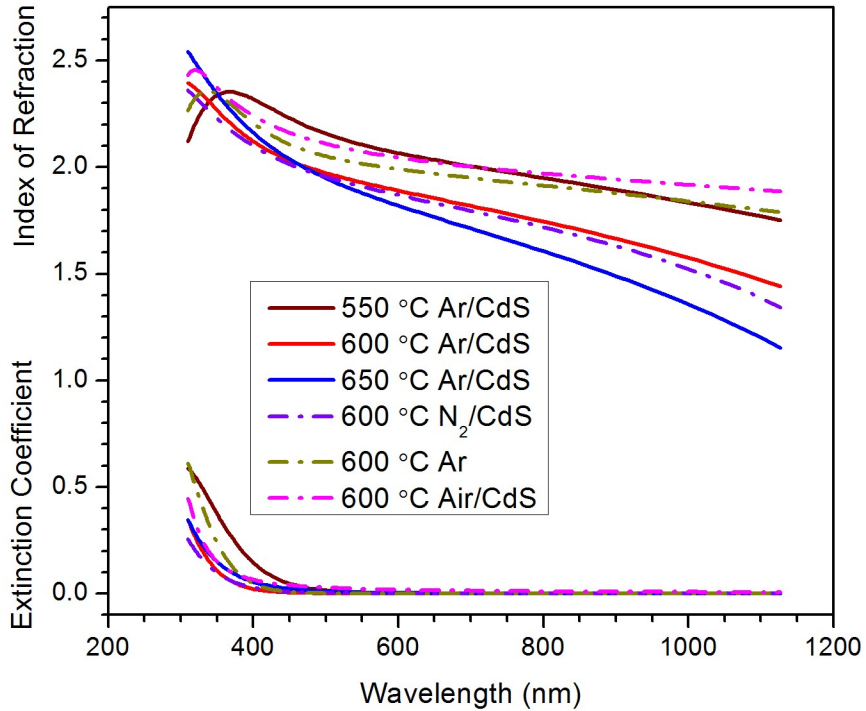


Figure 5.21: Optical constants for CTO films deposited at 5 mT, 5% oxygen and 25 °C, with varying heat treatment temperatures (solid) and environments (dashed).

Further, the band gap also shifts significantly higher for the high temperature samples. The same problem previously encountered regarding very high band gaps is once again present, producing data from which it is difficult to determine band gap values. However, it is fairly obvious that the band gap for the two high temperature

samples heat treated using the standard conditions are significantly higher than the low temperature heat treatment samples. It is interesting to note that both of the high temperature heat treatments produce roughly the same band gap, as inferred by the data in Figure (5.22).

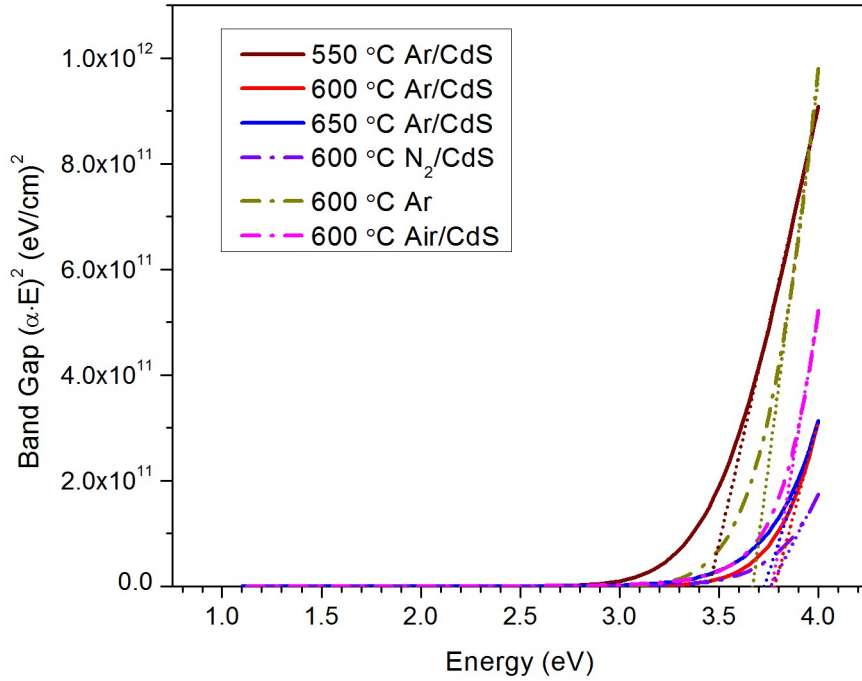


Figure 5.22: Direct band gap assessment for CTO films deposited at 5 mT, 5% oxygen and 25 °C, with varying heat treatment temperatures (solid) and environments (dashed).

Transmittance for these samples as seen in Figure (5.23) shows that the highest integrated transmittance is obtained with heat treatment at 600 °C using standard conditions. At 650 °C, a drop in transmittance is obtained.

Comparing the data for the standard environment at 600 °C to those of differing environments reveals interesting behavior. The sample heat treated in nitrogen with CdS, as well as the sample heat treated in argon with no CdS, produced comparable electrical properties to those of the standard sample. Of particular interest is the very high mobility and very low carrier density for the argon only sample. The sample treated in air with CdS produced poor results, electrically.

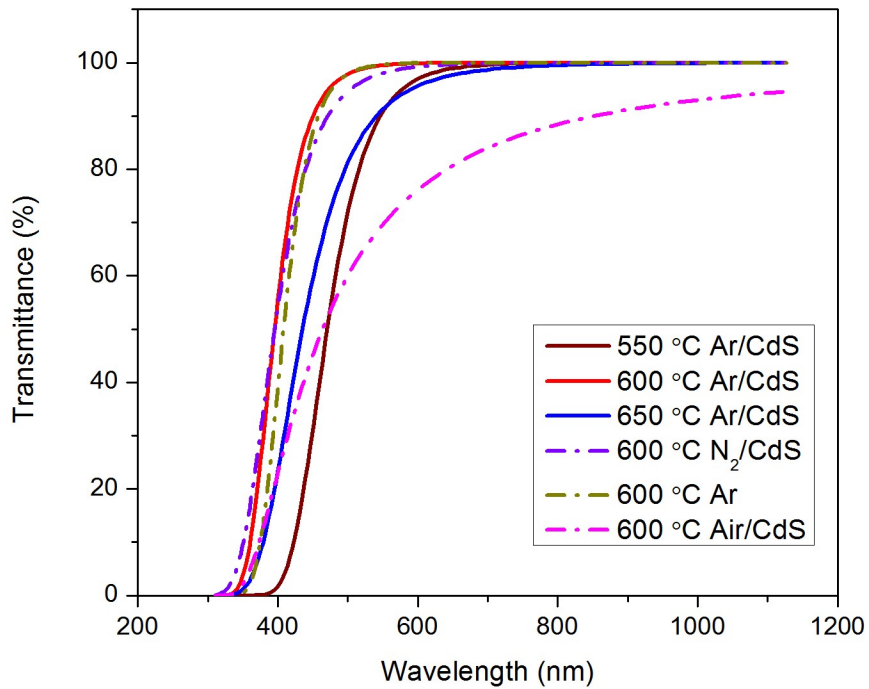


Figure 5.23: Transmittance for CTO films deposited at 5 mT, 5% oxygen and 25 °C, with varying heat treatment temperatures (solid) and environments (dashed).

Optically, the samples heat treated at 600 °C in varying environments behaved very similarly to those of the standard environment, with optical constants in approximate

agreement with those obtained by treatment in the standard environment. Band gap values were also very high, with the lowest of these samples being at 3.65 eV, still higher than the band gap of the sample heat treated at 550 °C. Further, both the nitrogen/CdS and argon samples showed very good transmittance, equal to that of the standard atmosphere. Air/CdS fared very poorly in transmittance.

Several points become clear from this series. As mentioned earlier, 600 °C appears to be the likely the minimum temperature needed to fully crystallize the CTO layer. This is strongly suggested by the optical data as well as the electrical data. Further, ambient atmosphere has an interesting effect on the electrical properties of these materials.

Optically, both the samples heat treated in nitrogen with CdS and argon with no CdS had properties comparable to those of the samples heat treated in argon with CdS. However, the argon-only treated sample had a far lower carrier density than the sample with argon and CdS, while both having similarly high values of mobility. This is a reasonable result, based on the explanation offered by Wu and McCandless in Section 5.2.1. This low carrier density may be desired in a final CTO product, however it does seem to cost the material slightly with regard to resistivity as well as the Cd/Sn ratio. It may be worthwhile to explore methods of varying the CdS allowed to diffuse into the CTO layer, in order to achieve a balance between carrier density and the rest of the electrical properties for the material.

Finally, replacing argon with nitrogen produces similar results to those of argon. Nitrogen gas is inert, so these results are not surprising. There was a slight drop in electrical quality, however.

As a rule, most of the samples treated at high temperature in argon or nitrogen were of high optical and electrical quality. The CTO material quality is high, compared to previous results by Wu, especially considering the variety of heat treatments used on this sample. Table (5.6) compares these properties to those mentioned in Chapter 2 achieved by Wu. All samples discussed from this series, with the exception of air/CdS, were comparable to the results achieved by Wu.

Table 5.6: Electric properties of CTO produced by Wu, compared to SP3151 samples.

Material	Thickness (nm)	Carrier Density (cm ⁻³)	Mobility (cm ² /Vs)	Resistivity (Ωm)	Sheet Resistance (Ω/sq)
Wu's Results	510	8.94 x 10 ²⁰	54.50	1.28 x 10 ⁻⁴	2.60
Ar/CdS 550 °C	879	3.49 x 10 ²⁰	39.39	4.54 x 10 ⁻⁴	5.54
Ar/CdS 600 °C	838	7.20 x 10 ²⁰	55.63	1.60 x 10 ⁻⁴	1.95
Ar/CdS 650 °C	821	6.34 x 10 ²⁰	46.02	2.14 x 10 ⁻⁴	2.61
N ₂ /CdS 600 °C	612	5.98 x 10 ²⁰	49.17	2.13 x 10 ⁻⁴	2.59
Ar 600 °C	667	2.60 x 10 ²⁰	57.61	4.18 x 10 ⁻⁴	6.23
Air/CdS 600 °C	710	3.39 x 10 ²⁰	5.33	35.2 x 10 ⁻⁴	42.98

5.2.4 Summary

From the effects of these heat treatments, much can be discerned. From the data presented here, 600 °C seems to be near the optimal temperature for conducting post-deposition heat treatments of CTO films on the glass types used. This temperature is sufficient to fully crystallize the materials, while also benefiting the optical and electrical properties, indicating a connection between the activation energy for crystallographic and electronic properties. Further, this temperature is not so great that the glass substrates employed in this study will be negatively affected during heat treatment. A natural extension of this work is to examine the effect of higher temperatures on more thermally stable glasses, such as borosilicate or fused silica.

As seen above, deposition oxygen content may ultimately affect the efficacy of the CdS diffusion process which is central to these heat treatments, as a limited quantity of excess oxygen is unlikely to be controllably added during the post-deposition heat treatments. Similarly, deposition thickness may have a similar effect on these final properties due to the limitations of the CdS vapor penetration depth in solid CTO film. Additionally, a way to control the degree of CdS diffusion may offer further control over the final optical and electrical properties of these materials.

Chapter 6

CONCLUSION AND FUTURE WORK

6.1 Conclusion

6.1.1 Summary of Results

As seen in Chapter 5, results comparable to those achieved by Wu were able to be obtained through a variety of heat treatment conditions. The standard argon atmosphere with a CdS layer in close proximity to the CTO layer proved to be as effective as Wu described it in achieving high quality optical and electrical properties for the CTO layer. Further, it was learned that heat treatment temperatures of approximately 600 °C produced the highest quality optical properties for CTO. Interestingly, an argon atmosphere with no close proximity CdS layer produced very similar results, however with a noticeably lower carrier density. This may be of great use to further work, considering the suspected impact carrier density has on free-carrier absorption in the near infra red. Additionally, a better understanding of the CdS diffusion during heat treatment was achieved, by studying the properties and mechanisms of semiconductor spinel formation and band gap structure. The behavior of the CTO during heat treatment suggests that a spinel structure is formed.

Additionally, the effects of both oxygen content and pressure of the deposition atmosphere were able to be determined, showing that a 5% oxygen content results in the highest quality CTO samples. Furthermore, the impact of deposition pressure on the samples has been shown to be noticeable, if not ultimately relevant to the final optical and electrical properties. It was also determined that samples deposited at room temperature, followed by a high temperature heat treatment, produced CTO samples with the highest optical and electrical quality. This process reduced the quantity of undesired material phases in the final film. Additionally, this process will be less time- and cost-intensive for commercial cell production.

Post-deposition heat treatments play a very large role in developing ideal CTO layers. Both the film thickness and the film oxygen content, as determined during deposition, may prove critical to how effective the close-proximity CdS heat treatment method works. Further exploring ways to vary the amount of CdS that diffuses into the material may also be of great benefit.

6.1.2 Ellipsometry

It should be noted as well that a highly effective system of modeling samples through the use of the variable angle spectroscopic ellipsometer has been established. This new procedure will allow for faster, more uniform analysis to be carried out, with a reduction in correlation and uniqueness related errors. The ellipsometry data is incredibly useful when analyzing the optical properties of these materials. It has also been shown to

be a viable way to interpret band gap structure, in conjunction with the GIXRD data. Together, a great deal of knowledge regarding sample characterization can be gleaned from these measurement systems.

6.1.3 Further Details

It should be noted that thickness discrepancies among the heat treated samples were widespread. All three sample series shown in Table (5.3) display some degree of variation from the measured thickness, especially the oxygen series and the low pressure low temperature series. This data was some cause for concern. However, it was noted earlier that due to the geometry of the deposition system, there was a great deal of thickness variation between the center of the sample and the edge of the sample. The center thickness, as noted in Table (5.3) was typically measured off of a very central sample cut, typically the top half of sample cut 7. These samples were also only measured after deposition. Distance from this central measurement combined with the effects of heat treatment can be attributed to most of these discrepancies.

Further, it is suspected that grain size may affect how light travels through the samples. This may cause scattering of the light inside the sample, changing the way the ellipsometer sees the sample. This scattering effect is strongly suspected to have occurred for some samples, due to the behavior of the model structure as well as results from the AFM. This new 'effective' thickness would be a result of this change in light path due to grain size, and may lend itself to the various discrepancies in sample thickness.

6.2 Future Work

6.2.1 Cadmium Tin Oxide

Regarding CTO, there is still a fair amount of work to be done. Some time should be spent further defining the effect of deposition conditions before and after heat treatment. This may allow for an ideal set of deposition parameters to be developed, further maximizing the qualities of the final heat treated product. Furthermore, ways to vary CdS diffusion and penetration during heat treatments may be crucial to forming cells with ideal electrical properties.

Additionally, further refinement of band gap measurements would benefit the study of CTO. The band gaps for several of the heat treated samples were higher than expected, resulting in incomplete data sets being obtained. Since this work was primarily focused on data trends, exact determination of these band gap values was of secondary importance. However, future work regarding the deposition and heat treatment conditions noted here may benefit from more accurate knowledge of these band gap values.

6.2.2 Cadmium Telluride Solar Cells

At this point, CTO is suitable for use as a high quality TCO for CdTe based solar cells. As mentioned by Wu [11] [13], a ZTO based buffer layer is used in conjunction with CTO to replace SnO₂ in the standard structure of CdTe based cells. This buffer layer could reduce the probability of forming localized CTO/CdTe junctions as well as improving adhesion during CdCl₂ treatments, among several other benefits [39]. Work

regarding the optical and electrical properties of ZTO during deposition and heat treatment, as well as how these treatments fit with work involving CTO, are of great importance to this device structure. Ultimately, all components of this cell structure will follow a similar procedure outlined here for CTO, in order to maximize the quality of the optical and electrical properties and ideally achieve a high efficiency CdTe based solar cell at a low cost¹.

1 At the date of this publishing, the group at the Institute of Energy Conversion has produced cadmium telluride based solar cells using CTO thin films produced following the described methodology. A 600 °C heat treatment with close-proximity CdS in an argon ambient was used in the production of this CTO layer. Additionally, a 40 nm thick sputtered ZTO high resistance layer was deposited between the CTO and the CdS layers of the cell. Cells produced in this fashion currently have greater than 16% efficiency.

REFERENCES

- [1] Addison, J., (July 24, 2010), “Solar Energy's 33 Percent Annual Growth Will Accelerate”, Clean Fleet Report, <http://www.cleanfleetreport.com/renewables/solar-energy-growth-facts/>, (December 3, 2010).
- [2] (June 21, 2010), “United States PV Market Becomes a Global Demand Leader by 2012”, SolarServer, <http://www.solarserver.com/solar-magazine/solar-report/solar-report/united-states-pv-market-becomes-a-global-demand-leader-by-2012.html>, (December 3, 2010).
- [3] Yildiz, O., (November 23, 2010), “Electric Power Annual”, U.S. Energy Information Administration, http://www.eia.doe.gov/cneaf/electricity/epa/epa_sum.html, (December 5, 2010).
- [4] (October 25, 2010), “US Solar Poised for \$100bn Growth Surge”, Bloomberg: Press Release, <http://www.bloomberg.com/news/2010-10-25/us-solar-poised-for-100bn-growth-surge.html>, (February 3, 2011).
- [5] (August 13, 2007), “Understanding the Cost of Solar Energy”, Green Econometrics, http://greenecon.net/understanding-the-cost-of-solar-energy/energy_economics.html, (December 7, 2010).
- [6] Evans-Pritchard, A., (February 19, 2007), “Monday View: Cheap Solar Power Poised to Undercut Oil and Gas by Half”, The Telegraph, http://www.telegraph.co.uk/finance/comment/ambroseevans_pritchard/2804574/Monday-view-Cheap-solar-power-poised-to-undercut-oil-and-gas-by-half.html, (December 7, 2010).
- [7] Gupta, P., (February 10, 2010), “U.S. Solar Upstart Aims to Match First Solar's Cost”, Reuters, <http://www.reuters.com/article/2010/02/11/miasole-idUSN1017639820100211>, (February 3, 2011).
- [8] (June, 2010), “Solarbuzz Reports World Solar Photovoltaic Market Grew to 7.3 Gigawatt in 2009”, Marketbuzz 2010, <http://www.solarbuzz.com/marketbuzz2010-intro.htm>, (December 5, 2010).

- [9] Wynn, G., (October 19, 2007), “Solar Power Edges towards Boom Time”, Reuters, <http://www.reuters.com/article/idUSL1878986220071019>, (December 13, 2010).
- [10] (September 21, 2010) “Solar Cell Hits Record Efficiency”, Greenbang, http://www.greenbang.com/new-solar-cell-achieves-record-efficiency_15305.html, (February 3, 2011).
- [11] Wu, X., 2004, High-efficiency Polycrystalline CdTe Thin-film Solar Cells, *Solar Energy*, v. 77, p. 803-814.
- [12] Osborne, M., (September 7, 2010), “First Solar's Market Share Set to Soar”, PVTech, http://international.pv-tech.org/news/first_solars_market_share_set_to_soar, (February 3, 2011).
- [13] Wu, X., Ribelin, R., Dhere, R. G., Albin, D. S., Gessert, T. A., Asher, S., Levi, D. H., Mason, A., Moutinho, H. R., and Sheldon, P., 2000, High-efficiency Cd₂SnO₄/Zn₂SnO₄/Zn_xCd_{1-x}S/CdS/CdTe Polycrystalline Thin-film Solar Cells, *Conference Record of the Twenty-Eighth IEEE Photovoltaic Specialists Conference, Anchorage, Alaska*, p. 470-474.
- [14] Britt, J., and Ferekides, C., 1993, Thin-film CdS/CdTe Solar Cell with 15.8% Efficiency, *Applied Physics Letters*, v. 62, p. 2851-2852.
- [15] Meng, L. J., and dos Santos, M.P., 1996, Structure Effect on Electrical Properties of ITO Films Prepared by RF Reactive Magnetron Sputtering, *Thin Solid Films*, v. 289, p. 65-69.
- [16] Wu, X., Dhere, R. G., Zhou, J., Duda, A., Perkins, C., Yan, Y., and Moutinho, H. R., 2003, High-Quality Cadmium Stannate Transparent Conductive Oxide Film for Tandem Thin-Film Solar Cells, *3rd World Conference on Photovoltaic Energy Conversion*, Osaka, Japan, Poster 507.
- [17] Theeten, J. B., and Aspnes, D.E., 1981, Ellipsometry in Thin Film Analysis, *Annual Review of Materials Research*, v. 11, p. 97-122.
- [18] Collins, R. W., Ferlauto, A. S., Ferreira, G. M., Chen, C., Koh, J., Koval, R. J., Lee, Y., Pearce, J. M., Wronski, and C. R., 2003, Evolution of Microstructure and Phase in Amorphous, Protocrystalline, and Microcrystalline Silicon Studied by Real Time Spectroscopic Ellipsometry, *Solar Energy Materials & Solar Cells*, v. 78, p. 143-180.
- [19] Jellison, G. E., 1993, Data Analysis for Spectroscopic Ellipsometry, *Thin Solid Films*, v. 234, p. 416-422.

- [20] Tompkins, H. G., and McGahan, W. A., 1999, *Spectroscopic Ellipsometry and Reflectometry: A User's Guide*, John Wiley & Sons, Inc, New York, NY, 228 p.
- [21] Fried, M., Lohner, T., and Gyulai, J., 1997, Ellipsometric Analysis, *Semiconductors and Semimetals*, v. 46, p. 1-36.
- [22] J. A. Woollam Co., Inc., *Guide to Using WVASE32: Software for VASE and M-44 Ellipsometer*, J. A. Woollam Co., Inc., Lincoln, NE, 587 p.
- [23] Landauer, R., 1978, *Electrical conductivity in inhomogeneous media*, AIP Conference Proceedings, 40, American Institute of Physics, p. 2–45.
- [24] Tiwald, T., (January 2008), “The Gaussian Oscillator”, J. A. Woollam, http://www.jawoollam.com/Newletters/TechNotes/gaussian_oscillator.pdf, (January 17, 2011).
- [25] Jellison, G. E., Merkulov, V. I., Poretzky, A. A, Geohegan, D. B., Lowndes, D. H., and Caughman, J. B., 2000, Characterization of Thin-film Amorphous Semiconductors Using Spectroscopic Ellipsometry, *Thin Solid Films*, v. 377-378, p. 68-73.
- [26] Spectroscopic Ellipsometry Tutorial, *J.A. Woollam Co., Inc. Ellipsometry Solutions*, http://www.jawoollam.com/tutorial_1.html, (February 2, 2010).
- [27] Hilfiker, J., Private communication, J.A. Woollam Co., Inc., 11/30/2010
- [28] Haacke, G., Mealmaker, W. E., and Siegel, L. A., 1978, Sputter Deposition and Characterization of Cd₂SnO₄ Films, *Thin Solid Films*, v. 55, p. 67-81.
- [29] Wu, X., and Coutts, T. J., Thin Transparent Conducting Films of Cadmium Stannate, U. S. Patent 6,221,495, April 24, 2001.
- [30] Wu, X., Mulligan, W. P., and Coutts, T. J., 1996, Recent Developments in RF Sputtered Cadmium Stannate Films, *Thin Solid Films*, 286, p. 274-276.
- [31] Fritzsche, H., 1971, Optical and Electrical Energy Gaps in Amorphous Semiconductors, *Journal of Non-Crystalline Solids*, v. 6, p. 49-71.
- [32] Pankove, J. I., 1971, *Optical Processes in Semiconductors*, Prentice-Hall, Inc., Englewood Cliffs, NJ, 422 p.
- [33] Nozik, A. J., 1972, Optical and Electrical Properties of Cd₂SnO₄: A Defect Semiconductor, *Physical Review B*, v. 6, n. 2, p. 453-459.

- [34] van der Pauw, I. J., 1958, A Method of Measuring Specific Resistivity and Hall Effect of Discs of Arbitrary Shape, *Philips Research Reports*, v. 13, n. 1.
- [35] McCandless, B., Private communication, Institute of Energy Conversion, University of Delaware, 4/19/2011.
- [36] Ingram, B. J., Gonzalez, G. B., Kammler, D. R., Bertoni, M. I. and Mason, T. O., 2004, Chemical and Structural Factors Governing Transparent Conductivity in Oxides, *Journal of Electroceramics*, v. 13, p. 167-175.
- [37] Walsh, A., Wei, S., Yan, Y., Al-Jassim, M. M. and Turner, J. A., 2007, Structural, Magnetic, and Electronic Properties of the Co-Fe-Al Oxide Spinel System: Density-Functional Theory Calculations, *Physical Review B*, v. 76, p. 165119-1 – 165119-9.
- [38] Segev, D., and Wei, S., 2005, Structure-Derived Electronic and Optical Properties of Transparent Conducting Oxides, *Physical Review B*, v. 71, p. 125129-1 – 125129-11.
- [39] Wu, X., Sheldon, P., Mahathongdy, Y., Ribelin, R., Mason, A., Moutinho, H., Coutts, T., 1998, CdS/CdTe Thin-Film Solar Cell with a Zinc Stannate Buffer Layer, *National Center for Photovoltaics Program Review Meeting, Denver, CO*.